

OPTIMIZATION OF INTERNAL-Sn Nb₃Sn COMPOSITES

by

MICHAEL THOMAS NAUS

A dissertation submitted in partial fulfillment
of the requirements for the degree of

DOCTOR OF PHILOSOPHY
(MATERIALS SCIENCE)

UNIVERSITY OF WISCONSIN – MADISON

2002

© Copyright by Michael Thomas Naus 2002
All Rights Reserved

ACKNOWLEDGEMENTS

There are many people that I would like to thank who have made my time at Wisconsin so enjoyable. Foremost, I must thank my advisor, David Larbalestier, for his guidance, understanding and patience with this thesis work. I am deeply indebted to Peter Lee not only for his advice and excellent microscopy skills, but also for his sense of humor and good cheer. Many thanks to Bill Starch for maintaining the fabrication and heat treatment facilities, and always taking the time to help me figure out how to build something. I am grateful for the many helpful discussions with Lance Cooley, who often provided more ideas than I knew what to do with. I especially need to acknowledge my fellow graduate students, both past and present, who have helped make my time in Room 602 both fun and enlightening. Specifically, I thank Rob Heussner for answering my many questions when I was just getting up to speed; Mike Field for his many antics and show tunes; and Chris Hawes, Jermal Chandler, and Chad Fischer for putting up with me when I was just looking for attention. I must also thank Matt Jewell for all his assistance, both in the lab and with this thesis. I thank the Sisters Meulemans for their encouragement and for helping me maintain my sanity, especially during the writing of this thesis. Lastly, I thank my family for being supportive during my extensive graduate career, and for not asking *too* frequently when I would be finished.

I thank the Department of Energy – Office of Fusion Energy and Division of High Energy Physics for funding this research. I am indebted to Oxford Instruments – Superconducting Technology, Inc. for providing most of conductor examined in this thesis.

This work also benefited greatly from the highly conducive discussions with many in the low temperature superconductor community, particularly at the Low Temperature Superconductor Workshops.

OPTIMIZATION OF INTERNAL-Sn Nb₃Sn COMPOSITES

MICHAEL THOMAS NAUS

UNDER THE SUPERVISION OF PROFESSOR DAVID C. LARBALESTIER

UNIVERSITY OF WISCONSIN - MADISON

The heat treatment of internal-Sn wires has two functions: (1) to mix the interfilamentary Cu with Sn from the core, and (2) to react the Sn with Nb to form the superconducting Nb–Sn A15 phase. To study the effectiveness of Cu–Sn mixing, the Cu–Sn microstructures were examined in two very different internal-Sn composites after heat treatments of 24 and 150 hours at each of 10 different temperatures (up to 600°C). None of the heat treatments generated a single-phase Cu–Sn microstructure. It was concluded that complete mixing of the Cu and Sn is highly unlikely in commercial wires. However, it was found that Cu–Sn microstructure inhomogeneity has no effect on the critical temperature (T_c), irreversibility field (H^*) or inductively measured critical current density (J_c) of fully reacted Nb₃Sn wire. Thus control of the superconducting properties lies with the composite design and the A15 reaction heat treatment. However, a Cu–Nb–Sn ternary intermetallic was discovered, which forms as a result of dissolution of Nb and therefore has deleterious effects on J_c . As the Cu fraction within the filament bundle decreases, lengthy Cu–Sn mixing heat treatments must be employed to limit formation of this ternary phase. A direct correlation was found between T_c and H^*_{Kramer} that is strongly dependent on the Sn concentration in the A15 layer, emphasizing the need to provide proper Sn stoichiometry in the Cu–Nb–Sn

package and to effectively contain the Sn within the bundle. Commonly used Nb diffusion barriers can react completely through locally, resulting in Sn loss from the A15 layer and degradation of the superconducting properties. To generate non-Cu $J_c(12\text{ T}, 4.2\text{ K}) = 3000\text{ A/mm}^2$, the required J_c within the A15 layer is 4610 A/mm^2 , equal to the best literature values. In the best performing internal-Sn conductor to date, it is shown that non-Cu $J_c(12\text{ T}, 4.2\text{ K})$ of 3000 A/mm^2 should be produced by replacing 5vol.% of the Sn core with Nb or by replacing 3 vol.% of interfilamentary Cu with Nb and Sn.

CONTENTS

ABSTRACT.....	iii
CHAPTER 1 – HISTORY AND BACKGROUND	1
1.1 MOTIVATION.....	1
1.2 GENERAL OVERVIEW OF SUPERCONDUCTIVITY.....	3
1.3 Nb ₃ Sn PROPERTIES.....	8
1.4 WIRE MANUFACTURING METHODS.....	12
1.5 HEAT TREATMENT ISSUES OF INTERNAL-Sn CONDUCTORS.....	19
1.6 SUMMARY.....	22
1.7 THESIS GOALS AND FORMAT	24
CHAPTER 2 – Cu–Sn PHASE IDENTIFICATION	26
2.1 WIRE CHARACTERISTICS	26
2.2 EXPERIMENTAL PROCEDURE.....	29
2.3 Cu–Sn PHASE IDENTIFICATION	30
2.4 DISCUSSION	32
2.5 DISCOVERY OF Cu-Nb-Sn INTERMETALLIC	35
2.6 SUMMARY.....	41
CHAPTER 3 – Cu-Sn INHOMOGENEITY EFFECTS ON THE FINAL SUPERCONDUCTING PROPERTIES	42
3.1 WIRE CHARACTERISTICS	43
3.2 EXPERIMENTAL PROCEDURE.....	45
3.3 RESULTS	48
3.3.1 SQUID – T_C	48
3.3.2 VSM – H^*_{KRAMER} AND $\Delta M/MASS$	50
3.4 DISCUSSION	54
3.5 SUMMARY.....	60
CHAPTER 4 – INTERPLAY BETWEEN T_C, H^*_{KRAMER}, H_{C2} AND COMPOSITE DESIGN	62
4.1 WIRE CHARACTERISTICS	62
4.2 EXPERIMENTAL PROCEDURE.....	65
4.3 RESULTS	69
4.4 DISCUSSION	72
4.4.1 RELATIONSHIP BETWEEN T_C AND H^*_{KRAMER}	72
4.4.2 RELATIONSHIP BETWEEN H^*_{KRAMER} AND H_{C2}	74

4.4.3 T_c AND A15 CHEMICAL COMPOSITION	76
4.4.4 COMPOSITE DESIGN IMPLICATIONS	78
4.5 SUMMARY	80
CHAPTER 5 – INFLUENCE OF WIRE DESIGN ON J_c.....	82
5.1 THE ESSENTIALS: Nb AND Sn	83
5.2 DIFFUSION BARRIER	85
5.3 INTERFILAMENTARY Cu	88
5.4 ALLOYED Sn CORE	89
5.5 ANALYSIS OF A RECENT ATTEMPT AT AN OPTIMIZED PACKAGE.....	90
5.6 SUMMARY	91
CHAPTER 6 – SUMMARY	93
REFERENCES.....	97
APPENDIX A – IMAGE ANALYSIS	101
A.1 MEASURING FEATURE SIZES	101
A.2 ATOMIC RATIO CALCULATIONS	104
A.2.1 Nb AND Cu.....	104
A.2.2 ALLOYED SN CORE.....	106
A.2.2.1 Sn-9AT.%Mg.....	107
A.2.2.2 Sn-1.3AT.%Cu.....	108
A.2.2.3 Sn WITH Ti_3Sn	109
APPENDIX B – Cu ELECTROPLATING.....	111

CHAPTER 1 – INTRODUCTION AND BACKGROUND

1.1 Motivation

There is a strong desire for the development of superconductors that can satisfy the ever-increasing magnetic field requirements of future high field magnets (> 8 T). One of the main drivers for high field superconductor development is particle physics research. As the size of the particle accelerator ring is inversely proportional to the magnetic field strength, it has historically been the strategy of the High Energy Physics (HEP) community to go for as high of a field as possible. As an example, the next new proton accelerator, presently called the *Very Large Hadron Collider*, is targeted to go online after 2015 [1] and plans call for magnetic field strengths in excess of 10 T. While such high fields generally mean more expensive magnets (in lieu of expensive land costs), the hope is that improvements in superconductor performance and manufacturing will help keep magnet costs down.

Until recently, the HEP superconductor of choice had been Nb–Ti because of its reproducible critical current densities (J_c) in long lengths and because its ductile nature makes it easy to handle. Most of the commercial Nb–Ti wire was optimized for high J_c in fields of 5 to 7 T at 4.2 K. A recent accelerator project (the Large Hadron Collider (LHC))

had increased the magnetic field requirement to ~ 10.5 T in the intersection quadrupoles. However, at 4.2 K and 10.5 T, Nb–Ti ceases to have any current carrying ability [2]. As a result, the designed operating temperature of LHC was reduced to 1.9 K so that Nb–Ti would have a significant J_c at 10.5 T. The $J_c(1.9$ K, 10.5 T) values of candidate strands were tested at the University of Wisconsin with the best attaining 1450 A/mm² [3]. It became apparent from this work that Nb–Ti was at its J_c limit and that future higher field magnets would require a superconductor with better high field properties.

Presently, the best superconductor option for higher field magnets is Nb₃Sn. Work on Nb₃Sn and Nb–Ti alloys proceeded concurrently in the early 1960's, but Nb₃Sn fell out of favor when its highly strain sensitive properties made handling difficult relative to that of Nb–Ti. However, Nb₃Sn has a higher upper critical field (H_{c2}) and critical temperature (T_c) than Nb–Ti based alloys (~ 25 T [4] & 18.3 K [5] for Nb₃Sn versus ~ 15.4 T [6] & 9.3 K [7] for Nb–Ti (H_{c2} values are at 0 K)). Presently, the Nb₃Sn strand with the highest J_c is made by the internal-Sn process (like those of this thesis), with $J_c(4.2$ K, 12 T) = 2900 A/mm² [8].

Due to the need for affordable high field magnets, a goal of the superconductor community is to make Nb₃Sn wire more cost-effective. The metric used for the cost efficiency of superconducting wire is $\$/\text{kA}\cdot\text{m}$, that is the price per unit operating current per unit length. The present cost of Nb₃Sn is $\sim \$10/\text{kA}\cdot\text{m}$ and that of Nb–Ti is $\sim \$1/\text{kA}\cdot\text{m}$. The drive is to bring Nb₃Sn conductor cost below $\$1.50/\text{kA}\cdot\text{m}$ [1]. Therefore, an important method to improve the cost efficiency is through an increase in J_c . Presently, the goal of the HEP community is to increase $J_c(4.2$ K, 12 T) to 3000 A/mm² [1]. Another way to decrease

the cost is through more efficient processing. Improvement of the Nb₃Sn heat treatment efficiency and superconducting properties are the driving forces of this work.

1.2 General Overview of Superconductivity

There are three critical, co-dependant parameters that determine whether a superconductor will be in the superconducting or normal (i.e. resistive) state: current density (J), magnetic field (B) and temperature (T). When plotted in three dimensions, these parameters form a surface beneath which a given material is in the superconducting state and it can carry essentially dissipation-free supercurrent. Above this curve, any current is dissipative (Figure 1.1). The upper limits to these parameters are the critical temperature (T_c), critical magnetic field (H_c), and critical current density (J_c). J_c is defined as the maximum, resistanceless transport current (I_c) divided by the cross-sectional area.

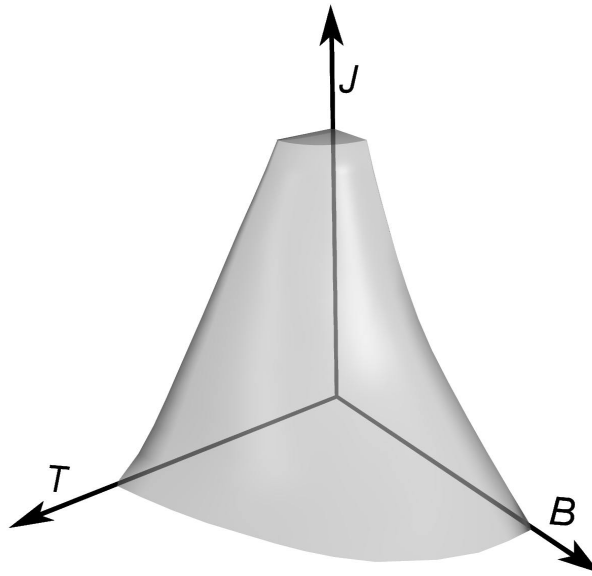


Figure 1.1. Schematic diagram of the superconducting current density–magnetic field–temperature (J-B-T) phase space. When below this ‘critical surface’, a material is in the dissipation-free superconducting state. The surface has been truncated on the J axis.

One characteristic of a superconductor is its desire to exclude an applied magnetic field from its interior. However, an applied field does penetrate a finite distance, the penetration depth (λ), into the surface of a superconductor. λ varies with temperature as

$$I(T) = \frac{I_0}{\sqrt{1 - (T/T_c)^4}}, \quad (1.1)$$

where λ_0 is the penetration depth at 0 K, which is a material property. Another fundamental, microscopic property of superconductivity is the pairing of electrons into Cooper pairs due to electron-phonon interactions. It is this property that allows for the resistanceless flow of electricity. The distance between the paired electrons is the coherence length (ξ), which varies with temperature in a similar manner as does λ . Both ξ and λ range between ~ 1 nm and ~ 1 μm and in stoichiometric Nb_3Sn , $\xi \sim 3$ nm and $\lambda \sim 60$ nm at 0 K [9].

Superconductors are divided into 2 classes that are determined by the ratio of λ to ξ , such that

$$\kappa = \frac{\lambda}{\xi}, \quad (1.2)$$

where κ is called the Ginzburg-Landau parameter. At the interface between normal and superconducting regions, there will be either a positive or negative surface energy (E_s), governed approximately by

$$E_s \sim \frac{1}{2}\mu_0 H_c^2 (\xi - \lambda). \quad (1.3)$$

It can be seen that the sign of the surface energy is dictated by the relative values of λ and ξ .

More specifically, if $\kappa < 1/\sqrt{2}$, the surface energy is positive, promoting complete magnetic flux exclusion (the Meissner state) from the superconductor up to H_c . At H_c , it becomes more energetically favorable to be in the normal state. This is Type I superconductivity and is associated with nearly all elemental superconductors. However, if $\kappa > 1/\sqrt{2}$, the normal-superconductor interfacial energy is negative and it is advantageous to have as much interfacial area as possible. In this situation, the superconductor will be in the Meissner state and magnetic flux will be excluded (as in Type I superconductivity) up to a *lower* critical field (H_{c1}). At H_{c1} , the magnetic flux enters the superconductor in discrete quanta called *fluxons* and the superconductor is said to be in the mixed state. At a much higher *upper* critical field (H_{c2}), the superconductor becomes normal. This is Type II superconductivity and it is associated with superconducting alloys and oxides (e.g. Nb–Ti, Nb₃Sn). Schematic diagrams of the H–T phase space for Type I and Type II superconductors are shown in Figure 1.2.

In Type I superconductors, J_c is limited because supercurrent only flows along the surface, and H_c and T_c are also low with maximum values of ~ 100 gauss and ~ 5 K, respectively. These low values generally preclude Type I superconductors from being technologically useful. However, in Type II superconductors, the supercurrent flows throughout the bulk allowing for much higher J_c values. Type II superconductors also

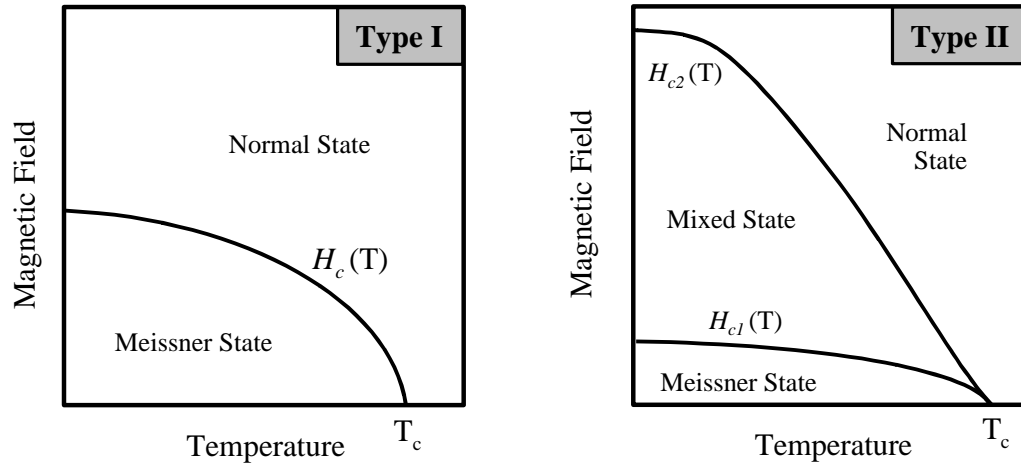


Figure 1.2. Schematics of the H–T phase space for Type I and Type II superconductors. Type I has one critical field (H_c), while Type II has a lower and upper critical field (H_{c1} and H_{c2} , respectively). Below H_c and H_{c1} , a magnetic field is completely excluded from the interior of a superconductor (Meissner state), and above H_c or H_{c2} , the material is no longer superconducting. Between H_{c1} and H_{c2} , the superconductor is penetrated by quantized magnetic flux, called “fluxons.”

generally have higher critical fields and temperatures than Type I superconductors. It is not surprising then that all technologically relevant superconductors are of Type II.

As mentioned above, Type II superconductors are penetrated by fluxons when the applied field exceeds H_{c1} . Each fluxon contains a single flux quantum ($\phi_0 = 2.1 \times 10^{-15}$ Wb) within a normal core of radius ξ and a vortex of supercurrent of radius λ . The mutually repulsive fluxons form a hexagonal lattice with a lattice spacing (a_0) equal to

$$a_0 = 1.07 \sqrt{\frac{\phi_0}{B(\text{T})}}, \quad (\text{meters}) \quad (1.4)$$

where B is the flux density (in Tesla) within the superconductor. At fields approaching H_{c2} , B can be considered equal to the applied field. As B increases, the fluxons move closer together until, at H_{c2} , the fluxon normal cores overlap and superconductivity is extinguished.

When a transport current flows through a superconductor, a force ($F_L = \mathbf{J} \times \mathbf{B}$) that is perpendicular to both the applied field and the current acts on the fluxons (Figure 1.3). When a fluxon moves, electrons cross its normal core and dissipate energy. Therefore, in order to have lossless current, the fluxons must be held stationary, or “pinned.” Imperfections in the superconductor act as pinning centers and retard fluxon motion with a volume flux pinning force F_p . The condition $F_L = F_p$ defines J_c , where the fluxons become depinned and move across the sample, generating a voltage and energy loss. Therefore, the first voltage encountered in a J_c measurement is that of fluxon motion and not that of the superconductor changing to the normal, resistive state. The field at which $F_p = 0$ is H^* (the irreversibility field), and no bulk supercurrent can flow above this field. The condition $F_p = 0$ thus defines the technologically relevant maximum magnetic field.

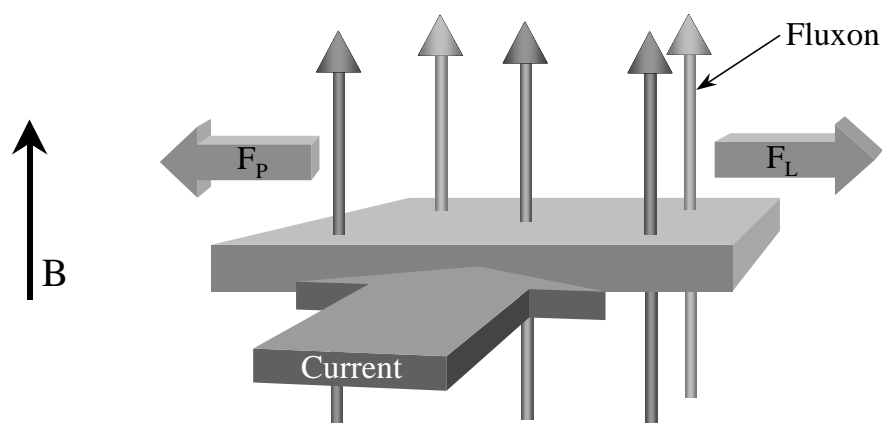


Figure 1.3. The forces acting on fluxons when there is an applied electric current. The Lorentz force on the fluxons (F_L) is countered by the pinning force due to defects (F_p). When $F_L > F_p$, the fluxons move and energy is dissipated.

1.3 Nb₃Sn Properties

Nb₃Sn is a Type II superconductor that possesses the brittle A15 crystal structure. For a generic A15 compound, A₃B, the B atoms reside on a body-centered cubic lattice with two A atoms on each face (Figure 1.4). The A atoms lie on 3 orthogonal chains and they are often closer to each other than in pure A. This has the effect of increasing the density of states, which in turn increases the superconducting properties over those of pure A. For example, the T_c values of Nb and Nb₃Sn are 9.1 K and 18.3 K, respectively, and the Nb and Nb₃Sn lattice spacings are ~ 2.940 Å and ~ 2.645 Å, respectively. There are several intermetallic compounds in the Nb–Sn system [10]. Unlike the other Nb–Sn intermetallics (Nb₆Sn₅ and NbSn₂), Nb₃Sn is not a line compound, but rather exhibits solid solution from 18 to ~ 25 at.% Sn. The A15 lattice parameter decreases nearly linearly from 5.290 Å for Nb-25at.%Sn to 5.280 Å for Nb-18at.%Sn [11]. The Nb–Sn A15 phase undergoes a cubic-to-tetragonal phase transformation below 43 K [12] for compositions above

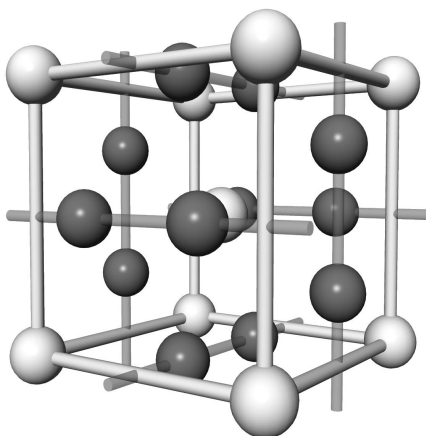


Figure 1.4. The A15 crystal structure of Nb₃Sn . The dark spheres are Nb atoms and the light spheres are Sn atoms. The Sn atoms form a body-centered cubic crystal structure with 2 Nb atoms forming mutually orthogonal chains across the faces.

24.5at.% Sn [11], which has the effect of lowering the superconducting properties due to a decrease in the density of states [13].

All Nb–Sn A15 compositions are superconducting, and T_c and H_{c2} increase with increasing Sn concentration up to just below stoichiometry. Therefore, near stoichiometry offers the best superconducting properties, but it is rarely achieved in practice due to small Sn diffusion coefficients. T_c ranges from ~6 K at Nb-18at.%Sn to 18.3 K at Nb-25at.%Sn [11]. T_c abruptly drops by ~0.5 K above Nb-24.5at.%Sn due to the decrease in the density of states caused by the cubic-to-tetragonal transformation [11].

Stoichiometric A15 H_{c2} values reported in the literature are much more varied than T_c . $H_{c2}(0\text{ K})$ values range from 21.6 T to 28 T [14, 15, 16, 17, 18]. The wide discrepancy in H_{c2} may be due to different measurement techniques, measurement criteria, strain state, true Sn content or atomic order. In Nb₃Sn samples of the same composition, Orlando et al. [16] reported that H_{c2} decreases with increasing atomic order, as measured by normal state resistivity (ρ_n) at T_c . The wide range of reported H_{c2} values highlights the need that still exists for accurate, reproducible H_{c2} measurement of Nb₃Sn compounds.

There have been few studies of the variation of H_{c2} as a function of Sn concentration [11, 13, 19]. Flükiger, Schauer and Goldacker [13] compiled data from the literature on pure, clean samples which showed that H_{c2} increases with increasing Sn content up to ~24.5at.%Sn, where it falls off precipitously, again due to the cubic-to-tetragonal transition. H_{c2} behavior can be understood using an equation derived by Kim, Hempstead and Strnad [20]

$$H_{c2}(0) = 3.11 \times 10^3 \cdot \rho_n \cdot \gamma \cdot T_c, \quad (\text{Tesla}) \quad (1.5)$$

where γ is the electronic specific heat coefficient in $\text{J/m}^3 \cdot \text{K}^2$, ρ_n is in $\Omega\text{-m}$ and, and T_c is in Kelvin. [13] has shown that ρ_n decreases with increasing Sn due to the increase in atomic order. However, both T_c and γ increase [9, 13] with increasing Sn, thus increasing H_{c2} . Equation 1.5 illustrates how the sharp decrease in T_c due to the cubic-to tetragonal transition influences H_{c2} and it also explains the increase in H_{c2} with disorder (and thus ρ_n) as reported by Orlando et al. [16]

Much of what was reported in the literature as H_{c2} is actually H^* , the field at which the bulk $J_c = 0$, as awareness of the existence of H^* did not come about until the discovery of high temperature superconductors in the late 1980's. The upper critical field was often determined by an extrapolation of F_p , J_c or of a Kramer function ($J_c^{1/2} \cdot B^{1/4}$ versus B) [21] to zero. However, extrapolations such as these have been shown to give H^* , not H_{c2} , in Nb–Ti wires [2].

A key factor controlling the J_c of a Nb_3Sn conductor is grain size. It has been shown that grain boundaries are the primary magnetic flux pinning centers in Nb_3Sn [22, 23] and grain size should thus be minimized to maximize J_c . In the formation of Nb_3Sn , lower reaction temperatures produce smaller grain sizes [22, 24, 25]. However, 600°C is considered to be the practical lower temperature bound for Nb–Sn A15 formation because Nb_3Sn formation is exceedingly slow below this. In the multifilamentary tapes studied by Scanlan, Fietz and Koch [22], it took 500 hours at 600°C to form an A15 layer just $1 \mu\text{m}$ thick. While lower reaction temperatures lead to smaller grain sizes, they also lead to a less

stoichiometric A15 layer because of the inevitable Sn concentration gradient. It has been shown in multifilamentary wires that lower reaction temperatures form an A15 compound with lower Sn content and, consequently, decreased H_{c2} [19, 25]. To maximize J_c (the parameter of principal importance to magnet designers), one must carefully balance the need for small grains with the need for high Sn concentration.

Small amounts of third element additions often influence the superconducting properties. This was studied extensively by Suenaga et al. [4] in bronze-processed wires (the bronze-process is described later in this chapter). They showed that additions of 1 to 2 at.% of Ti or Ta increase T_c by ~ 0.3 K, whereas V, Zr and Mo decrease T_c . Also 2 to 4 at.% of Ti, Ta, V, or Mo increase H_{c2} (4.2 K) by up to 3.5 T, with the largest increases due to Ti or Ta addition [4]. Non-transition metal additions of Al, Ga, In, Tl and Pb have also been reported to increase H_{c2} (4.2 K) to up to ~ 30 T [26]. Almost all commercially available Nb_3Sn conductor is alloyed with either Ti or Ta, and all of the conductors studied in this thesis have Nb-2at.%Ti filaments.

The increase in H_{c2} with small amounts of solute is likely due to an increase in ρ_n through impurity scattering. In the presence of solute atoms or atomic disorder, the cubic-to-tetragonal transition is suppressed [27] and thus no fall-off of H_{c2} (or T_c) is expected at high Sn concentrations, as is seen in the unalloyed material. However, no study of H_{c2} as a function of Sn concentration for alloyed Nb_3Sn was found in the literature.

The addition of Ti, Ta or Mg has been shown to inhibit grain growth [28, 29, 30, 31] and Mg has also been shown to increase A15 layer growth rate [30]. McKinnell et al. [32] believed that Mg enhances the flow of Sn to the Nb filaments by decreasing the solubility of

Sn in the interfilamentary Cu and forcing it to the Cu-Sn(-Mg) grain boundaries where diffusion is faster. The increased Sn availability then promotes faster A15 layer growth and smaller A15 grains. Consistent with these effects, Nb₃Sn wires manufactured with Mg additions have shown improved J_c values [31, 32].

Nb₃Sn has one of the strongest strain dependencies of the A15 superconductors, showing marked decreases in H_{c2} [33], T_c [34] and I_c [35] with strain. The strain effect on the superconducting properties is reversible up to the point where fracture begins, ϵ_{irr} . The strain tolerance in Nb₃Sn wire is dependent upon the fabrication method, with ϵ_{irr} ranging from 0.2 to 0.9% [33]. Apart from handling concerns, strain effects play an important role in composite Nb₃Sn wire because the Nb and Nb₃Sn have smaller thermal contraction coefficients than the Cu-based wire components. This thermal contraction mismatch leads to Nb₃Sn being in a state of “pre-compression” after heat treatment and upon cooling to operating temperatures [34]. This pre-compression can attain 0.5%, significantly enhancing the strain tolerance of a conductor under tensile stress.

1.4 Wire Manufacturing Methods

There are presently three primary processes used in the manufacture of Nb₃Sn wire – bronze, powder-in-tube (PIT) and internal Sn (Figure 1.5). The three processes differ in their Sn source, which has important ramifications for the overall wire design. However, all designs use solid state diffusion to transport Sn from the source to the Nb filaments, and all require a diffusion barrier. The barrier keeps the Sn where it is needed (i.e. near the Nb) and

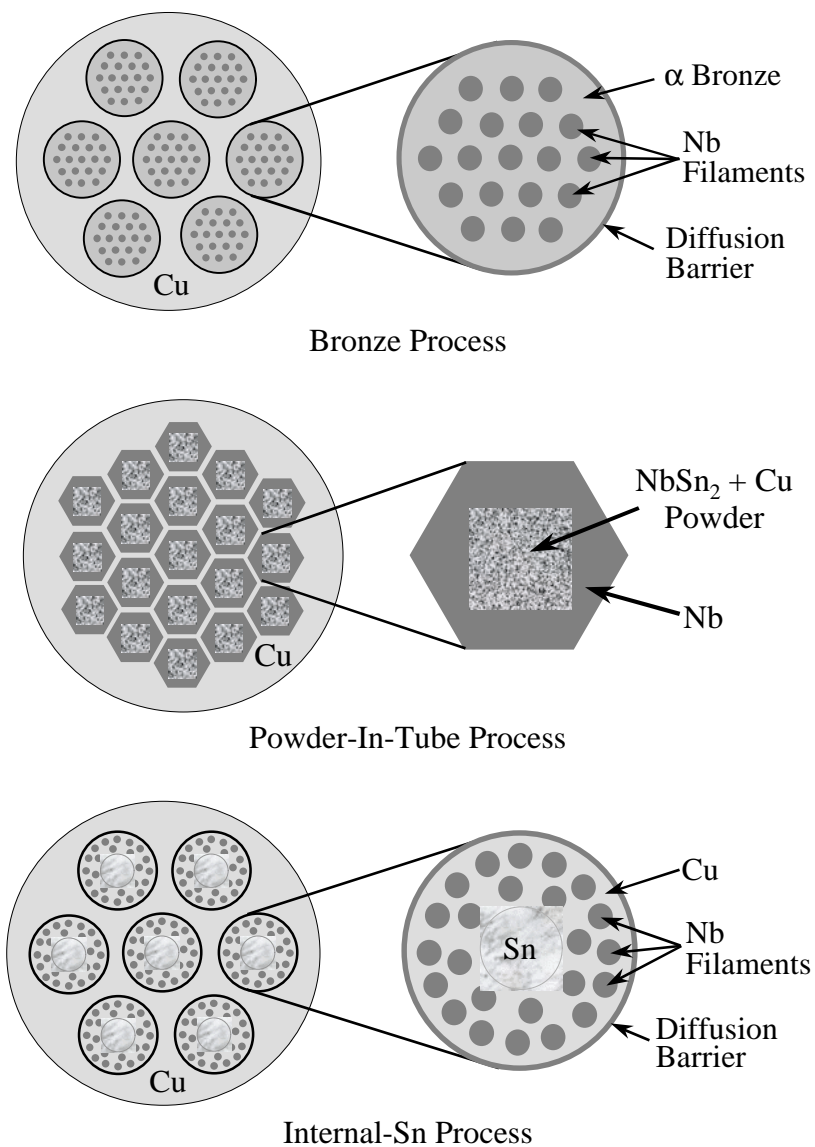


Figure 1.5. Schematics of the three main Nb₃Sn wire fabrication techniques – bronze, powder-in-tube and internal-Sn. All processes use diffusion to form Nb₃Sn from a ductile Sn source.

out of the surrounding pure Cu, the high conductivity of which is needed to electromagnetically stabilize and protect the conductor.

It should be noted that difficulty often exists in comparing the J_c values of wires produced by different manufacturing methods because J_c is usually reported as a “non-Cu” J_c value ($J_{c,non-Cu}$). That is, J_c is normalized to the portion of the wire cross-section that generates the Nb–Sn A15 phase, including the diffusion barrier needed to protect the stabilizing Cu. This is appropriate because it is not known a priori how much Nb will be converted to Nb₃Sn, and the true cross-sectional area of the superconducting component is not known. Therefore, because the superconducting fraction in the non-stabilization Cu areas are different for different wire designs, $J_{c,non-Cu}$ comparisons are not necessarily reflective of the J_c value of the A15 layer ($J_{c,layer}$). Adding to the complication is the fact that there is a 36.3% volume expansion upon conversion from Nb to Nb₃Sn. A more meaningful, but more difficult, measurement is to compare the $J_{c,layer}$ values. This involves quantitative microscopy to analyze the amount of Nb₃Sn formed within each composite, which is generally not done due to time and/or resource limitations. Examination of the necessary $J_{c,layer}$ values to reach the goal $J_{c,non-Cu} = 3000 \text{ A/mm}^2$ is one thrust of this thesis work. In the rest of this thesis, J_c implies $J_{c,non-Cu}$ unless stated otherwise.

The majority of the early work in Nb₃Sn wire manufacturing was on conductors made via the bronze route. However, the internal-Sn and PIT methods have generated much higher J_c values. One reason is that a larger fraction of the non-Cu area is Nb and Sn than in bronze wires, and thus there is more A15 phase after reaction. It is likely that internal-Sn or PIT will be used in the next high field DC magnets.

The “bronze process” was the first viable fabrication procedure of multifilamentary Nb₃Sn conductors [36]. In this process, Nb rods are inserted into a α -bronze matrix and the composite is extruded and drawn down to final size, where the wire is then heat treated to form Nb₃Sn. A drawback of this process is that the bronze work-hardens so quickly that the wires must be annealed after every 3 drawing passes (~50% area reduction). This makes the process labor-intensive and there is a risk of prematurely forming Nb₃Sn during the anneals, hampering further wire reduction. Another limitation of this process is that the maximum amount of Sn available is limited by the maximum solubility of Sn in α -phase bronze (9.1at.% Sn) (Figure 1.6). For many years, the Sn content was kept to a maximum of Cu-7at.%Sn because it was difficult to fabricate single-phase bronze with higher Sn content [37]. Recently, however, the push to make higher field conductors for nuclear magnetic resonance devices has led to new manufacturing processes for single phase, high Sn bronzes. State-of-the-art bronze wires are now manufactured with Cu-8.6at.%Sn bronze, with the best having $J_c(4.2\text{ K}, 12\text{ T}) = 980\text{ A/mm}^2$ [37].

One of the fabrication processes that has garnered much attention in recent years is the powder-in-tube (PIT) process [38]. In this process, Nb tubes in a Cu matrix are filled with various powders (NbSn₂, Sn, Cu), extruded, drawn down to final size and then heat treated to form Nb₃Sn, which grows from the inner Nb tube wall outward. It was found that Cu allows the Nb₃Sn to form at temperatures below 700°C [39]. The PIT process is advantageous because it allows for freedom in the choice of powder constituents and their relative proportions. An added bonus of using a Nb tube is that the unreacted Nb at the outer radius acts as the diffusion barrier. PIT wire also suffers less from pre-compression than

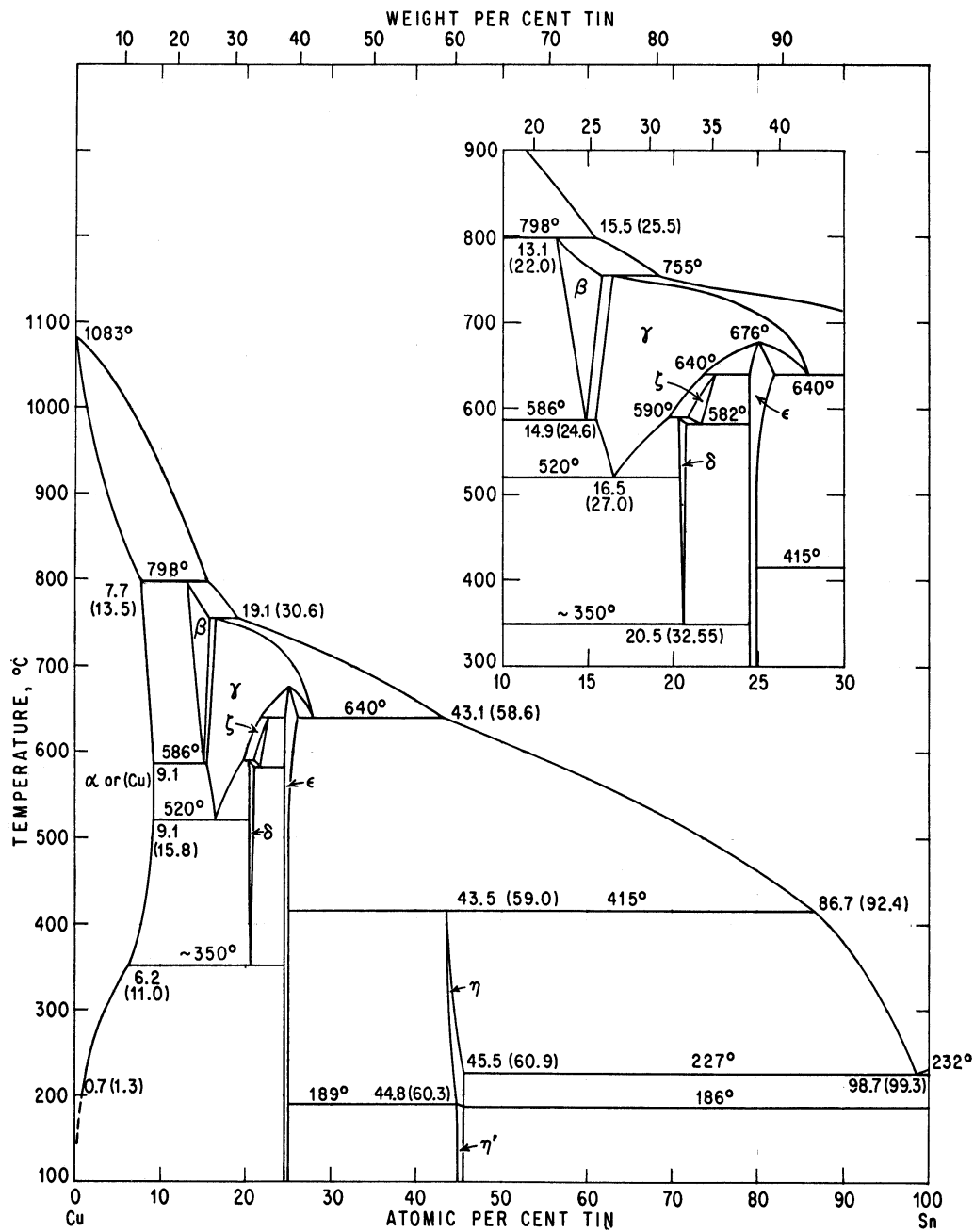


Figure 1.6. The Cu-Sn phase diagram (Adapted from [40]).

other designs because it has less Cu overall than the other designs, and the powder core after reaction has little or no strength. However, the drawbacks of this method are that the Nb tubing and special powders are expensive, making the cost per $\text{kA}\cdot\text{m}$ ($\$/\text{kA}\cdot\text{m}$) greater than the other processing routes. The best PIT wires have a $J_c(4.2\text{ K}, 12\text{ T})$ of $\sim 2200\text{ A}/\text{mm}^2$ [41].

Presently, the most common fabrication method for high J_c conductors (and the focus of this thesis) is the internal-Sn process [42]. In this process, a high Sn source is surrounded by Nb filaments in a Cu matrix, which is all surrounded by a diffusion barrier. The wires used in this thesis were all manufactured utilizing a specific technique called the Modified Jellyroll (MJR) process (Figure 1.7) [43]. In the MJR process, a nearly pure Sn core is wrapped with a double layer of Cu and expanded Nb metal, which will become the Nb filaments at final size. This stack is then surrounded by a diffusion barrier, typically Nb or a Nb-Ta alloy. This unit is called a package, bundle or sub-bundle interchangeably.

A problem with using a pure Sn core is that the wire can be difficult to process to final size because the Sn is so much softer than the other components. To remedy that, the Sn is often hardened by alloying it with a second element (e.g. Mg, Cu or Ti). Another drawback of using nearly pure Sn is that its low melting point prevents extrusion, and the wire must be fabricated by cold drawing, leading to larger drawing losses than in better bonded, extruded billets. One way around this is to use salt (NaCl) in place of the Sn during extrusion of large billets. The salt is subsequently dissolved, molten Sn alloy is poured into the openings, and the wire is then drawn to final size.

The internal-Sn process is advantageous compared to the bronze process because it allows wire processing to proceed to final size without intermediate anneals. Also, the Nb

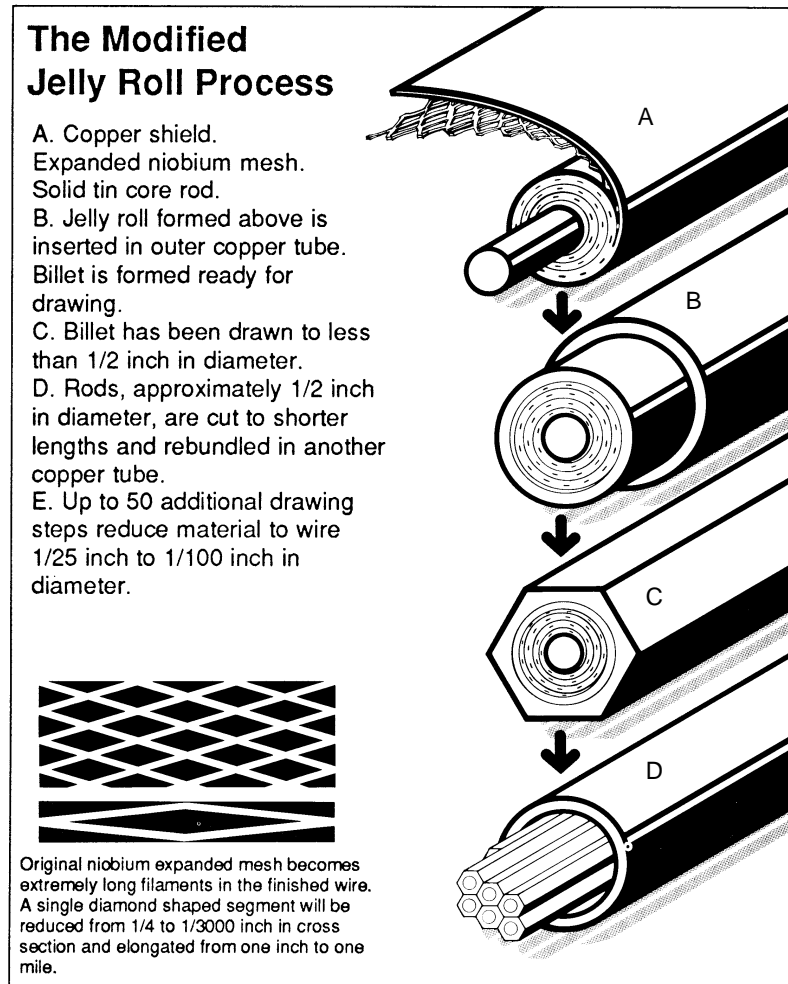


Figure 1.7. Schematic of the Modified Jelly Roll fabrication technique for internal Sn superconductors [Adapted from 44].

content is generally much higher, increasing the A15 cross-sectional area and thus $J_{c,non-Cu}$.

The primary advantage of internal-Sn over PIT is that the basic components are much cheaper, helping to keep \$/kA·m down.

1.5 Heat Treatment Issues of Internal-Sn Conductors

The optimization of heat treatments for internal-Sn wire has often been debated since many variants are possible. The heat treatments are designed to perform two functions: (1) mix the Cu and Sn, and (2) form the Nb–Sn A15 phase. Each manufacturer has its own suggested heat treatment times, temperatures and ramp rates, as illustrated in [45]. Total heat treatment times are typically between ~350 and 500 hours, 1/3 to 1/2 of which is spent on Cu–Sn mixing. The mixing heat treatment usually takes the form of several strategically placed hold temperatures, but can also be a long, slow temperature ramp. The hold temperatures are often chosen to avoid liquefaction of Sn and Cu–Sn η -phase because their melting points, 232°C and 415°C respectively, are below Nb₃Sn reaction temperatures. The hold temperatures are designed to allow these low melting point phases to transform into higher melting temperature phase(s) before the A15 reaction heat treatments at temperatures in excess of 650°C. In conductors where a goal is to minimize the interfilament contact (e.g. low AC loss conductors), there is concern about filament motion and subsequent coupling as the Cu–Sn α – ϵ interface moves through the filament stack [46] during heat treatment.

As Sn has a larger diffusion coefficient than Cu [47], Kirkendall voids appear to be an unavoidable side-effect during Cu–Sn interdiffusion. Also, the atomic volumes of the Cu–Sn phases decrease with decreasing Sn content (Figure 1.8). Therefore, voids can develop within a bundle as higher Sn content Cu–Sn phases transform to α -phase during A15 formation. The effect of such voids, however, is unclear. They slow diffusion when agglomerated and are believed to cause stress concentrations where in contact with Nb₃Sn filaments. In samples strained to ~1%, Easton and Kroeger [48] showed larger cracks near

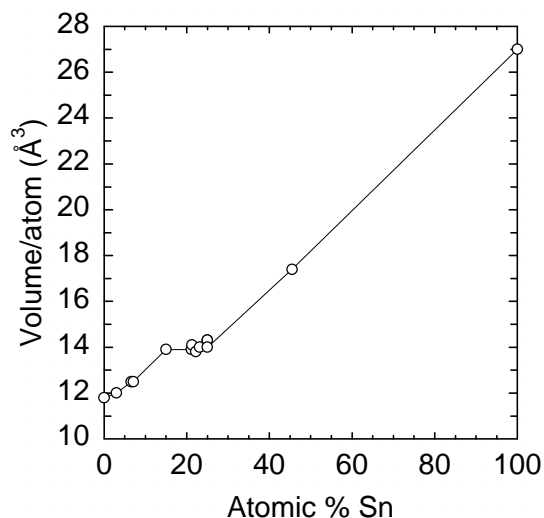


Figure 1.8. The volume per atom in the Cu–Sn system. Data points were calculated from crystal structures and lattice parameters given in [51] and [52].

voids than elsewhere along an A15 filament. However, others have not been able to decisively correlate cracks with void locations [49].

Although Sn uniformity is, in principle, a starting goal of the Cu–Sn mixing heat treatment (thus, often called the “homogenization” heat treatment), complete mixing seldom occurs in practice. It has been seen that, just prior to reaching the Nb–Sn A15 reaction temperature, the Cu–Sn matrix is not single phase [50, 54]. This sets up a situation where different Nb filaments are in contact with different Cu–Sn phases. Based on the 675°C isotherm of the Cu–Nb–Sn phase diagram (Figure 1.9), one should expect that this Cu–Sn inhomogeneity would affect the Sn composition in the individual A15 filaments and thus the superconducting properties.

It has been shown that significant shortening of the Cu–Sn mixing heat treatments can be achieved without detrimental effects to the superconducting properties. One of the

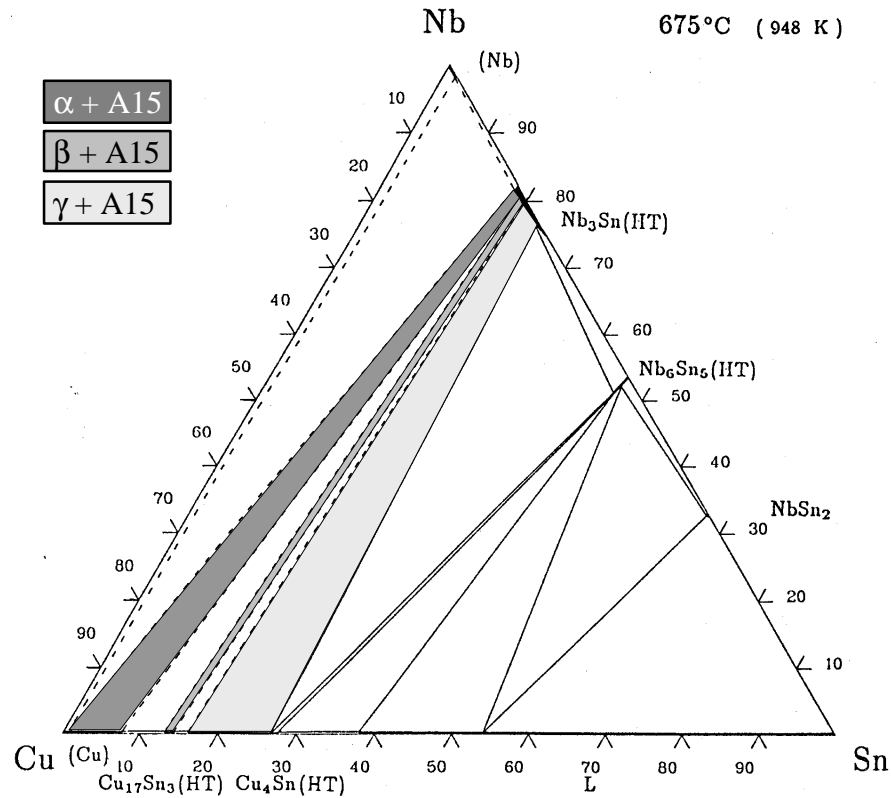


Figure 1.9. The Cu–Sn–Nb ternary phase diagram at the 675°C isotherm (the dashed lines are speculation). α , β and γ Cu–Sn phases are each in equilibrium with different A15 compositions [Adapted from 55].

supposed purposes of the $\sim 200^\circ\text{C}$ heat treatment step is to transform the Sn core into higher melting point Cu–Sn phases. While such studies are always particular to each composite design, Taillard and Verwaerde [53] and Dieterich et al. [54] reported that this heat treatment step did not completely transform the Sn core and this calls into question its purpose and value. Moreover, Dieterich et al. [54] reported that the same $J_c(4.2\text{ K})$ values were generated whether the Cu–Sn mixing portion of the heat treatment was 48 hours at 380°C (48h/380°C) or the manufacturer’s recommended 120h/200°C + 24h/380°C. Bruzek et al. [56] replaced a 175h/220°C + 96h/340°C heat treatment with 24h/375°C and achieved similar or better results in terms of J_c in each of 5 different wire designs. Barzi, Gregory and

Pyon [57] have completely removed the Cu–Sn mixing steps below 575°C and found no effect on J_c values. While shortening the Cu–Sn mixing heat treatment has had little effect, there is conflicting evidence that removing it entirely is detrimental to J_c [19, 54]. However, there is strong anecdotal evidence that liquid Sn can burst through a wire, and it is accepted that the Cu–Sn mixing step helps to minimize this risk.

There are a limited number of studies in the literature on the Nb–Sn A15 heat treatment and they are focussed on a specific wire or heat treatment, making it difficult to apply the findings to all internal-Sn wires in general. A15 layer growth rate increases with increasing temperature [19, 53], but so does A15 grain size, which is detrimental to J_c . In the A15 reaction heat treatment time versus temperature study of Dietderich et al. [54], a 650°C heat treatment generated higher J_c values than those at 700°C or 730°C. However, [57] found that 180h/650°C was not enough to fully react the 4.7 μm filaments in their composite. They go on to show that 30 to 100 hours at 700°C maximized J_c for wires with filaments < 2 μm , with shorter times appropriate for smaller filaments. In other literature, only one reaction heat treatment time was used for a given reaction temperature [25, 56, 58] making generalizations difficult.

1.6 Summary

A superconductor is needed with improved J_c at magnetic fields > 10 T and at low cost for future high field magnets. Ductile Nb–Ti has been the workhorse of the particle accelerator community, but it is generally agreed that ductile Nb–Ti is at its J_c limit. Nb₃Sn wire is common in high field laboratory magnets, and is now the best option for particle

accelerator magnets. Nb_3Sn is the stoichiometric composition in an A15 phase field which ranges from 18 to 25at.%Sn. All Nb–Sn A15 compositions are superconducting, but the superconducting properties increase with increasing Sn concentration. T_c ranges from ~6 K to 18.3 K for compositions between 18 and 25at.%Sn, respectively. H_{c2} also increases with increasing Sn concentration, although the values reported in the literature for stoichiometric Nb_3Sn are widely varied. Moreover, many of the values reported in the literature are that of H^* , not H_{c2} .

The primary flux pinning centers in Nb_3Sn are grain boundaries and thus grain size should be minimized. Grain size can be minimized by minimizing the A15 reaction temperature, however lower reaction temperatures will require longer time to fully react the Nb and Sn. There is a fine balance between minimizing grain size and maximizing Sn concentration. Third element additions, such as Ta or Ti, have been seen to decrease grain size and increase T_c , H_{c2} and A15 layer growth rate. These elements are incorporated into most Nb_3Sn conductors.

There are a number of viable Nb_3Sn wire fabrication methods including bronze, PIT and internal-Sn, and each has its own advantages and disadvantages. However, low-Cu, internal-Sn wires are the best option for the high energy physics community. This design has produced the highest J_c (4.2 K, 12 T) of any Nb_3Sn strand to date and is a relatively inexpensive process for Nb_3Sn at ~\$10/kA·m (for comparison, Nb–Ti ~ \$1/ kA·m).

Systematic studies in the literature of internal-Sn heat treatments are very limited and specific to the wire(s) examined, however evidence exists that the heat treatments are not fully optimized. Nearly half of the heat treatment time is used for the mixing of Cu and Sn,

but complete mixing has not been seen. Based on the Cu–Nb–Sn phase diagram, one might expect the local Cu–Sn phase to have an effect on the composition of the A15 phase that is formed, and thus influence the superconducting properties. Higher reaction temperatures will allow the Nb₃Sn to grow more quickly and increase the Sn concentration, but at the price of rapidly growing grains. This thesis closely examines the effects of both the Cu–Sn mixing and A15 reaction heat treatments of internal-Sn Nb₃Sn conductors.

1.7 Thesis Goals and Format

This thesis focuses on several issues surrounding optimization of internal-Sn heat treatment, superconducting properties and wire design:

- a. What level of Cu and Sn mixing can be achieved prior to the A15 reaction heat treatment?
- b. What are the superconducting ramifications of incomplete Cu–Sn mixing?
- c. How do the superconducting properties change with variations in the A15 reaction heat treatment and composite make-up?
- d. How do changes in the wire components effect $J_{c,non-Cu}$?

In Chapter 2, two very different internal-Sn wire designs (low-Cu and high-Cu) are given 20 different Cu–Sn mixing heat treatments to determine if it is ever possible to completely mix Cu and Sn in under 150 hours. The Cu–Sn phases present after 10 different heat treatment temperatures and at 2 different heat treatment times are identified. As there is anecdotal evidence that Cu–Sn δ -phase has a deleterious effect on the superconducting

properties, this work will show at which temperatures it forms. The first reported Cu–Nb–Sn ternary phase is discussed, which forms as a result of dissolution of the Nb filaments.

Chapter 3 examines whether the Cu–Sn microstructure surrounding the Nb filaments has any measurable effect on the superconducting properties in fully reacted wires. Various Cu–Sn microstructures were generated by varying the temperature ramp rate to the A15 reaction temperature. This was followed by a full reaction heat treatment of 180h/650°C. If the Cu–Sn microstructure does not play a role in the superconducting properties, it would remove one factor for performance differences between wires, leaving only the Nb–Sn A15 reaction heat treatment and the wire design as influencing factors.

Chapter 4 is a global investigation of internal-Sn superconducting properties and wire design, as five distinct composites are studied. The effect of the Cu:Nb:Sn ratio within the bundle and alloying element in the core on the superconducting properties are examined. A universal correlation is found between T_c and H^* . Also, consequences of allowing Sn to escape the bundle are clearly shown.

Chapter 5 discusses internal-Sn design issues and methods to increase $J_{c,non-Cu}$. The value and cost of each bundle component is discussed in terms of its effect on J_c . It is found that given the presently reported values of $J_{c,layer}$ in the literature, it should be possible to reach the HEP goal of $J_{c,non-Cu}(4.2\text{ K}, 12\text{ T}) = 3000\text{ A/mm}^2$. Moreover, calculations on the internal-Sn conductor with the highest $J_{c,non-Cu}$ to date (2900 A/mm^2 at 42 K, 12 T) indicate that 3220 A/mm^2 is possible without going to extraordinary processing or heat treatment lengths.

Chapter 6 summarizes the findings of this thesis.

CHAPTER 2 – Cu–Sn PHASE FORMATION

There are many possible heat treatment schedules for the mixing of Cu and Sn. In the few studies in the literature, the Cu–Sn mixing is incomplete at the beginning of the A15 reaction heat treatment. A natural question is therefore whether it is ever possible to completely mix the Cu and Sn. This chapter addresses this issue and, in the process, determines which of the Cu–Sn phases will form after various heat treatment temperatures and times.

2.1 Wire Characteristics

The two wires examined in this chapter were manufactured via the MJR, internal-Sn process by Teledyne Wah Chang (now Wah Chang), and their characteristics are listed in Table 2.1. The overall Cu:Sn ratio within the barrier was determined by digital image

TABLE 2.1
CHARACTERISTICS OF CRE1912 AND CRE1721

Conductor	Diameter	Sn core alloy	Barrier	Filaments	Cu–Sn Composition*
CRE1721	0.8 mm	Sn–9at.%Mg	Ta–56at.%Nb	Nb–2at.%Ti	Cu–12at.%Sn
CRE1912	0.5 mm	Sn–9at.%Mg	Nb	Nb–2at.%Ti	Cu–29at.%Sn

* Overall composition within the bundle assuming full mixing

analysis techniques described in Appendix A. One of the examined wires, designated CRe1721, was designed for low AC losses [59] and is shown in Figure 2.1. It contains 14 filament bundles each consisting of a Sn–9at.%Mg core surrounded by Cu and widely spaced Nb–2at.%Ti filaments, and has a Ta–56at.%Nb (Ta–60wt.%Nb) diffusion barrier. The wire diameter is 0.8 mm and the overall Cu–Sn composition within the diffusion barrier is Cu–12at.%Sn, which is slightly greater than the maximum Sn content of α -phase bronze (Cu–9.1at.% Sn). It was believed that the widely spaced filaments of this design would facilitate identification of the Cu–Sn phases formed during the Cu–Sn mixing heat treatments.

The second conductor examined was CRe1912 (0.5 mm diameter) (Figure 2.2), which has 54 filament bundles with a Sn–9at.%Mg core surrounded by a double-wrap of Cu and expanded Nb–2at.%Ti mesh and a Nb diffusion barrier. It had an overall Cu–Sn composition of Cu–29at.%Sn, which about twice that of CRe1721 and slightly greater than the composition of ϵ -phase (Cu–25at.%Sn). This higher Sn concentration is the result of replacing much of the Cu from the CRe1721 design with Nb and Sn, effectively increasing the $J_{c,non-Cu}$. The 0.7 mm diameter version of CRe1912 (which is discussed in chapters 3 and 4) generated a $J_c(4.2 \text{ K}, 12 \text{ T}) = 2200 \text{ A/mm}^2$ [60]. The general design types that CRe1721 and CRe1912 represent will also be referred to as high-Cu and low-Cu, respectively, in this thesis.

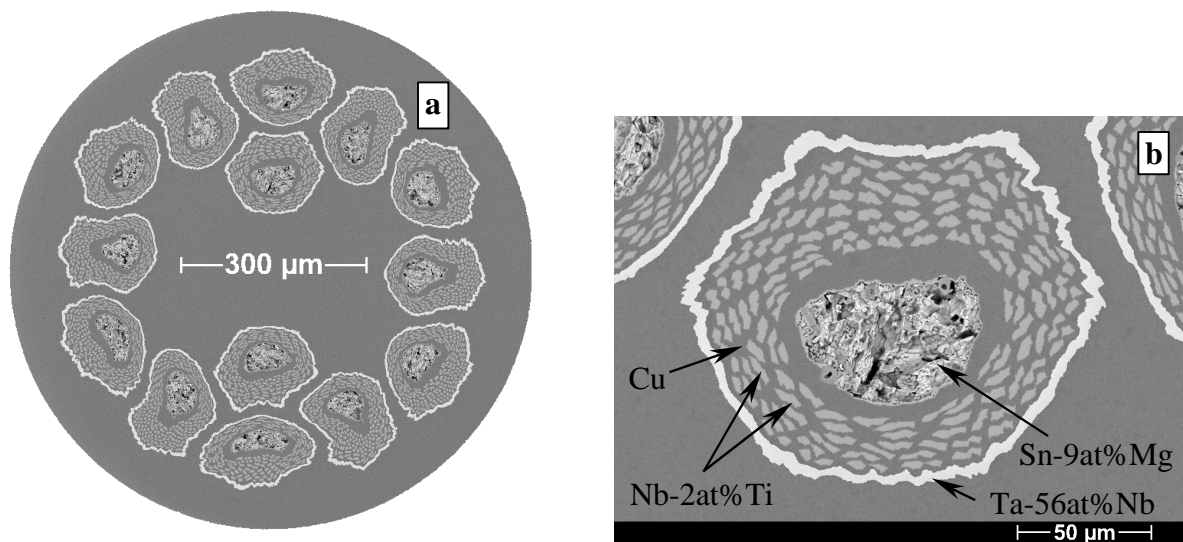


Figure 2.1. SEM-BSE images of CRe1721 (a) wire and (b) bundle cross-sections prior to heat treatment.

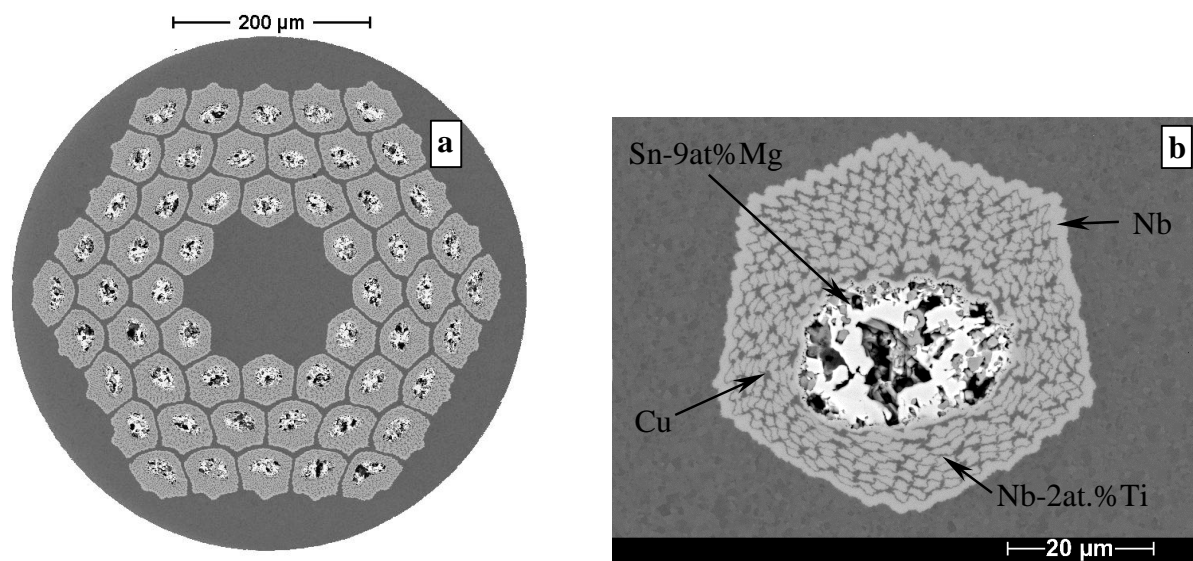


Figure 2.2. SEM-BSE images of the CRe1912 (a) wire and (b) bundle cross-sections prior to heat treatment.

2.2 Experimental Procedure

One of the problems with internal-Sn wire is that special precautions must be taken to prevent liquid Sn from leaking out of the ends of the cut wires during heat treatment. One common method to deal with this is to keep the Sn at the ends of the wire below the Sn melting point (i.e. solidified), trapping any liquid Sn inside. This usually entails heat treating a long sample such that the ends extend outside the furnace and/or are in contact with a heat sink that is below the melting point of Sn. The drawback of using the cold-ends technique is that much material is wasted. A more sample-efficient method is to crimp the ends of the wire closed. However, the crimping is often incomplete as microscopic openings can remain. Also, the diffusion barrier is damaged in the crimped region, giving the Sn another possible escape path. Often, the end result is a wire where Sn still leaks out of the ends.

A better method to seal the ends, and the one used for wires in this thesis, is to electroplate Cu onto the ends of the cut wires. A complete description of the Cu plating system can be found in Appendix B. It was assumed that the ends of the wires would be compromised by Sn diffusing into the plated Cu region, but it was not believed that this would effect the Sn content within the bundles away from the ends. To alleviate the concern, typically the last 1 cm of wire was discarded after heat treatment to avoid these end effects.

After Cu-plating the ends, one ~80 mm long sample from each of CRe1721 and CRe1912 were sealed together in an evacuated quartz tube (6 mm O.D., 4 mm I.D.) under ~30 mTorr of Ar and inserted into a pre-heated, 5 cm bore, horizontal tube furnace for 24 or 150 hours. 150 hours was chosen as the upper limit because this is approximately the time used for Cu-Sn mixing in standard heat treatments. 24 hours was considered short enough to

identify phases that might transform to other phases by 150 hours. The temperatures were approximately 10°C above and below the temperature invariants of the Cu–Sn system below 600°C (the exact temperatures are listed in Table 2.2 with the results). 600°C was chosen as the upper limit to avoid significant Nb₃Sn formation. After removal from the furnace, the quartz tubes were water quenched. The Cu–Sn phases were examined by light microscopy (LM), backscatter scanning electron microscope (SEM-BSE) imaging and energy dispersive spectroscopy (EDS).

2.3 Cu–Sn Phase Identification

Examples of the SEM-BSE images taken after 24 and 150 hours at ~360°C (just above the δ eutectoid) are shown in Figures 2.3 and 2.4. The phases found after all heat treatments are compiled in Tables 2.2 and 2.3, where the Cu–Sn phases are arranged from lowest to highest Sn content from left to right. The trend in the Cu–Sn phase development in each wire as temperature and time increased is toward the average Cu–Sn composition within the diffusion barrier. However, there is a shift toward α -phase at high temperature in CRe1912. No δ -phase was visible between α and ϵ phases at temperatures where it is thermodynamically stable (above 350° C). SEM-BSE and LM resolution limits might have prevented the detection of δ -phase in CRe1912 wire due to the closely spaced filaments, but this was not a factor for CRe1721. The Mg from the Sn core was seen to form a Cu–Sn–Mg ternary phase, the composition of which changed from approximately Cu-29at.%Sn-36at.%Mg at ~218°C to Cu-15at.%Sn-15at.%Mg after heat treatments at 510°C and above. Mg was not detected outside the Cu–Sn–Mg ternary phases.

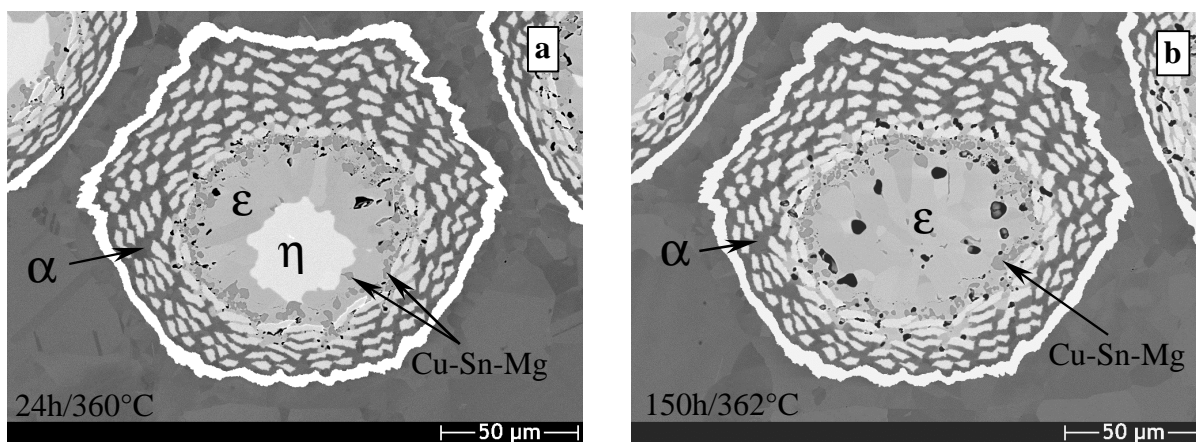


Figure 2.3. SEM-BSE images of the CRe1721 wire after (a) 24h/360°C and (b) 150h/362°C. The Cu-Sn and Cu-Sn-Mg phases are labeled.

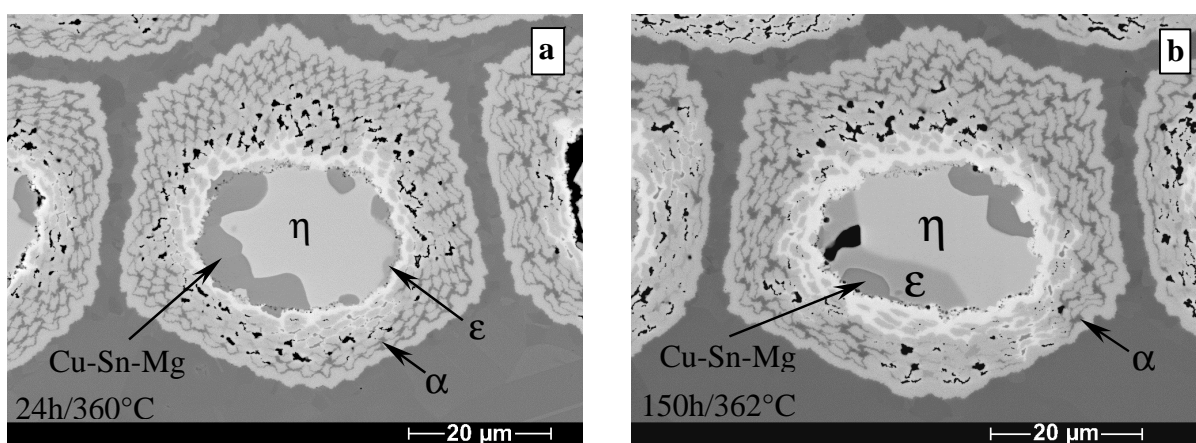


Figure 2.4. SEM-BSE images showing the phases formed in CRe1912 after (a) 24h/360°C and (b) 150h/362°C. The Cu-Sn and Cu-Sn-Mg phases are labeled. The bright ring around the core may be a Cu-Sn-Nb ternary (See Figure 2.5).

Void formation was seen in all strands and after all heat treatments. The voids had initially formed in the core region, but moved toward the barrier and amongst the filaments as time and temperature increased. It appeared that the voids moved outward with the α -phase boundary. In CRe1721, the voids stopped within the first few rows of filaments, but in CRe1912, the voids were distributed throughout the filament stack.

A bright ring can be seen near the inner most ring of filaments in CRe1912 (Figure 2.4). It is believed that this is an as yet unreported Cu–Sn–Nb phase, and this will be discussed in greater detail in Section 2.5.

2.4 Discussion

Based upon the data presented in Tables 2.2 and 2.3, it is unlikely that Sn can be distributed uniformly by the time the A15 reaction heat treatment begins in commercial wires. This might be expected, as the average Cu–Sn composition for each wire does not fall within a single Cu–Sn phase region. For example, the average composition of CRe1912 is Cu-26at.%Sn and thus one would expect that only ϵ and η phase would be present at equilibrium. However, no heat treatment generated such a Cu–Sn microstructure. Moreover, as evidenced by the Cu–Sn phases present 150h/402°C or 24h/426°C, the average Sn composition in the Cu–Sn matrix had fallen below the initial non-heat treated composition. This Sn depletion is due to premature Nb–Sn A15 formation. Preliminary T_c measurements showed that both CRe1912 and CRe1721 heat treated for 24h/426°C had T_c values above that of pure Nb (9.3 K) indicating Nb–Sn A15 phase formation. The A15 phase possibly formed at even lower temperatures, but was not detected due to the low T_c of Sn-poor A15 phase

TABLE 2.2
Cu-Sn PHASES FOUND IN CRE1721

Heat Treatment Temperature (24h/150h)	Cu-Sn Phases Detected							Pure Sn	Mg-Cu-Sn Ternary
	α	β	γ	δ	ζ	ϵ	η		
218°/217° C	✓◆					✓◆	✓◆	✓◆	✓◆
237°/239° C	✓◆					✓◆	✓◆		✓◆
335°/342° C	✓◆					✓◆	✓		✓◆
360°/362° C	✓◆					✓◆	✓		✓◆
401°/402° C	✓◆			✓◆		✓◆			✓◆
426°/428° C	✓◆			✓◆		✓◆			✓◆
510°/510° C	✓◆			✓◆					✓◆
528°/533° C	✓◆		✓◆						✓◆
569°/569° C	✓◆		✓						✓◆
599°/604° C	✓◆	✦	✦		✦				✓◆

✓ = 24 hour heat treatment ◆ = 150 hour heat treatment
 ✦ = Refined microstructure after 24h; might have been
 formed from a eutectoid decomposition of this phase
 Shaded areas indicate where a given phase is not stable

TABLE 2.3
Cu-Sn PHASES FOUND IN CRE1912

Heat Treatment Temperature (24h/150h)	Cu-Sn Phases Detected							Pure Sn	Mg-Cu-Sn Ternary
	α	β	γ	δ	ζ	ϵ	η		
218°/217° C	✓◆					✓◆	✓◆	✓	✓◆
237°/239° C	✓◆					✓◆	✓◆		✓◆
335°/342° C	✓◆					✓◆	✓◆		✓◆
360°/362° C	✓◆					✓◆	✓◆		✓◆
401°/402° C	✓◆					✓◆	✓		✓◆
426°/428° C	✓◆					✓◆			✓◆
510°/510° C				✓◆		✓◆			✓◆
528°/533° C				✓◆		✓◆			✓◆
569°/569° C	◆		✓	✓		✓			✓◆
599°/604° C	✓◆	✦	✦		✦				✓◆

✓ = 24 hour heat Treatment ◆ = 150 hour heat treatment
 ✦ = Refined microstructure after 24h; might have been
 formed from a eutectoid decomposition of this phase
 Shaded areas indicate where a given phase is not stable

being masked by the Nb transition (Recall, $T_c \sim 6$ K for Nb-18at.%Sn). By using x-ray analysis techniques, Taillard and Ustinov [61] reported the formation of Nb–Sn A15 phase in internal-Sn composites in as little as 1 hour at 220°C. The superconducting properties, however, were not reported. The lack of Cu–Sn phase homogeneity and the early A15 phase formation calls into question the value of the Cu–Sn mixing step, if it is not possible to be fully mixed prior to A15 formation.

There was an often expressed concern in the Nb₃Sn community that Cu–Sn δ -phase has a deleterious effect on A15 formation, without however explicit supporting evidence. This concern is the reason why there is usually a hold temperature below 350°C, the lowest temperature that δ -phase is stable. We fully expected that δ -phase would form above 350°C between the α and ϵ phases. However, there was a noticeable lack of δ -phase after both 24 and 150 hours at 360°C in CRe1721 and at 360°, 401° and 427°C in CRe1912. Onishi and Fujibuchi [62] and Verhoeven et al. [63] also observed a lack of δ -phase formation in Sn-plated Cu sheet at temperatures between ~350° and ~400°C. We thus conclude that concerns about δ -phase formation under 400°C are unfounded. If Cu–Sn δ -phase remains a concern for A15 development, the ~340°C heat treatment step can be increased to near 400°C without δ -phase formation occurring.

In CRe1721, much of the original Sn core had not transformed into higher melting point Cu–Sn phases after 150h/217°C. This heat treatment is both hotter and longer than the manufacturer's recommended low temperature step of 120h/185°C, which was presumably designed to remove the Sn core. In contrast, the Sn core of CRe1912 was fully transformed after 150h/217°C. The likely cause of this difference is the diffusion distances are roughly

twice as long in CRe1721. This highlights the fact that, to maximally mix the Cu and Sn, heat treatment schedules should be optimized for each composite. As is the case now, heat treatment schedules are highly similar from composite to composite. The remnant Sn core in CRe1721 is similar to the results of Taillard and Verwaerde [53] and Dietderich et al. [54] and the three results calls into question the ability of any heat treatment step near 200°C to transform the Sn core. It is more likely that the true effect of this step is to produce protective layers of ϵ and η phases, encasing the Sn core and helping to prevent Sn-burst.

Sn-burst is a phenomenon in which liquid Sn ruptures the wire. Although we have not seen Sn-burst in any of the wires discussed in this thesis, the probability of it occurring increases with sample length, possibly due to the increased probability of encountering weak diffusion barrier regions. Sn-burst probability is also increased if cabling of the wire sufficiently reduces the integrity of the diffusion barrier. While the ability to fully mix the Cu and Sn is doubtful, one function of the Cu–Sn mixing heat treatment is that it does reduce the risk of Sn-burst.

2.5 Discovery of a Cu-Nb-Sn Intermetallic

Figure 2.4 shows a bright ring surrounding the inner-most filaments of CRe1912. At first, this was thought to simply be early A15 formation. However, suspicious areas of similar brightness were also found extending into the core region of CRe1912 as shown in Figure 2.5. When the heat treatment temperature was at or below 401°C, the bright region appeared to be single phase down to the ~100 nm resolution of the SEM-BSE detection limit.

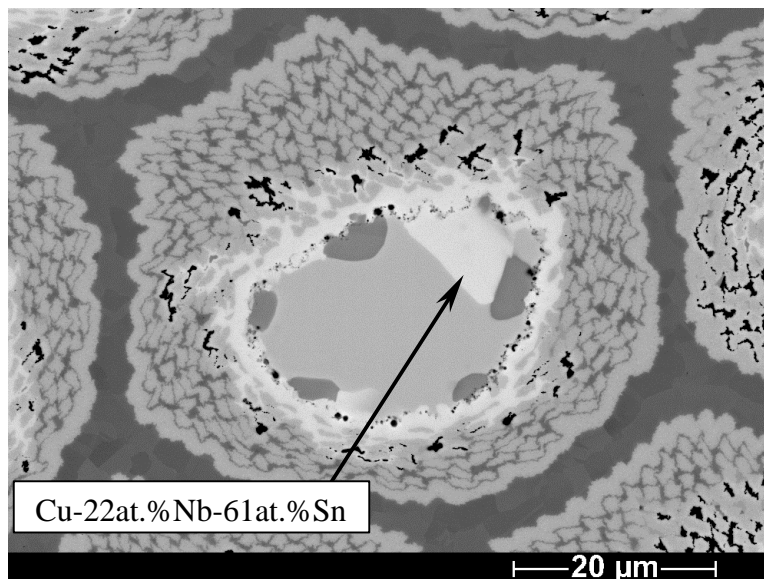


Figure 2.5. SEM-BSE image of CRe1912 showing Cu–Sn–Nb ternary in the core region after 150h/362°C. The ternary appears to be single phase down to 100 nm.

However, at 428°C and above, those regions were clearly multi-phase (Figure 2.6). This was true of the unknown phases in both the core and among the filaments.

Whereas the bright material within the filaments was too small for accurate EDS analysis, the material extending into the core was large enough to be analyzed. A 10 minute EDS analysis (in “standardless” mode) on the single phase material gave a composition of Cu-22at.%Nb-61at.%Sn. EDS measurement of the multi-phase region gave a composition of Cu-20at.%Nb-30at.%Sn, which is the average composition of this region. The phases comprising the multiphase region were too small to probe individually and may simply be known binaries. The apparent decomposition at 428°C suggests that the multi-phase region is also not any of the Nb–Sn intermetallics (NbSn_2 , Nb_6Sn_5), as they first decompose at 845°C [10].

The Cu–Nb–Sn ternary discovery in CRe1912 prompted a close re-examination of the

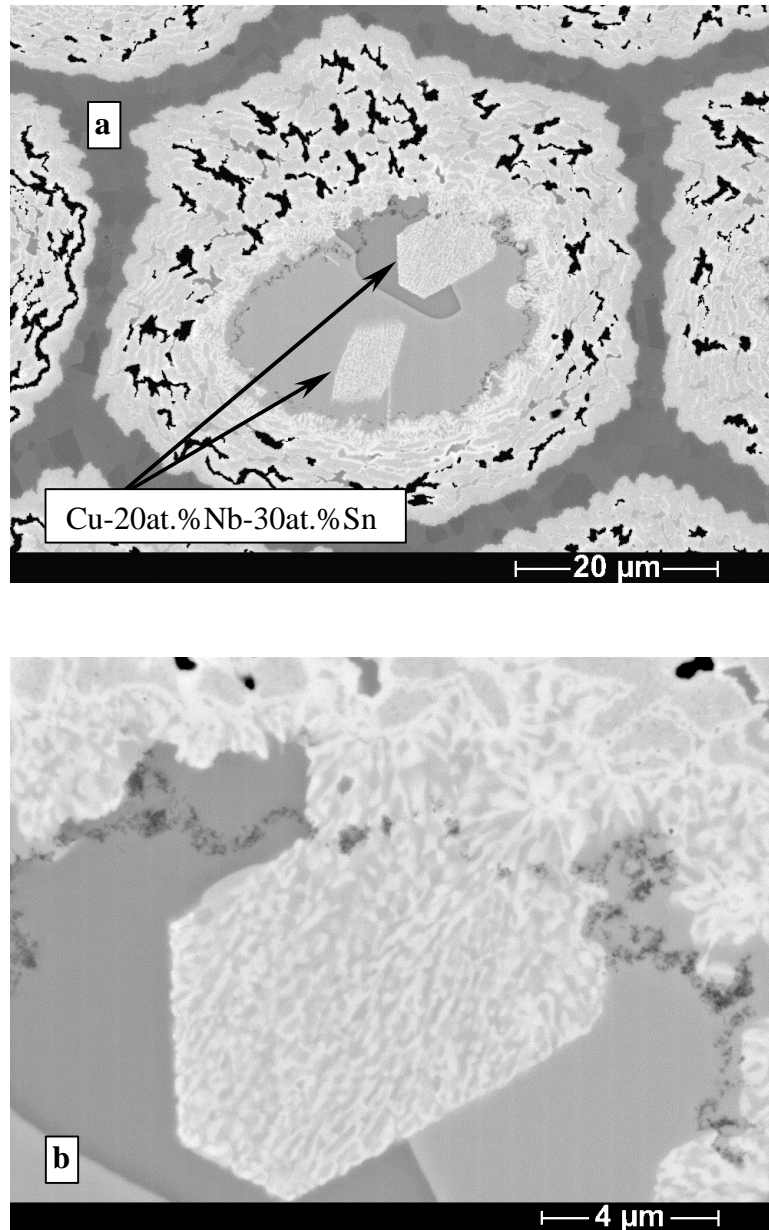


Figure 2.6. (a) Multiphase structure found growing into the core of CRe1912 after 150h/510C. (b) Magnified view of the same structure as in (a) more clearly showing the multi-phase structure.

of area surrounding the Nb filaments in CRe1721. Again, a single phase region is seen to have formed around the filaments after heat treatment temperatures at or below 401°C and a multiphase region formed at or above 428°C (Figure 2.7). Although the areas in question in CRe1721 were too small for EDS analysis, it is assumed that it is the same phase probed in CRe1912 due to the similar SEM-BSE image brightness and similar single-phase/double-phase nature with respect to heat treatment temperature. An additional insight from CRe1721 is that this Cu–Nb–Sn ternary only appeared where higher Cu–Sn phases (i.e. non- α phases) were in contact with the Nb.

Cu–Sn–Nb phase formation is a cause for concern as its growth requires the dissolution of Nb and thus a reduction of the longitudinally continuous area Nb filaments, reducing $J_{c,non-Cu}$. Even if this new ternary phase transforms into the Nb–Sn A15 phase at higher temperatures, it still forms unconnected nodules that are not able to pass supercurrent along the length of the wire. The deleterious effects of this phase on J_c were confirmed in a very low Cu, high Sn composite (ORe137, discussed in Chapter 4) [64]. The Cu–Nb–Sn phase is thus a serious impediment to increasing J_c by simply increasing the Sn:Cu ratio within the bundles.

An attempt was made to produce the Cu–Sn–Nb phase directly through mixing the appropriate amounts of –325 mesh Cu, Sn and Nb powders. The powders were mixed and pressed into a cylindrical pellet ~5 mm in diameter and ~15 mm long. The pellet was sealed in a quartz tube under ~ 30 mTorr of Ar, and then inserted into a preheated furnace at 210°C for 360 hours. This heat treatment was to bind as much Sn as possible into a Cu–Sn phase, allowing for a subsequent heat treatment at a temperature above the melting point of Sn, and

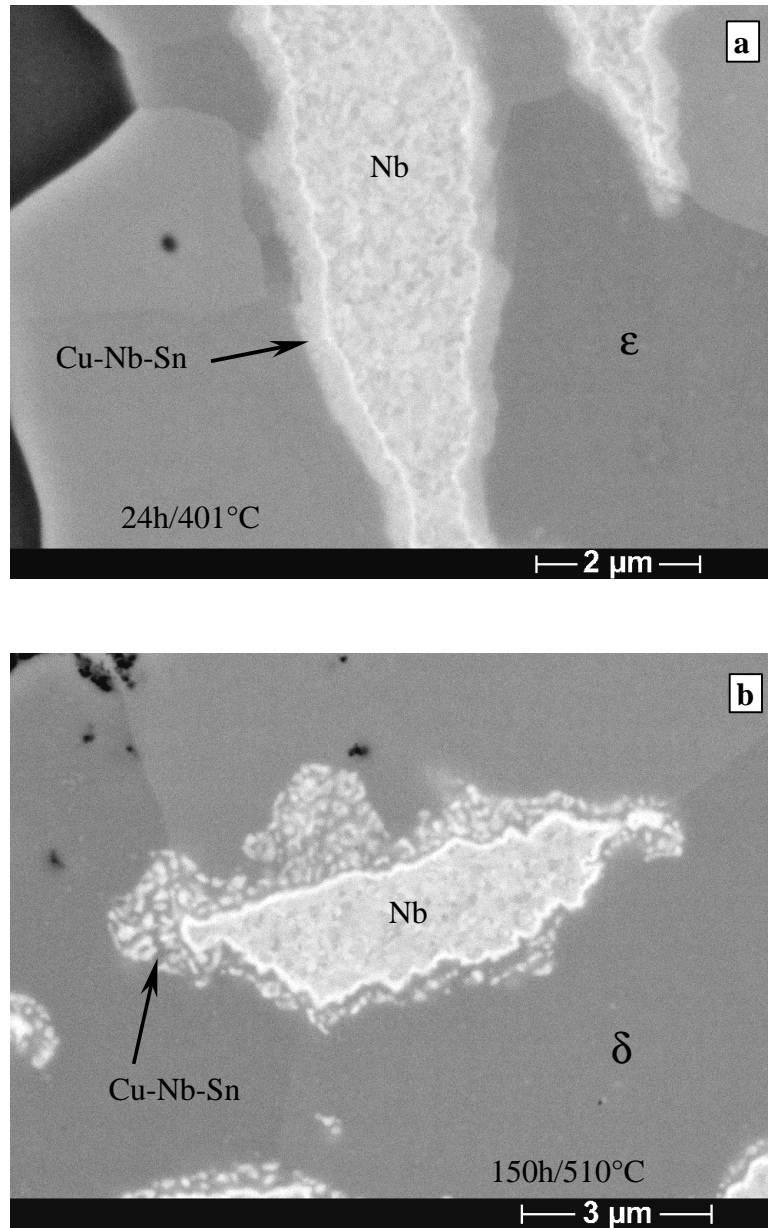


Figure 2.7. SEM-BE images of what is believed to be Cu-Nb-Sn ternaries surrounding the Nb filaments in CRe1721 after (a) 24h/401°C and (b) 150h/510°C. Nb dissolution was only seen when non- α Cu-Sn phases were in contact with the filaments.

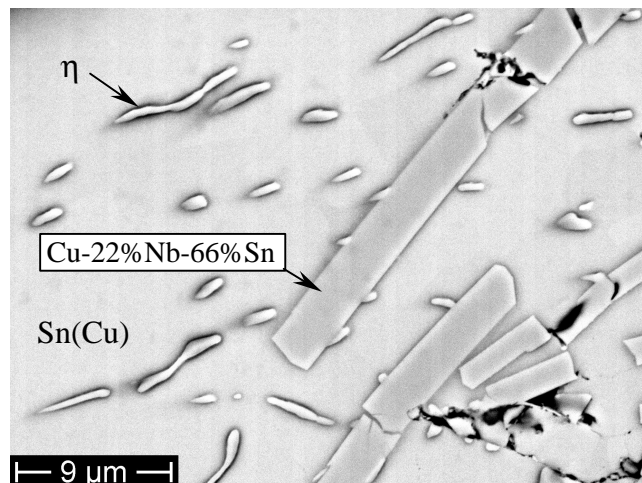


Figure 2.8. SEM-BSE image of Cu–Nb–Sn particles formed from the pellet of mixed Nb, Sn, and Cu powders. EDS analysis showed that composition was Cu-22at.%Nb-66at.%Sn, which is slightly higher in Sn than that found in CRe1912. The small ribbons are too small to be accurately identified, but EDS analysis indicates that they are Cu–Sn η -phase.

thus minimize the loss of liquid Sn. Analysis of the pellet after the 210°C anneal revealed that the vast majority of the pellet was comprised of Nb, η -phase and pure Sn. There was a small amount of Cu remaining at the center of what had originally been a few large Cu particles.

To form the Cu–Nb–Sn phase, the pellet was resealed in quartz under 30 mTorr of Ar and given a heat treatment of 160h/380°C. SEM-BSE examination revealed that the pellet still contained mainly Nb and η -phase particles surrounded by Sn. The Cu–Sn–Nb phase was found as small rectangular particles (2 to 4 μm across and 10 to 20 μm long) within the Sn matrix and had a composition of Cu-22at.%Nb-66at.%Sn (Figure 2.8). This is slightly higher in Sn than the single phase material examined in CRe1912. The difference might be due to a strong Sn signal from the surrounding Sn matrix, which is common when analyzing such thin particles. It may also be indicative of some solid solubility in the ternary phase. In order to generate a larger quantity of the Cu–Nb–Sn phase, either longer heat treatment time

is required or the diffusion distances needs to be reduced either by using smaller particle sizes or mechanically alloying the powders.

2.6 Summary

The Cu–Sn phases formed after 24 or 150 hours at 10 different temperatures were identified for 2 very different internal-Sn conductor designs. It was not possible to achieve a homogenous mixture of Cu and Sn for any heat treatment. While this might simply be the result of the Cu–Sn composition being between the single-phase regions of the Cu–Sn phase diagram, it is unlikely that Cu–Sn homogeneity is possible in any commercial internal-Sn wire. Concerns over δ -phase formation at the typical $\sim 340^\circ\text{C}$ heat treatment temperatures appear to be unfounded, as our results confirm that δ -phase does not readily form at temperatures below 400°C . The standard 200°C heat treatment step does not fully transform the Sn core when diffusion distances are large ($\sim 50\ \mu\text{m}$). It is likely that the true function of this heat treatment step is to encase the Sn core in higher melting point Cu–Sn phases and thereby help protect the wire from Sn-burst. The first Cu–Nb–Sn ternary phase has been discovered, having a composition of Cu-22at.%Nb-61at.%Sn. It appears to only form when a non- α Cu–Sn phase is in contact with Nb at temperatures below 400°C . Since it dissolves the Nb filaments and forms disconnected nodules in the core, it has a deleterious effect on $J_{c,non-Cu}$, even if it subsequently converts to Nb–Sn A15 phase.

CHAPTER 3 – Cu–Sn HOMOGENEITY EFFECTS ON THE FINAL SUPERCONDUCTING PROPERTIES

The evidence presented in Chapter 2 shows that complete mixing of Cu and Sn in commercial internal-Sn wires prior to the A15 reaction heat treatment is highly unlikely. This forces the Nb filaments to start the A15 reaction with one or more different Cu–Sn phases depending on the level of Cu–Sn mixing. According to the available Cu–Nb–Sn phase diagram (Figure 1.9), the Cu–Sn phases are each in equilibrium with a different sub-stoichiometric portion of the Nb-Sn A15 phase. However, the discovery of a Cu–Nb–Sn phase (Chapter 2) shows that Figure 1.9 needs to be re-evaluated. Whether Figure 1.9 or some more complex diagram is valid, the A15 phase could have varying Sn composition (and therefore varying superconducting properties) as a consequence of the variability of the pre-reaction Cu–Sn phases. In this chapter, the superconducting properties of 2 wires (different from those in Chapter 2) are examined that were ramped from room temperature to 650°C at various rates and then given a full A15 formation heat treatment of 180h/650°C. The purpose of varying the ramp rates was to generate various Cu–Sn microstructures prior to the A15 formation heat treatment and to thus determine what effect the Cu–Sn microstructure would have on the superconducting properties of fully reacted samples.

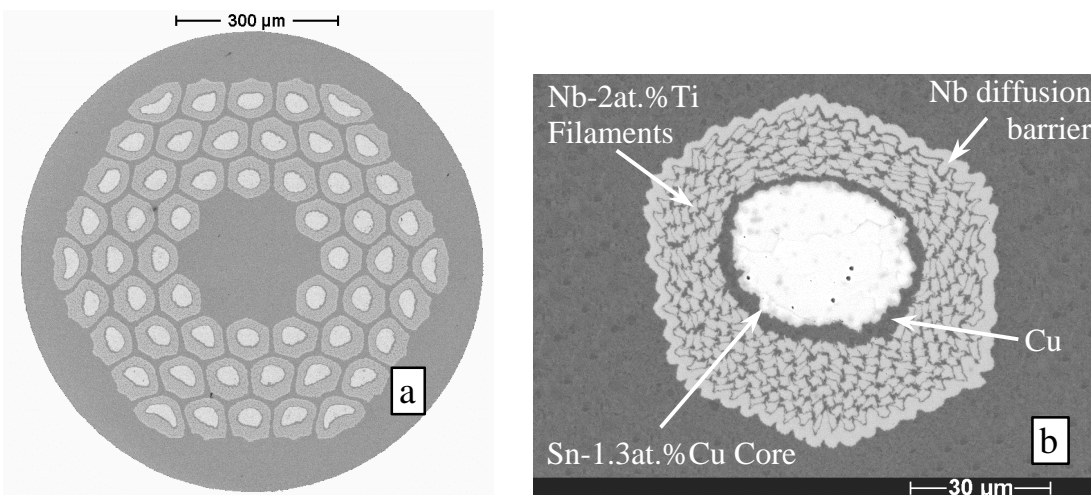


Figure 3.1. Backscatter scanning electron microscope images of ORe102 (a) wire and (b) bundle cross-section prior to reaction.

3.1 Wire Characteristics

One of the 2 wires in this study was designated ORe102 (0.8 mm diameter) and was manufactured using the MJR process by Oxford Instruments – Superconducting Technology (OIST) (Figure 3.1). It has 54 bundles, each bundle consisting of a Sn-1.3at.%Cu core surrounded by alternating layers of Cu sheet and Nb-2at.%Ti mesh with a Nb diffusion barrier. The second wire was the same CRe1912 wire from Chapter 2, but at 0.7 mm diameter (see Figure 2.2) instead of 0.5 mm. CRe1912 at the larger diameter was studied because it was at this size that CRe1912 generated its highest reported J_c , and it would thus have its best superconducting properties in general. The physical characteristics of CRe1912 and ORe102 are listed in Tables 3.1 and 3.2.

Table 3.2 lists the atomic Cu:Nb:Sn ratios of the bundles derived from digital SEM-BSE image analysis on polished cross-sections similar to that shown in Figure 3.1(b). The Nb barriers of low-Cu wires like these are designed to react significantly to maximize the

TABLE 3.1
ORE102 AND CRE1912 WIRE CHARACTERISTICS

Wire Designation	Diameter	# of Bundles	Core	Filaments	Barrier
CRE1912	0.7 mm	54	Sn-9at.%Mg	Nb-2at.%Ti	Nb
ORE102	0.8 mm	54	Sn-1.3at.%Cu	Nb-2at.%Ti	Nb

potential A15 cross-sectional area. Thus, Table 3.2 shows the Cu:Nb:Sn ratios both with and without the Nb barrier. Excluding the barrier, the Nb:Sn ratios before reaction were 2.60:1.00 (Nb-27.8at.%Sn) and 2.51:1.00 (Nb-28.5at.%Sn) for CRE1912 and ORE102, respectively, and thus both composites would be Sn-rich. However, when including the barrier, these ratios increased to 3.53:1.00 (Nb-22.1at.%Sn) and 3.49:1.00 (Nb-22.3at.%Sn) for CRE1912 and ORE102, and they would thus be sub-stoichiometric.

The highly aspected bundles situated at the corners of the hexagonal stack of bundles (see Figure 3.1a) have similar Cu:Nb:Sn ratios to the symmetric inner-ring bundles used for the data in Table 3.2. For an aspected corner bundle of CRE1912, the Cu:Nb:Sn ratios were 1.91:2.48:1.00 (Nb-28.7at.%Sn) and 1.91:3.37:1.00 (Nb-22.9at.%Sn), when excluding and including the barrier, respectively. This is in contrast to that of a symmetric inner bundle of CRE1912, where the Cu:Nb:Sn ratios were 1.81:2.60:1.00 and 1.81:3.53:1.00 excluding and including the barrier, respectively. Similar Cu:Nb:Sn ratio differences were found for ORE102. Since they represent the extremes in bundle deformity, it is believed that the highly

TABLE 3.2
Cu:Nb:Sn RATIOS PRIOR TO A15 REACTION

Wire	Including Barrier				Not Including Barrier			
	Cu	Nb	Sn	Composition	Cu	Nb	Sn	Composition
CRE1912	1.81	3.53	1.00	Nb-22.1 ^a %Sn	1.81	2.60	1.00	Nb-27.8 ^a %Sn
ORE102	2.13	3.49	1.00	Nb-22.3 ^a %Sn	2.13	2.51	1.00	Nb-28.5 ^a %Sn

aspected outer bundles and the symmetric inner bundles represent the high and low limits, respectively, in relative Sn content within a given wire. Therefore, the Cu:Nb:Sn ratios used here represent the bundles which are the weakest links in the strand in terms of Sn availability and, very likely, the superconducting properties.

3.2 Experimental Procedure

The wires were Cu plated and an ~80 mm long sample from each of ORe102 and CRe1912 was sealed in the same quartz tube to ensure that they received the same heat treatment. The heat treatments consisted of controlled temperature ramp rates of 6°C, 30°C or 60°C per hour from room temperature (RT) to 650°C. Also, one set of samples was inserted directly into a pre-heated furnace at 650°C, where it is estimated the samples reached 650°C within 2 to 3 minutes. All samples were subsequently reacted for 180 hours at 650°C, then water quenched. Comparison of these simple heat treatments was made to a more complex, but standard, manufacturer's heat treatment of 120h/185°C (solid state mixing below the melting point of Sn) + 72h/340°C (solid state mixing below the formation temperature of δ phase Cu–Sn) + 180h/650°C, with a ramp rate of 60°C/h between hold temperatures. After reaction, approximately 10 mm was removed from the ends of the samples to avoid effects from Sn diffusion into the Cu-plated ends.

The T_c values were inductively measured using a Superconducting Quantum Interference Device (SQUID). The sample was mounted on clear plastic straws with its axis parallel to both the straw axis and the applied field. Clear plastic straws are used because of their small magnetization. Samples were zero-field cooled to 6 K, where 5 mT was applied

and the magnetic moment was measured upon warming in 0.1 K steps to 20 K. Although not needed for the results of this chapter, the technique for determining T_c is shown in Figure 4.2.

H^* was measured at 4.2 and 12 K using a 14 T vibrating sample magnetometer (VSM). 12 K was chosen because, prior to this work, it was believed that $H_{c2}(12\text{ K})$ lies near 13 T, which is just within the VSM limit. However, as the work in Chapter 4 will show (Figure 4.6), $H_{c2}(12\text{ K})$ is too close to 14 T to be accurately determined with this VSM, and thus no H_{c2} measurements were made on these samples.

Since H^* is defined as the field where $J_c = 0$, H^* is often determined by linear extrapolation of J_c (or F_p) to zero when plotted versus applied field. For A15 materials however, the highly non-linear form of such curves makes accurate extrapolation difficult. Kramer [21] developed a flux pinning model based upon flux line lattice shear that is applicable to Nb_3Sn superconductors. From the model, a plot of $J_c^{1/2}\text{B}^{1/4}$ vs. B will be linear, and the extrapolation to zero then defines H^* . The Kramer formulism is used to determine H^* in this thesis and is termed H^*_{Kramer} to distinguish it from other methods. As mentioned in Chapter 1, Kramer extrapolations have historically been incorrectly used to determine H_{c2} , but it has been shown that extrapolations of J_c or F_p to be representative of H^* , not H_{c2} , in highly optimized Nb–Ti [2].

The magnetization of a superconductor as a function of applied magnetic field is hysteretic (Figure 3.2) and the width of the hysteretic magnetization loop is proportional to J_c [65]. Since, for H^*_{Kramer} determination, we only care about the extrapolation of $J_c^{1/2}\text{B}^{1/4}$ and $J_c \propto \Delta m$, one can simply extrapolate $\Delta m^{1/2}\text{B}^{1/4}$ versus B to zero. This was the method used in this thesis to determine H^*_{Kramer} .

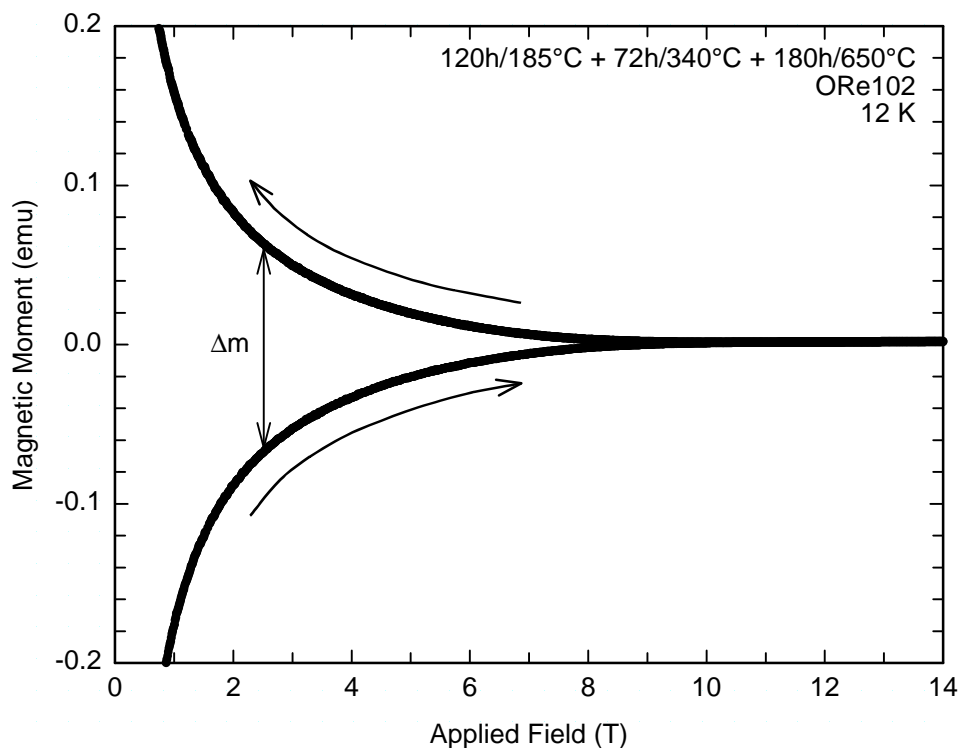


Figure 3.2. 12 K VSM curve for ORe102 after a full manufacturer's heat treatment. The bottom and top arrows indicate the data taken during increasing and decreasing magnetic field sweep, respectively. The loop width (Δm) is proportional to J_c .

To determine the relative changes in J_c values, the sample moment at 4.2 K & 12 T and at 12 K & 5 T was normalized to the much more readily measurable sample mass (i.e. $\Delta m/\text{mass}$), rather than to sample volume. For samples from a given wire, it was assumed that the sample mass would be proportional to the A15 volume, as every sample received the same A15 reaction heat treatment. That is, the average A15 cross-sectional area in each sample was assumed to be the same when given the same A15 reaction heat treatment. While this allows for comparison between samples from the same wire, it does not allow for comparison between different wires.

Each ~5 mm long VSM sample was mounted on a PEEK (poly-ether-ether-ketone) sample holder and secured with teflon tape. PEEK is a thermoplastic that has a small magnetization and good mechanical robustness, which is required for VSM use. The sample was mounted with its axis perpendicular to the applied field and the field was swept at 0.6 T/min from 0 T to 14 T and back. The typical electric field induced in the 5 mm VSM samples was thus $\sim 5 \times 10^{-5}$ V/m.

3.3 Results

3.3.1 SQUID – T_c

Figure 3.3 shows the T_c data normalized to 10 K (just above the Nb transition). T_c values varied only slightly and no systematic trend was observed as a function of ramp rate (and thus of the Cu–Sn microstructure). The T_c values of ORe102 were consistently ~0.4 K higher than those of CRe1912 for the controlled ramp rate heat treatments shown in Figure 3.3a. The ~1 K wide transitions had mid-point T_c values that averaged ~15.8 K and ~16.2 K for CRe1912 and ORe102, respectively. Figure 3.3b compares the extremes in Cu–Sn mixing by plotting the T_c data of ORe102 after a full manufacturer’s heat treatment of 120h/185°C + 72h/340°C + 180h/650°C with the data obtained after directly inserting the samples into a 650°C furnace followed by 180h/650°C. The T_c was only ~0.2 K lower after the full heat treatment than after direct insertion.

A problem with the SQUID measurements is that, upon warming, the temperature would overshoot the set-point by up to 0.3 K and then settle to the set-point temperature. This would set up a situation where the samples were slightly field-cooled, making the

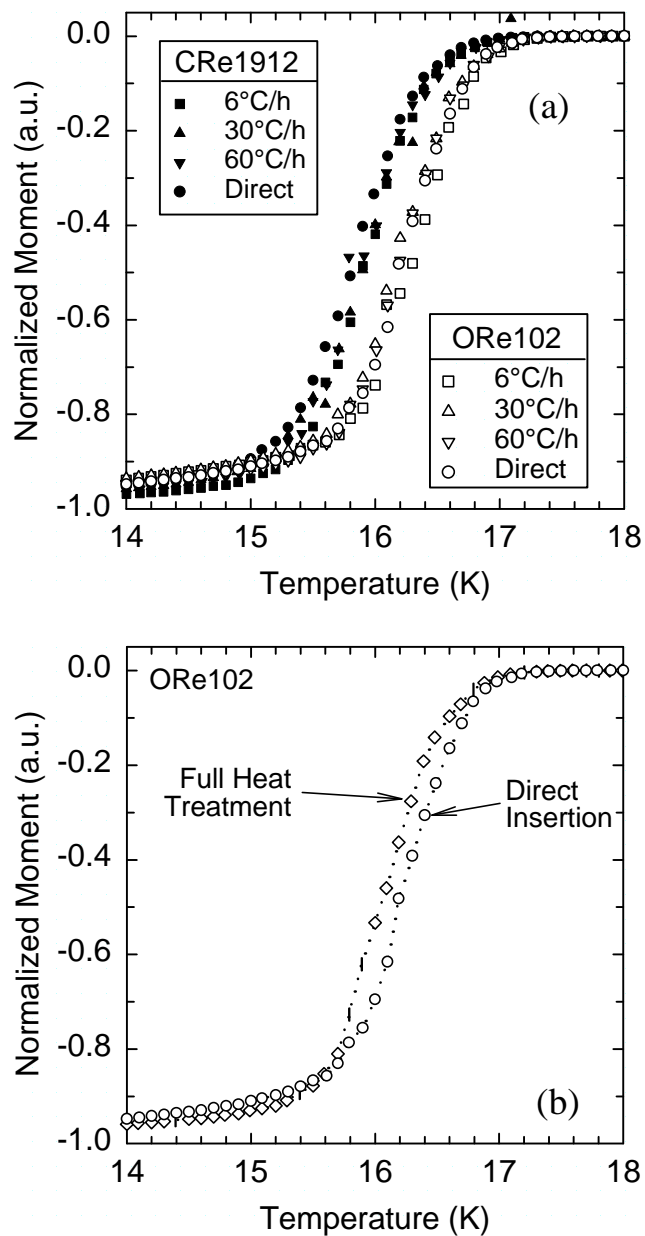


Figure 3.3. T_c of ORe102 (open symbols) and CRe1912 (closed symbols) for various heat treatments. In (a), the samples were ramped to 650°C at various ramp rates or inserted directly into a pre-heated furnace, and then held for 180 hours at 650°C. No trend was seen in T_c as a function of ramp rate. A comparison of a standard manufacturer’s HT (“Full HT”) to one in which the sample was inserted directly at 650°C (“Direct”) is shown in (b). There was only a ~ 0.2 K T_c difference between the two heat treatments.

TABLE 3.3
 H^*_{KRAMER} AND $\Delta m/MASS$ OF CRE1912

Heat Treatment	H^*_{Kramer} (T)		$\Delta m/mass$ (emu/mg)	
	4.2 K	12 K	4.2 K, 12 T	12 K, 5 T
120h/185°C + 72h/340°C + 180h/650°C	24.3	10.0	5.88×10^{-3}	2.58×10^{-3}
6°C/h, RT to 180h/650°C	24.1	10.0	5.39×10^{-3}	2.28×10^{-3}
30°C/h, RT to 180h/650°C	24.2	9.9	5.34×10^{-3}	2.18×10^{-3}
60°C/h, RT to 180h/650°C	24.3	9.9	5.07×10^{-3}	2.08×10^{-3}
Direct insertion, RT to 180h/650°C	24.1	9.9	5.74×10^{-3}	2.35×10^{-3}

measured moment artificially high, and thus the T_c curves slightly low. It is estimated that this caused the measured T_c to be ~ 0.1 K lower than the true T_c because, upon re-cooling, the sample would regain some of its zero-field cooled moment. However, the error from run-to-run is less than 0.1 K and thus relative T_c comparisons are still completely valid.

3.3.2 VSM - H^*_{Kramer} and $Dm/mass$

H^*_{Kramer} and $\Delta m/mass$ values for CRe1912 and ORe102 are listed in Tables 3.3 and 3.4, respectively. There are only small variations from sample to sample and no clear trend in either parameter as a function of heat treatment. H^*_{Kramer} values were $H^*_{Kramer}(4.2 \text{ K}) \sim 24 \text{ T}$ and $H^*_{Kramer}(12 \text{ K}) \sim 10 \text{ T}$ for both wires. $H^*_{Kramer}(4.2 \text{ K})$ values of CRe1912 were

TABLE 3.4
 H^*_{KRAMER} AND $\Delta m/MASS$ OF ORE102

Heat Treatment	H^*_{Kramer} (T)		$\Delta m/mass$ (emu/mg)	
	4.2 K	12 K	4.2 K, 12 T	12 K, 5 T
120h/185°C + 72h/340°C + 180h/650°C	23.4	10.0	4.81×10^{-3}	2.11×10^{-3}
6°C/h, RT to 180h/650°C	24.0	10.2	5.78×10^{-3}	2.74×10^{-3}
30°C/h, RT to 180h/650°C	23.7	10.0	5.68×10^{-3}	2.53×10^{-3}
60°C/h, RT to 180h/650°C	23.7	10.1	6.02×10^{-3}	2.68×10^{-3}
Direct insertion, RT to 180h/650°C	23.8	10.1	4.78×10^{-3}	2.12×10^{-3}

generally only slightly higher than those of ORe102, but was 0.9 T higher for CRe1912 than for ORe102 after the full manufacturer's heat treatment.

Figures 3.4a and 3.4b show examples of Kramer plots at 12 K and 4.2 K, respectively. All of the 12 K and 4.2 K Kramer plots demonstrated subtle non-linearities and it is believed that these are indicative of A15 phase inhomogeneity. At 12 K, the extrapolation was made more difficult due to the curvature at low and high field. Therefore, the extrapolation was generally made between 4 T and 8 T, where the data was most linear. The measurement error in $H^*_{Kramer}(12\text{ K})$ was estimated to be 0.1 T. At 4.2 K, there is a slight downward bend in the moment above ~10 T, which is not believed to be due to systematic error, but is indicative of the true sample response at high field (> 14 T). Therefore, the data above 10 T was used to determine $H^*_{Kramer}(4.2\text{ K})$. A linear extrapolation of the data between 0 T and 10 T gives $H^*_{Kramer}(4.2\text{ K})$ values that are ~1 T higher than those reported in Tables 3.3 and 3.4. The error in $H^*_{Kramer}(4.2\text{ K})$ data can not be accurately determined because of the long extrapolation from 14 T to ~24 T. However, these extrapolations are expected to be conservative underestimates, if in error. They are expected to be small, however, the trend (or lack thereof) is supported by the 12 K data, which extend all the way to H^*_{Kramer} .

$\Delta m/\text{mass}$ values for both wires taken at 12 K & 5 T and at 4.2 K & 12 T were much more variable than the H^*_{Kramer} data, but also show no clear dependence on heat treatment. The loop width (Δm) was determined by first-order fit to the Δm data extending ± 0.1 T about the field of interest (Figure 3.5). For both wires, the $\Delta m/\text{mass}$ values were most similar when

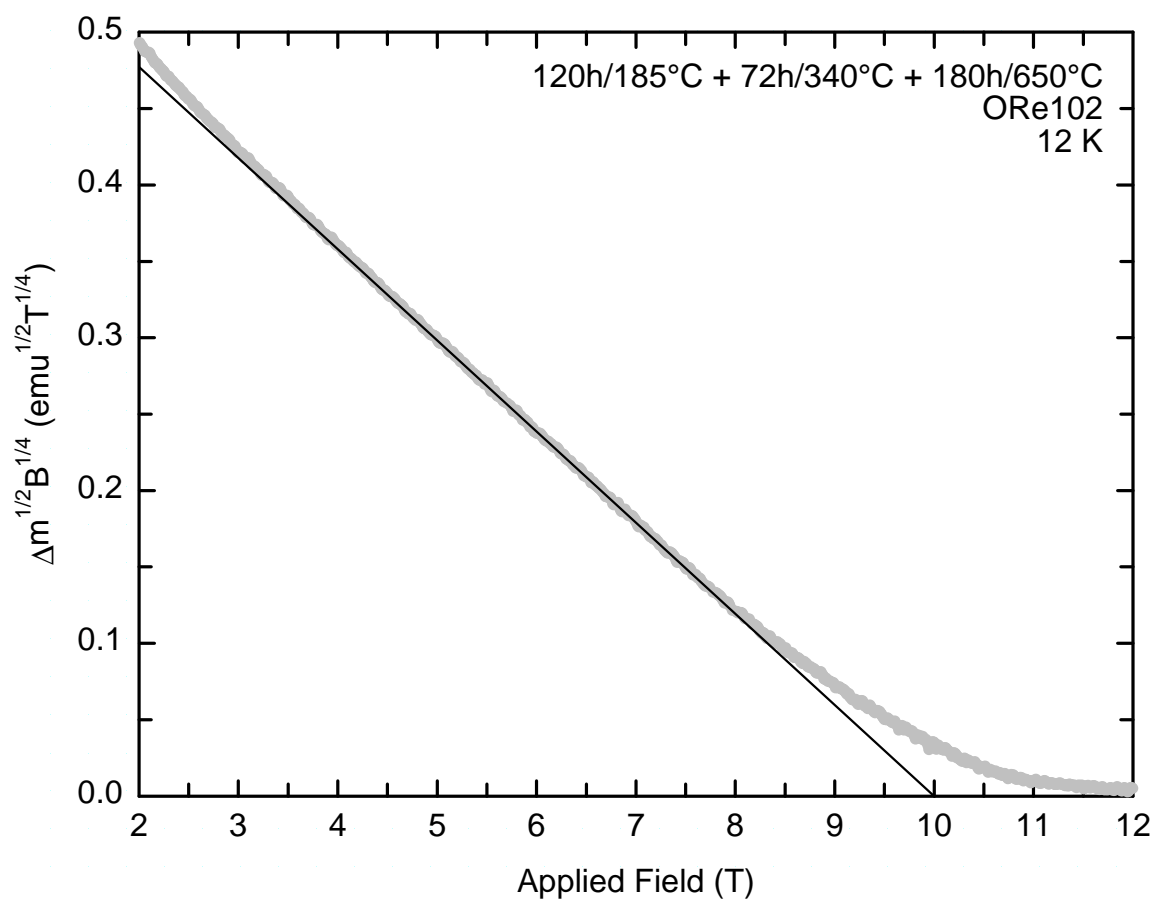


Figure 3.4a. H^*_{Kramer} extrapolations at 12 K and 4.2 K for ORe102 after receiving a heat treatment of 120h/185°C + 72h/340°C + 180h/650°C. The 12 K linear extrapolation was fitted to the data between 4 T and 8 T, generally the most linear portion of the data.

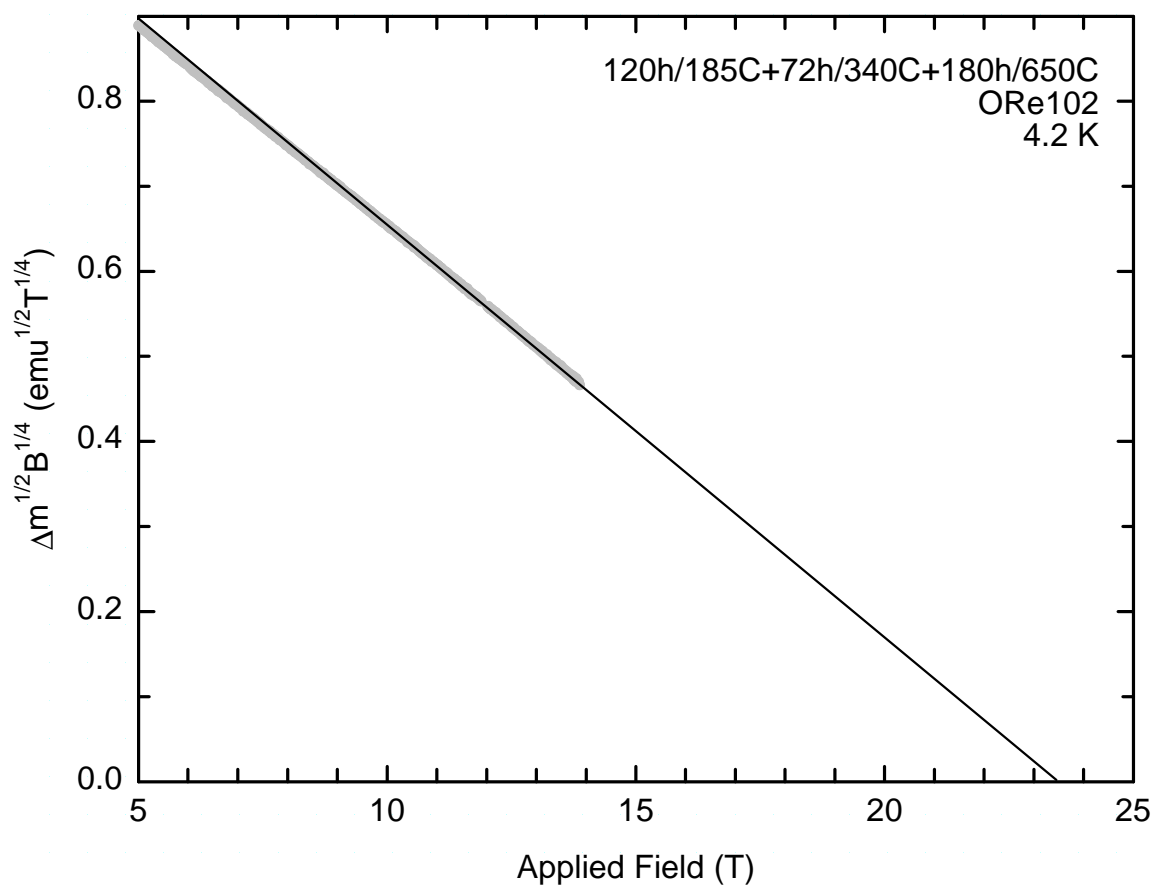


Figure 3.4b. Kramer extrapolation of ORe102 at 4.2 K. The decrease in slope at fields greater than ~10 T is believed to be reflective of the high field (> 14 T) data, and thus it was used for the linear extrapolation. The long extrapolation distance made accurate determination of $H^*_{Kramer}(4.2K)$ more difficult.

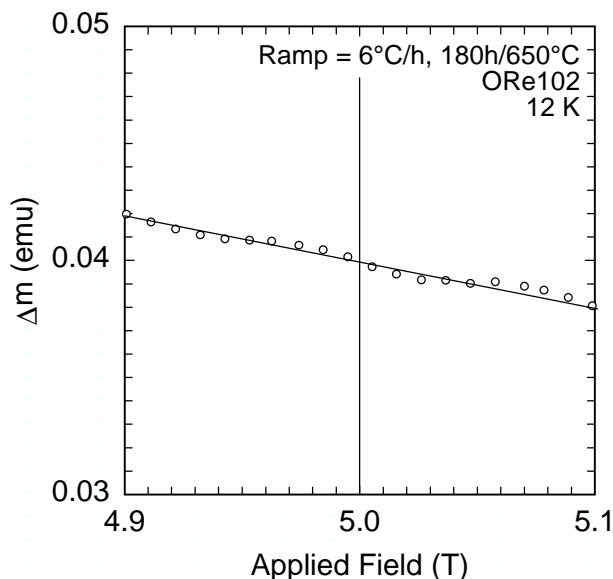


Figure 3.5. Δm versus applied field for ORe102 that received a 6°C/h ramp from room temperature to 650°C, where it underwent a 180h/650°C heat treatment. Due to fluctuations in the data, Δm at the field in question (here, 5 T) was determined by a linear fit. The cause of oscillatory nature of the data is not known.

considering only Cu–Sn mixing at the heat treatment extremes (i.e. full heat treatment and direct insertion). However, $\Delta m/\text{mass}$ values of the controlled ramp rate heat treatments (6°C/h, 30°C/h and 60°C/h) were much more variable.

3.4 Discussion

There is no evidence that the Cu–Sn microstructural state (as generated by a wide range of Cu–Sn mixing heat treatments) influences the inductively measured superconducting properties in fully reacted low-Cu, internal-Sn wires. This is true whether the mixing heat treatment lasts 200 hours or just a few minutes (i.e. direct insertion). While there were variations in all of the measured parameters, no systematic trend was found. For both CRe1912 and ORe102, H^*_{Kramer} at 12 K and 4.2 K was essentially independent of

Cu–Sn mixing heat treatment. The T_c values for a given wire were also quite consistent, varying by only ~ 0.2 K for all heat treatments examined. $\Delta m/\text{mass}$ exhibited the most variability of the measured parameters. This may be due to an incorrect assumption that the volume of A15 generated within a given wire type (e.g. CRe1912) is the same with the same A15 reaction heat treatment. It is unclear whether the cause of the $\Delta m/\text{mass}$ variation is due to variations in A15 volume or composition and T_c spread of the A15. It is not believed, however, that these effects are heat treatment related because the closest two $\Delta m/\text{mass}$ values for CRe1912 and ORe102 are those at the heat treatment extremes (manufacturer's heat treatment versus direct insertion). Moreover, $\Delta m/\text{mass}$ trends are not consistent in either CRe1912 or ORe102. $\Delta m/\text{mass}$ at the heat treatment extremes for CRe1912 are higher than for all other heat treatments, while those of ORe102 are lower than for all other heat treatments. It is thus concluded that the Cu–Sn mixing heat treatment does not play a role in the superconducting properties for a wide range of mixing heat treatments.

This independence of the superconducting properties from the Cu–Sn mixing step(s) is quite unlike that in high-Cu composites (e.g. CRe1712 of Chapter 2), where the aggressiveness of the Cu–Sn mixing heat treatment influences the Cu–Sn phase diffusion front movement, and thereby the amount of filament coupling [46] and hysteretic coupling losses. Filament coupling is not an issue for low-Cu wires like CRe1912 and ORe102 because the filaments are initially so close together that it is not possible to keep them from coupling during heat treatment. Filament coupling is caused by the 36% volume expansion upon conversion from Nb to Nb₃Sn and due to the formation of the Cu–Nb–Sn ternary between filaments, which transform into Nb–Sn A15 at reaction temperatures.

The very limited literature on the influence of Cu–Sn mixing gives mixed results as to its importance. Dietderich et al. [54] reported that transport J_c is at most 15% lower when there is no Cu–Sn mixing heat treatment prior to a 700°C A15 reaction step, as compared to having a full Cu–Sn mixing heat treatment (120h/200°C + 24h/380°C + 233h/580°C). Verwaerde et al. [19] found that the best J_c values were generated with a heat treatment schedule that had only a mid-level heat treatment (at ~350°C) prior to the A15 reaction heat treatment. They also found, however, that having no Cu–Sn mixing step generated J_c values that were only slightly below the best values. Verwaerde et al. also show that a full Cu–Sn mixing heat treatment schedule generated the worst J_c , the opposite to what Dietderich et al. reported. More recently Barzi et al. found that removal of the Cu–Sn mixing steps below 575°C did not reduce J_c . However, all heat treatments in the Barzi et al. study had a heat treatment hold of 200h/575°C, which would produce significant Cu–Sn mixing and also produce Nb–Sn A15 phase. Since the Sn concentration of the first A15 to form would be most affected by Cu–Sn inhomogeneity, having a first heat treatment hold at 575°C is effectively the same as not having any Cu–Sn mixing heat treatment at all. Both Dietderich et al. and Verwaerde et al. show that a ~200°C Cu–Sn mixing step is inconsequential for the final superconducting properties.

In contrast to the literature just discussed, where most evaluations were by 4.2 K transport methods, all of the superconducting values in this thesis were generated from magnetization measurements. If the good A15 areas (high Sn concentration, small grains) are on the exterior and are more than a penetration depth (λ) thick, the interior of inductively measured samples are shielded and any interior ‘bad’ areas will not be probed. Chapter 2

showed that when high Sn content Cu–Sn phases (β , γ , ϵ , η) are in contact with Nb, the Nb will dissolve into a Cu–Nb–Sn ternary. Since such Cu–Nb–Sn areas are interior to each bundle, these areas might not be probed by the SQUID T_c measurements. VSM magnetization measurements will see its influence in the magnetic moment. It should be noted, however, that the Cu–Nb–Sn phase was not stable above $\sim 428^\circ\text{C}$ and no Cu–Nb–Sn phases have been seen in fully reacted wires. Thus, it is believed that any Cu–Nb–Sn phase converts to A15 in fully reacted samples. The effect of having dissolved Nb filaments would be to lower transport J_c by decreasing the continuous A15 cross-sectional area.

The T_c values are significantly lower than expected, considering the relatively high $J_{c,non-Cu}$ (12 T) values of these composites ($\sim 2200 \text{ A/mm}^2$). The mid-point transitions were $\sim 16.2 \text{ K}$ and $\sim 15.8 \text{ K}$ for ORe102 and CRe1912, respectively, which is $\sim 2 \text{ K}$ lower than that of stoichiometric, strain-free Nb_3Sn (18.3 K). One possible source of the reduced superconducting properties is compressive strain induced by the higher thermal contraction of Cu relative to that of Nb_3Sn . Thus, the wires are put under compression when cooling from heat treatment temperature to room temperature and also from room temperature down to cryogenic temperatures (termed “pre-compression”). The magnitude of this effect was examined in the 0.5 mm diameter CRe1912 sample from Chapter 2 that underwent a heat treatment of 150h/340°C + 180h/650°C. To relieve the pre-compression, it was etched for ~ 4 hours in a 1:1 solution of $\text{H}_2\text{O}:\text{HNO}_3$ to remove the Cu and/or Cu alloys, leaving behind strain-free, individual bundles. It was found that the T_c was indeed $\sim 0.6 \text{ K}$ higher in the strain-free, etched state (Figure 3.6), pointing to a pre-compression effect. (The effect of strain on CRe1912 at 0.7 mm diameter was not tested, but it is assumed that the results would

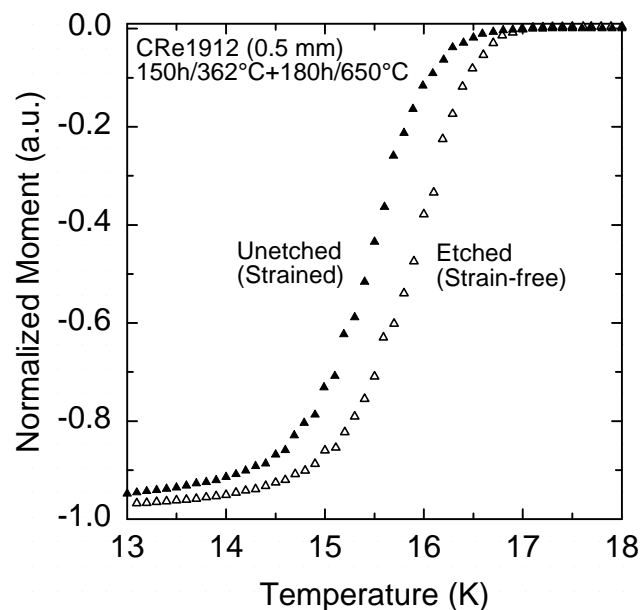


Figure 3.6. T_c of CRe1912 (0.5 mm) in the unetched and etched states showing the effect of pre-compression. The T_c was ~ 0.6 K higher in the strain-free state, showing that while pre-compression does play a role in suppression of the superconducting properties, it is not a large enough effect to account for the ~ 2.5 K suppression in T_c below that of stoichiometric Nb_3Sn .

be similar). However, the T_c values of CRe1912 are ~ 2.5 K below that of stoichiometric Nb_3Sn . Therefore, T_c suppression can not be solely due to strain and must be primarily due to a sub-stoichiometric A15 composition effect. Consistent with this view, the T_c values of CRe1912 are (~ 0.4 K) lower than those of ORe102, and CRe1912 has a higher Nb:Sn ratio in the bundle.

The true Nb:Sn ratios of each composite are undefined to the extent that it is not possible to predict a priori the extent of Nb conversion to Nb-Sn A15 phase prior to reaction. Thus, the *effective* Nb:Sn ratios lie somewhere between the extremes listed in Table 3.2. It is expected that all of the filaments will fully react for a standard heat treatment schedule, and the Nb:Sn ratio excluding the barrier should thus be taken as the lower bound in Nb content. However, it is never the case that the entire Nb barrier reacts to form Nb_3Sn . Therefore, the

Nb:Sn ratios that include the barrier are unrealistically high in Nb, but are nevertheless easily measured and give a qualitative upper bound in Nb.

From the atomic Nb:Sn ratios in Table 3.2, it appears that CRe1912 and ORe102 were designed such that, if the A15 phase to form is stoichiometric, $\sim 1/2$ of the Nb barrier will be reacted. By limiting the size of the Sn core, one can try to ensure that the Sn supply will be depleted before the barrier reacts completely through. It has only recently been seen, in preliminary experiments on mixed Nb and Sn powders, that the first Nb–Sn A15 to form is close to stoichiometry [66]. However, if unreacted Nb is present (e.g. unreacted Nb barrier) and there is not an adequate Sn supply, the A15 reaction continues and there is a risk that the average A15 composition will become more sub-stoichiometric.

In practice, the Nb barrier reaction is highly non-uniform and it often locally reacts completely through, allowing Sn to leak into the stabilization Cu. Evidence of significant barrier reaction is seen in an ORe102 SEM-BSE image (Figure 3.7) of the barrier region after direct insertion for 180h/650°C. Areas clearly exist where the barrier has reacted completely through and A15 grains are present on the *outside* of the Nb barriers, indicating Sn in the stabilization Cu. The low T_c values reported here are probably a combination of an over-reacted barrier and Sn loss into the stabilization Cu, both making the effective Nb:Sn ratio Sn-poor.

A sensitive test of impurities is to measure the resistivity ratio between room temperature (ρ_{RT}) and just above T_c (ρ_{T_c}), called the residual resistivity ratio (RRR = ρ_{RT}/ρ_{T_c}). A quicker, but slightly less sensitive, 77 K test was conducted to check for the existence of Sn in the stabilization Cu. The resistivity ratio (RR₇₇) was measured between

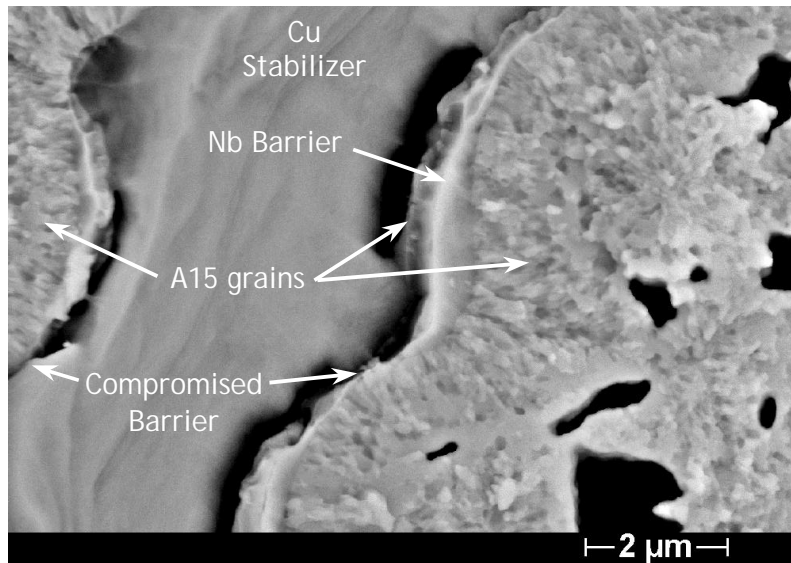


Figure 3.7. Backscatter SEM image of ORe102 after direct insertion for 180h/650°C. The image shows the region between 2 bundles, and areas can be seen where the Nb–Sn A15 phase has grown completely through the barrier. As a result of subsequent Sn leakage into the Cu stabilizer, A15 grains can be seen growing on the external side of the Nb barrier (Image courtesy of Dr. Peter Lee).

room temperature and 77 K ($RR_{77} = \rho_{RT}/\rho_{77\text{ K}}$). For the ORe102 sample directly inserted for 180h/650°C, it was found that $RR_{77} = 3.1$, as compared to 6.8 in the as received, unreacted state, further indicating Sn in the stabilization Cu. This is consistent with the RRR work of Barzi et al. [41] on other internal-Sn samples. In that work, the RRR values in heat treated internal-Sn wires were ~ 10 to 20, although high purity matrix has $RRR > 100$.

3.5 Summary

In fully reacted, low Cu, internal-Sn Nb_3Sn wire, there is no effect on the inductively measured T_c , H^*_{Kramer} , or J_c due to differences in the Cu–Sn microstructure prior to the A15 reaction heat treatment. This is true whether the Cu–Sn mixing heat treatment lasts ~ 200 hours or just a few minutes. Despite their high J_c values, the T_c values of the wires examined in this chapter are ~ 2 K below that of stoichiometric Nb_3Sn . The primary cause of this T_c

suppression is attributed to Sn-poor A15 phase due to an excess of Nb in the bundles and Sn leakage out of the filament bundles and into the stabilization Cu. Sn leakage occurs because the Nb barrier reacts non-uniformly and in some places will react completely through, leading to significant sub-stoichiometry in the A15 layer. The influence of the Cu–Sn mixing heat treatment on Nb filament coupling is not important in low-Cu wires, as all of the filaments couple regardless of heat treatment schedule. Clearly, there presently exists a tradeoff between the cross-sectional area of the A15 layer and the A15 Sn concentration. If low-Cu, internal-Sn wires are to reach their full potential, the issues of the proper Nb:Sn ratio and Sn leakage into the stabilizing Cu must be addressed.

CHAPTER 4 – INTERPLAY BETWEEN T_C , H^*_{KRAMER} , H_{C2} AND COMPOSITE DESIGN

Chapter 3 showed that the superconducting properties are essentially independent of how, or even whether, the Cu and Sn are mixed prior to A15 reaction. This leaves the A15 reaction heat treatment and specific features of the Cu–Nb–Sn bundle design as primary factors influencing the superconducting properties. This chapter pursues a global investigation of the superconducting properties of internal-Sn composite wires of different Cu:Nb:Sn ratios and their dependence on heat treatment. More specifically, T_C , H^*_{Kramer} and H_{c2} were measured by SQUID and VSM magnetometry for 5 different internal-Sn wire designs and many different A15 reaction heat treatments.

4.1 Wire Characteristics

Five different internal-Sn wire designs were examined. CRe1912 (0.7 mm) and ORe102 (0.8 mm) have been described in Chapter 3. They received the widest array of A15 formation heat treatments of any of the wires discussed. ORe110 (1.0 and 0.7 mm diameter), ORe137 (1.0 mm) and ORe139 (1.0 mm) were manufactured by OI-ST and received only

TABLE 4.1
ORE110, ORE137 AND ORE139 COMPARISON

Wire	Diameter	# of Bundles	Core	Filaments	Barrier
CRe1912	0.7 mm	54	Sn-9at.%Mg	Nb-2at.%Ti	Nb
ORe102	0.8 mm	54	Sn-1.3at.%Cu	Nb-2at.%Ti	Nb
ORe110	0.7 & 1.0 mm	40	Sn-1.3at.%Cu	Nb-2at.%Ti	Nb
ORe137	1.0 mm	54	Sn-9at.%Mg	Nb-2at.%Ti	Nb
ORe139	1.0 mm	54	Sn-1.3at.%Cu	Nb-2at.%Ti	Nb

one heat treatment each. ORe110, ORe137 and ORe139 are shown in Figure 4.1 and characteristics for all of the wires are listed in Tables 4.1 and 4.2. As in previous chapters, the Cu:Nb:Sn ratios were determined by digital SEM-BSE image analysis of a symmetric bundle from the inner-most ring of bundles within each wire (e.g. those shown in Figure 4.1).

Each wire is subtly different from the others. ORe110 has 40 bundles while CRe1912, ORe102, ORe137 and ORe139 each have 54. The Sn core of ORe110 looks different than the other wires in Figure 4.1 because it suffered an unusual Sn pullout during polishing that did not occur in the other samples. ORe137 is optimized to maximize the Nb and Sn areas by minimizing the interfilamentary Cu. It was the most Sn-rich

TABLE 4.2
ATOMIC Cu:Nb:Sn RATIOS PRIOR TO A15 REACTION

Wire	Including Barrier				Not Including Barrier			
	Cu	Nb	Sn	Composition	Cu	Nb	Sn	Composition
CRe1912	1.81	3.53	1.00	Nb-22.1 ^a %Sn	1.81	2.60	1.00	Nb-27.8 ^a %Sn
ORe102	2.13	3.49	1.00	Nb-22.3 ^a %Sn	2.13	2.51	1.00	Nb-28.5 ^a %Sn
ORe110 (0.7 mm)	2.28	3.39	1.00	Nb-22.7 ^a %Sn	2.28	2.40	1.00	Nb-29.4 ^a %Sn
ORe110 (1.0 mm)	2.30	3.28	1.00	Nb-23.4 ^a %Sn	2.30	2.30	1.00	Nb-30.3 ^a %Sn
ORe137	1.17	2.77	1.00	Nb-26.5 ^a %Sn	1.17	2.01	1.00	Nb-33.2 ^a %Sn
ORe139	2.16	3.74	1.00	Nb-21.1 ^a %Sn	2.16	1.97	1.00	Nb-33.7 ^a %Sn

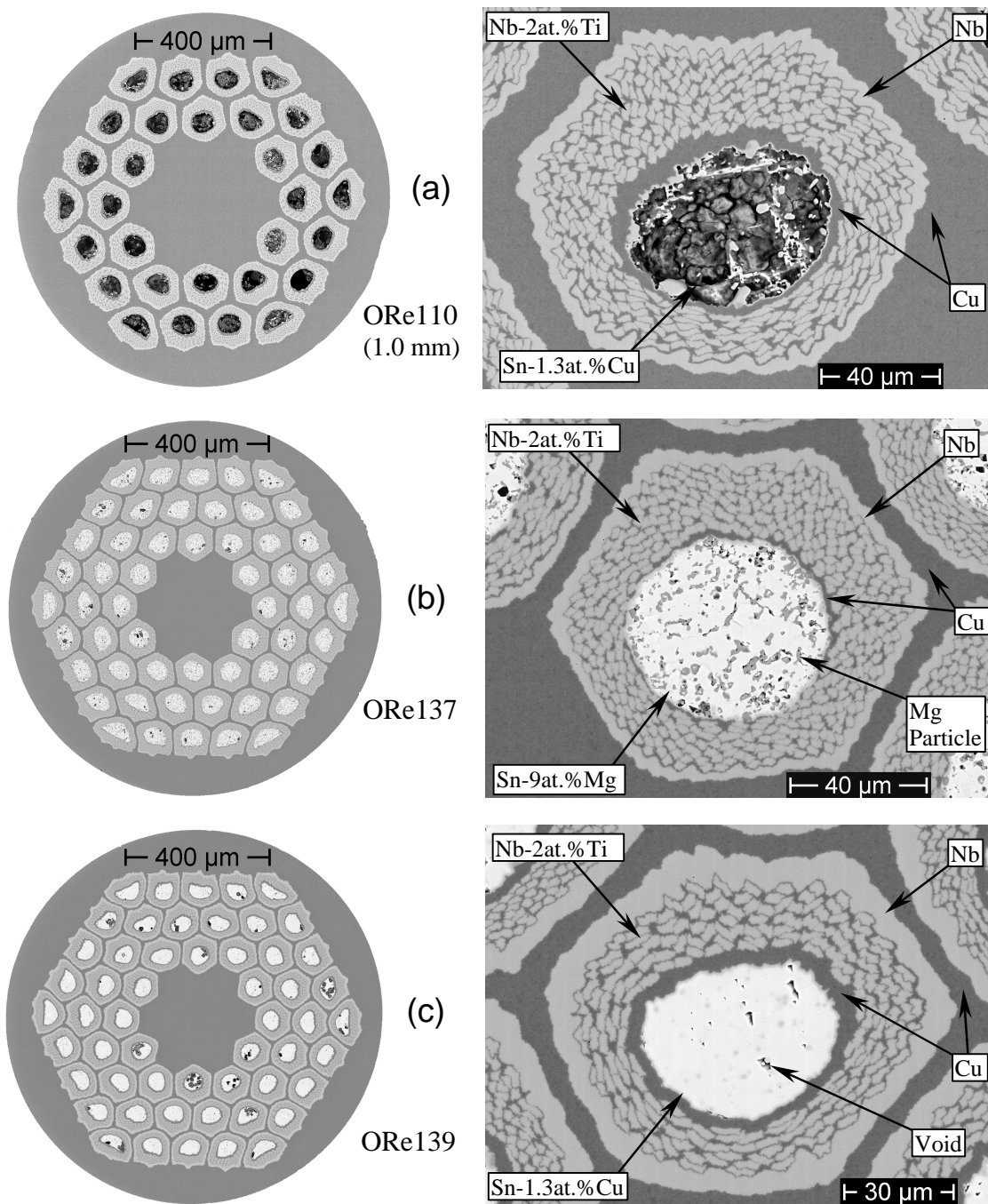


Figure 4.1. SEM-BSE images of wire and bundle cross-sections of (a) ORe110, (b) ORe137 and (c) ORe139, all at 1.0 mm diameter. ORe110 has 40 bundles, while ORe137 and ORe139 have 54. The Sn core in ORe110 and ORe139 is a Sn-Cu alloy, while that of ORe137 is a Sn-Mg alloy. The dark gray regions within the ORe137 core are Mg_2Sn precipitates. ORe110 exhibited an unusual core pullout during polishing. The small black spots within the cores are voids.

of any composite examined. Chapter 3 discussed Nb barrier breakdown and subsequent Sn loss: ORe139 is an attempt to prevent Sn loss by using a $\sim 6 \mu\text{m}$ thick Nb barrier, roughly 50% thicker than the next thickest barrier, that in ORe110. This thick barrier of ORe139 dramatically skews its Cu:Nb:Sn ratio, as will be discussed later in this chapter. All of the wires were manufactured using the MJR method (Figure 1.7) and have Nb barriers, Nb-2at.%Ti filaments and Sn cores alloyed with either Cu or Mg.

Table 4.2 shows that all of the wires have more Sn than necessary to produce stoichiometric Nb_3Sn when excluding the Nb barrier. However, when including the barrier, only ORe137 has an excess of Sn. While the excess Sn in ORe137 will help to maximize the Sn concentration in the Nb–Sn A15, it is imperative that the reaction be stopped in time so that massive barrier react-through does not occur.

4.2 Experimental Procedure

The samples underwent the same preparation procedure as those described in previous chapters. Briefly, the ends of ~ 80 mm long, straight samples were electroplated with Cu, sealed in quartz tubes under ~ 30 mTorr of Ar, and heat treated in a horizontal tube furnace with a 2" bore. The heat treatments are detailed in Table 4.3. Wires undergoing the same heat treatment were sealed in the same quartz tube.

CRe1912 and ORe102 were used to examine the influence of heat treatment time and temperature on the superconducting properties. They first underwent a Cu–Sn mixing heat treatment of 104h/340°C to minimize the risk of liquid Sn-burst. The subsequent A15 formation heat treatments were performed at 650°C, 700°C or 750°C. For each A15 reaction

TABLE 4.3
HEAT TREATMENT SCHEDULES

Wire Designation	Cu–Sn Mixing Heat Treatment	A15 Formation Heat Treatments
CRe1912	104h at 340°C	1, 2, 8, 32, 128, and 256h at 650°C
		1, 2, 8, 32, 64, 128, and 256h at 700°C
		1, 2, 4, 8, 16, 32, 48, and 256h at 750°C
ORE102	104h at 340°C	2, 8, 32, 128, and 256h at 650°C
		1, 2, 8, 32, 64 and 128h at 700°C
		1, 2, 4, 8, 16, 32, 64, and 256h at 750°C
ORe110	110h at 210°C + 48h at 340°C	96h at 695°C
ORe137	48h at 340°C	180h at 675°C
ORe139	48h at 340°C	180h at 675°C

temperature, all of the samples were placed in the furnace together and individual samples were pulled at pre-designated times. As the A15 reaction temperatures increased, the reaction times were shortened to get more data points when the A15 layer was developing most quickly.

ORe110, ORe137 and ORe139 received only the manufacturer’s recommended A15 reaction heat treatments, which differed slightly for different wires. Both ORe137 and ORe139 received an A15 reaction heat treatment of 180h/675°C, while that of ORe110 was 96h/695°C. ORe110 was tested at two wire diameters (1.0 and 0.7 mm) to look for changes in the superconducting properties due to Sn draw-off in the smaller wire. Draw-off is an effect whereby the softer components are reduced in size more quickly than the other components during wire drawing. For the *same* bundle within ORe110, it can be seen from Table 4.2 that the Nb:Sn ratio is 3.46:1.00 (Nb-22.4at.%Sn) at 0.7 mm versus 3.35:1.00 (Nb-23.0at.%Sn) at 1.0 mm. This small difference is consistent with Sn draw-off.

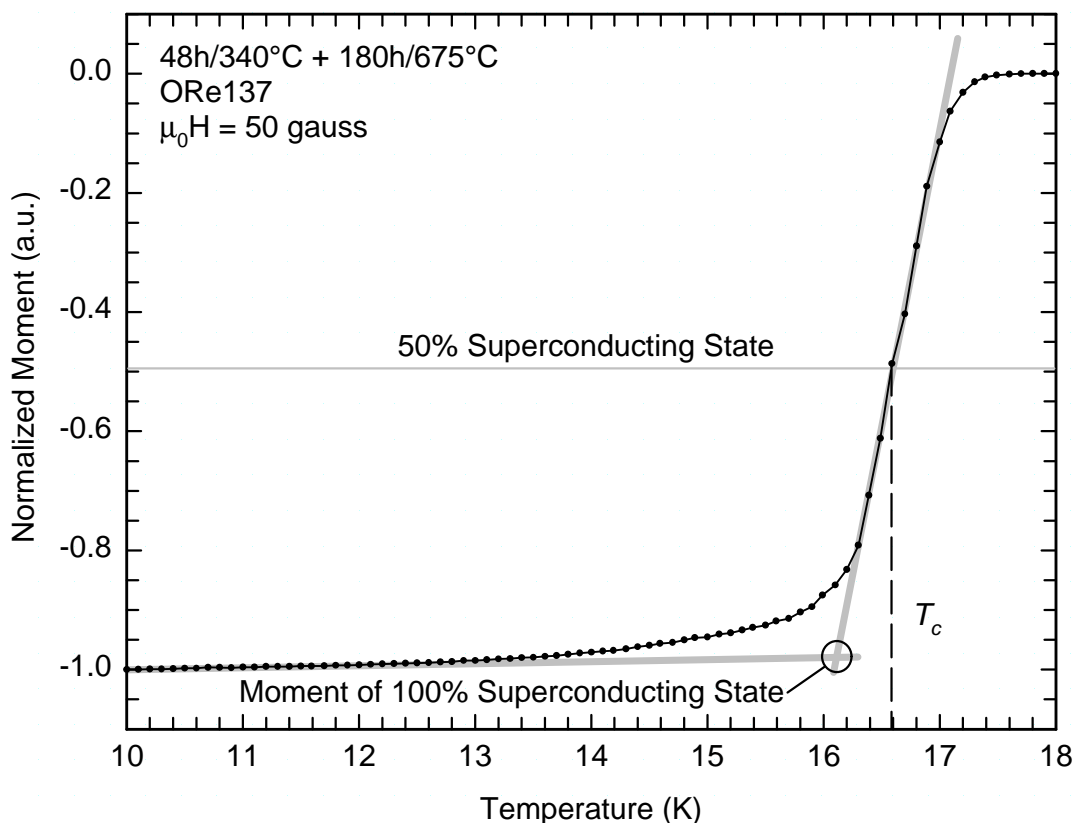


Figure 4.2. T_c curve of ORe137 illustrating how T_c was defined. The magnetic moment of the 100% superconducting state was defined as the intersection of the baseline with a linear extrapolation through the transition. T_c was then defined as the temperature at which the moment was 50% of the full superconducting state moment. The 0% superconducting (100% normal) state is defined as being at $m = 0$ (zero) emu.

T_c and H^*_{Kramer} were measured inductively in the same manner as described in Chapter 3. T_c was measured by SQUID magnetometry, and H^*_{Kramer} and H_{c2} were measured by vibrating sample magnetometry (VSM). The mid-point of the T_c transition was determined as illustrated in Figure 4.2, where the moment has been normalized to the 10 K value (i.e. just above the Nb transition). The moment of the 100% superconducting state was defined as the intersection of the extended baseline and the linear extrapolation of the transition. T_c was then defined as the temperature that generated half of this moment.

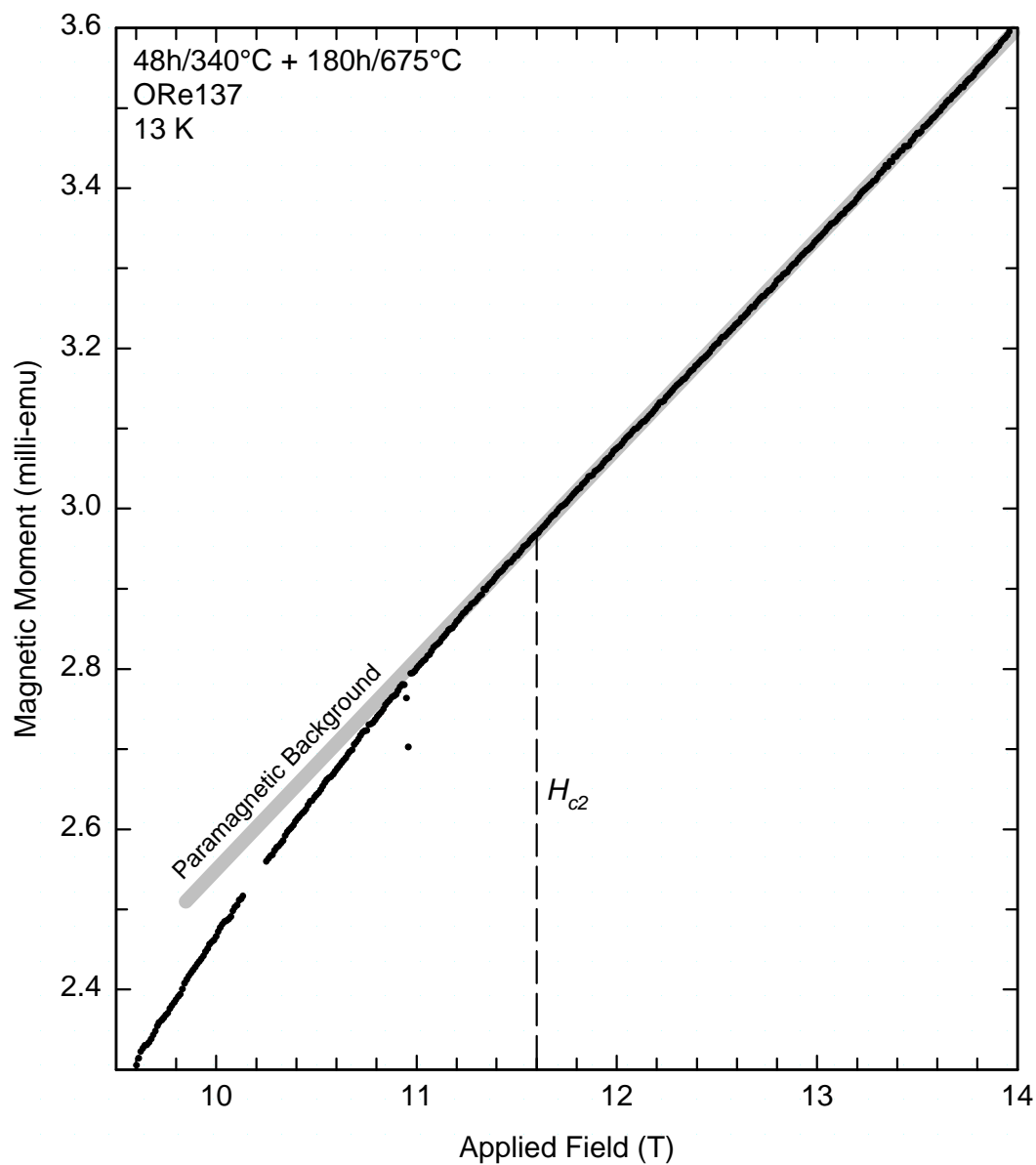


Figure 4.3. High field VSM data showing the method used to determine H_{c2} . H_{c2} was determined as the field at which the superconducting sample moment (black points) becomes indistinguishable from the paramagnetic background moment (gray line).

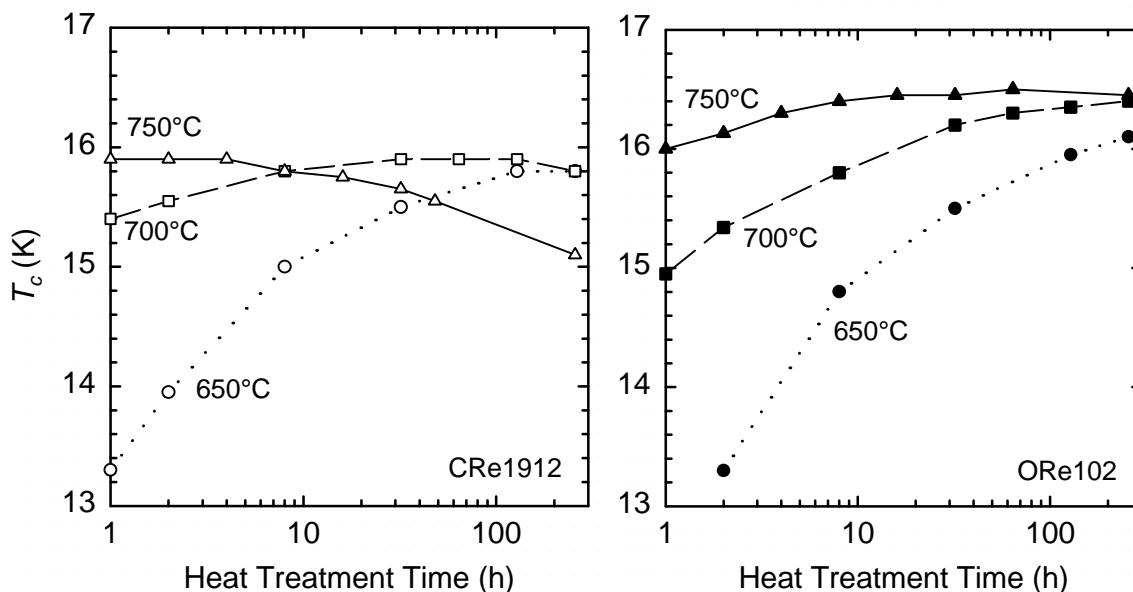


Figure 4.4. T_c as a function of heat treatment time at 650°C, 700°C and 750°C for CRe1912 and ORe102. Maximum T_c values were 15.9 K and 16.4 K for CRe1912 and ORe102, respectively. T_c decreased with 750°C heat treatment time for CRe1912. A similar falloff may have begun at 256h/700°C for CRe1912.

As can be seen in Figure 4.2, the difference between this method and simply taking the T_c value at 0.5 on the normalized y-axis scale was always small, but the latter method is less rigorous. H_{c2} was defined as the field at which superconducting moment becomes indistinguishable from the paramagnetic background moment. Figure 4.3 shows high field VSM data of ORe137 to illustrate how H_{c2} was determined.

4.3 Results

Figure 4.4 shows mid-point T_c values of CRe1912 and ORe102 versus heat treatment time at 650°C, 700°C and 750°C. The maximum T_c values attained by ORe102 and CRe1912 were 16.4 K and 15.9 K, respectively. At 750°C, CRe1912 was at its maximum T_c after only 1 hour and the T_c decreased with increasing heat treatment time beyond 8 hours.

TABLE 4.4
 H^*_{KRAMER} AND T_c VALUES

Wire Designation	A15 Formation Heat Treatment	H^*_{Kramer} (T)		T_c (K)
		4.2 K	12 K	
CRe1912	4h/650°C	20.4	--	14.6
	180h/650°C	24.6	10.1	15.8
	4h/750°C	24.7	10.1	15.9
	256h/750°C	20.3	8.2	15.1
ORe102	4h/650°C	18.8	--	14.2
	180h/650°C	24.0	10.2	16.1
	4h/750°C	24.6	10.3	16.3
	256h/750°C	25.4	10.5	16.4
ORe110, 0.7 mm	96h/695°C	23.8	10.0	16.4
ORe110, 1.0 mm	96h/695°C	24.7	10.7	16.6
ORe137	180h/675°C	25.5	10.8	16.6
ORe139	180h/675°C	25.6	11.0	16.6
PIT	4h/675°C	20.2	7.1	15.3
PIT	8h/675°C	21.9	8.2	15.9
PIT	64h/675°C	25.0	10.7	17.0
PIT	64h/800°C	26.8	11.5	17.3
PIT	8h/850°C	28.1	12.1	17.4

A similar falloff appears to have begun at 256h/700°C for CRe1912. However, for ORe102, no decrease in T_c was seen at any heat treatment temperature.

H^*_{Kramer} was measured for a few of the CRe1912 and ORe102 samples whose T_c values are plotted in Figure 4.4 and for all the ORe110, ORe137 and ORe139 samples. For CRe1912 and ORe102, only those with heat treatments of 4h/650°C, 180h/650°C, 4h/750°C and 256h/750°C were measured to look for a correlation between H^*_{Kramer} and the large variation in T_c . The 12 K and 4.2 K H^*_{Kramer} samples are compiled in Table 4.4 and plotted as a function of T_c in Figure 4.5. There appears to be a very direct correlation between T_c and H^*_{Kramer} . The low T_c samples (especially under-reacted CRe1912 and ORe102 (i.e. 4h/650°C) and over-reacted CRe1912 (256h/750°C)) have the lowest H^*_{Kramer} values.

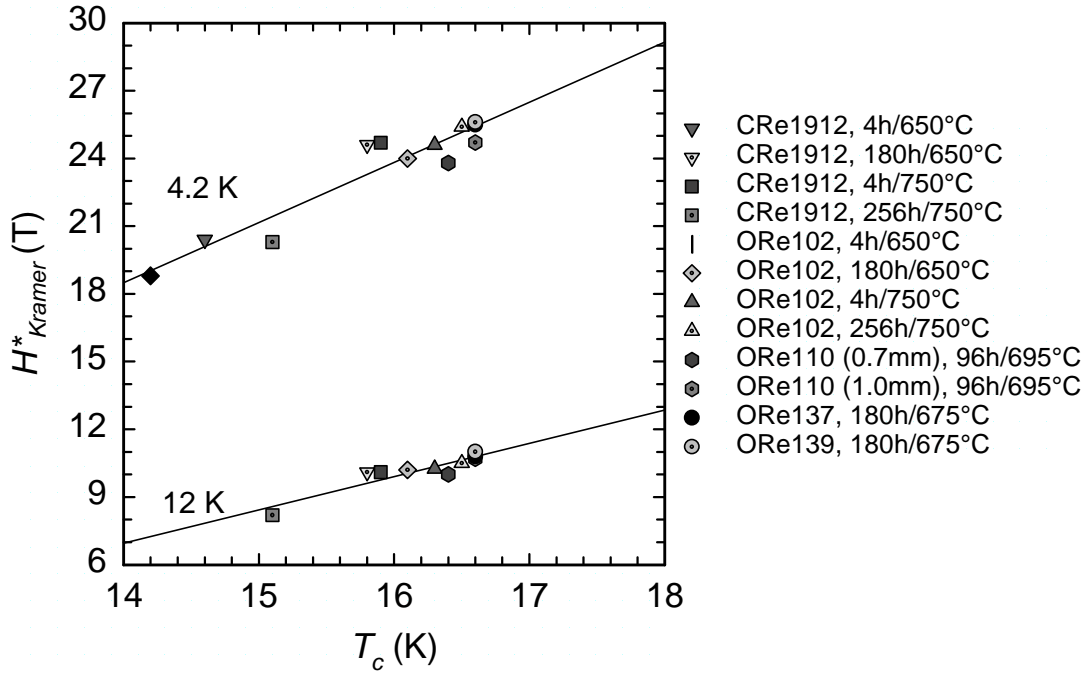


Figure 4.5. H^*_{Kramer} at 12 and 4.2 K as a function of T_c , with a linear fit applied at each temperature.

ORe110 (1.0 mm), ORe137 and ORe139 had the highest T_c values, all reaching 16.6 K, and they also had among the best H^*_{Kramer} values (~ 25.5 T). ORe102 after 256h/750°C has only slightly lower T_c and H^*_{Kramer} values than these 3 “best” samples, despite the very long, high temperature reaction. A first-order fit of the H^*_{Kramer} versus T_c data has the form

$$H^*_{Kramer} (4.2 \text{ K}) = -18.8 + 2.67 \cdot T_c \quad (4.1a)$$

$$H^*_{Kramer} (12 \text{ K}) = -13.7 + 1.48 \cdot T_c . \quad (4.1b)$$

$H_{c2}(T)$ and $H^*_{Kramer}(T)$ are shown in Figure 4.6 for CRe1912 after 256h/750°C and for ORe137 after 180h/675°C. These samples were chosen because, based upon T_c and H^*_{Kramer} , they are the best (ORe137) and worst (over-reacted CRe1912) samples in this

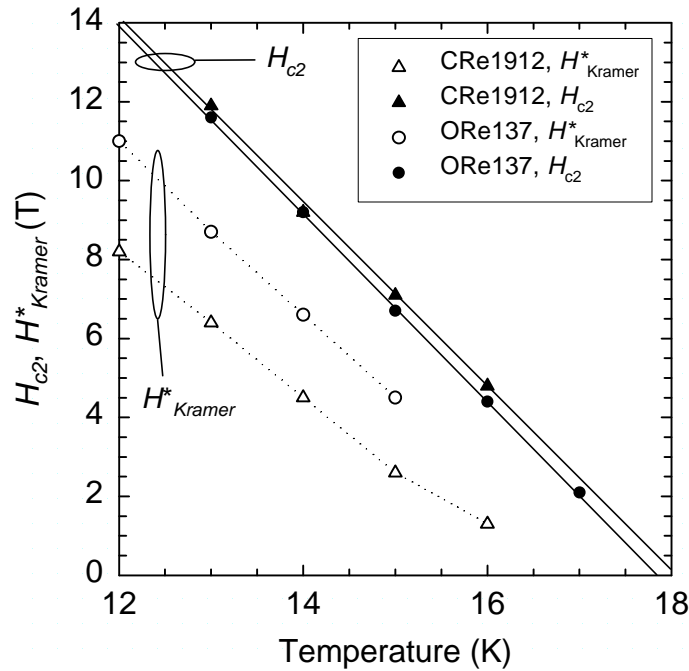


Figure 4.6. H_{c2} and H_{c2}^* as a function of temperature for CRe1912 (256h/750°C) and ORe137 (180h/675°C). H_{c2}^* data is connected by point-to-point lines, whereas the lines through the H_{c2} data are linear fits. The much lower H_{c2}^* of over-reacted CRe1912 than that of ORe137 is indicative of Sn loss through the barrier in CRe1912. However, the H_{c2} values of both samples were nearly identical because only the highest H_{c2} is detected. $dH_{c2}/dT \sim 2.4$ T/K for both samples.

study. H_{c2}^* (T) of CRe1912 was 2 to 3 T below that of ORe137 between 12 K and 15 K.

It is interesting to note, however, that H_{c2} (T) was essentially identical at $dH_{c2}/dT \sim 2.4$ T/K for these two very different samples.

4.4 Discussion

4.4.1 Relationship Between T_c and H_{c2}^*

A new result of this thesis is that there is a direct correlation between T_c and H_{c2}^* . As a check of the universality of the plot in Figure 4.5, results obtained by Fischer [67] on wires fabricated by the Powder-In-Tube (PIT) method (see Figure 1.5) were added. The PIT wire is comprised of a Nb-7.5wt.%Ta alloy tube with a powder core composition that, while

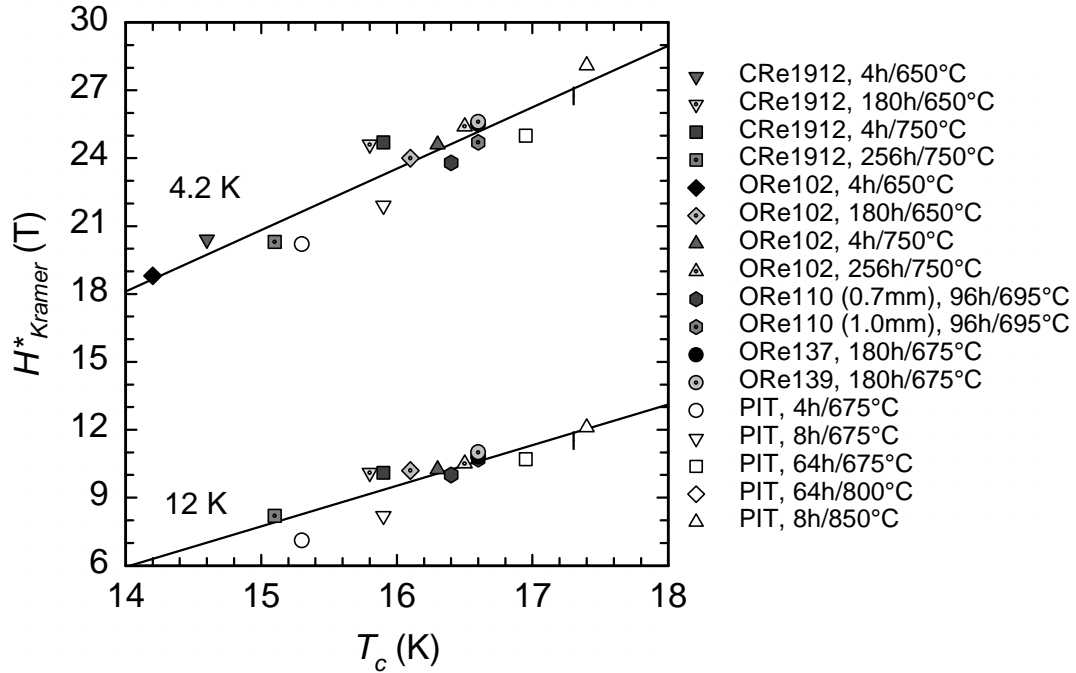


Figure 4.7. H^*_{Kramer} at 12 and 4.2 K versus T_c for internal-Sn and PIT wires (closed and open symbols, respectively). The PIT data fall on a line nicely showing that the linearity holds for Nb_3Sn wire made via other fabrication routes.

proprietary, likely includes $NbSn_2$, Sn, and Cu. The PIT wires and their sample preparation procedures are described in [67]. Data were taken for PIT wires that received heat treatments of 4, 8 and 64 hours at 675°C, 64 hours at 800°C, and 8 hours at 850°C. Figure 4.7 shows T_c versus H^*_{Kramer} including both internal-Sn (closed symbols) and PIT data (open symbols) (the PIT data are tabulated in the bottom rows of Table 4.4). The PIT data is qualitatively in accord with the MJR, internal-Sn data with only small changes to the regression coefficients, thus maintaining the same trend first shown in Figure 4.5.

$$H^*_{Kramer} (4.2 \text{ K}) = -19.8 + 2.71 \cdot T_c(\text{K}) \quad (\text{Tesla}) \quad (4.2a)$$

$$H^*_{Kramer} (12 \text{ K}) = -19.2 + 1.79 \cdot T_c(\text{K}) \quad (\text{Tesla}) \quad (4.2b)$$

As H_{c2} is the maximum limit of H^*_{Kramer} , it is generally assumed that the behavior of H_{c2} as a function of T_c dictates in the T_c dependence of H^*_{Kramer} . Theoretical calculations of H_{c2} in the early literature also show a linear dependence on T_c . Clogston [68], Kim, Hempstead and Strnad [20] and Hake [69] derived the following expressions for $H_{c2}(0)$:

$$\text{Clogston: } H_{c2}(0) = 1.84 \cdot T_c, \quad (\text{Tesla}) \quad (4.3)$$

$$\text{Kim et al.: } H_{c2}(0) = 3.11 \times 10^3 \cdot \rho_n \cdot \gamma \cdot T_c \quad (\text{Tesla}) \quad (4.4)$$

and

$$\text{Hake: } H_{c2}(0) \approx 0.69 \cdot T_c \cdot \left. \frac{dH_{c2}}{dT} \right|_{T_c}, \quad (\text{Tesla}) \quad (4.5)$$

where ρ_n is the normal state resistivity at T_c ($\Omega\cdot\text{m}$), γ is the electronic specific heat coefficient ($\text{J}/\text{m}^3 \cdot \text{K}^2$) and T_c is in Kelvin. Equation 4.3 does not take into account the increase in free energy of the superconductor due to it possessing a finite paramagnetic moment in an applied field, but nevertheless shows a linear T_c dependence. However, equations 4.4 and 4.5 take this into account and are applicable to superconductors whose electron mean free path is much less than the coherence length (i.e. “dirty”), like those in this study.

4.4.2 Relationship between H^*_{Kramer} and H_{c2}

An important observation is that both the best (ORe137) and worst (over-reacted CRe1912) internal-Sn wires have $dH_{c2}/dT \sim 2.4 \text{ T/K}$ (Figure 4.6), in spite of the fact that

their T_c values differ by 1.5 K and their $H^*_{Kramer}(12\text{ K})$ values differ by 2.6 T. Their dH_{c2}/dT values are consistent with the measurements of Orlando et al. [9] and Hechler et al. [15], and with the measurements of PIT wires reported by Fischer [67].

The distinction between H^* and H_{c2} is one that is often ignored. While internal-Sn composites are assumed to be longitudinally uniform, there exist Sn concentration gradients transverse to the wire axis which lead to gradients in T_c , H_{c2} and J_c , due to the non-equilibrium nature of Nb–Sn A15 formation. H^*_{Kramer} is defined by measurement of the highest field of long-range connectivity along the filament axis and, in principle, is $\sim 90\%$ of H_{c2} . However, if long-range compositional uniformity is lacking, dissipation first sets in at locations that can be considered the *weakest links*, and H^*_{Kramer} is a measure of such weak links. Contrarily, H_{c2} is defined by the last remnant of superconducting diamagnetism, that is, the *strongest link*. Figure 4.6 shows that the distinction between H_{c2} and H^* needs to be taken seriously.

It is unlikely that the linearity in $H^*_{Kramer}(T_c)$ holds at high T_c values (i.e. $> 17\text{ K}$). If one assumes that the highest measured H_{c2} is that of a strain-free, stoichiometric Nb_3Sn , then $T_c = 18.3\text{ K}$ and $H_{c2}(0) = 30\text{ T}$ from equation 4.5. This calculated $H_{c2}(0)$ is $\sim 2\text{ T}$ higher than that calculated by Hechler [15] for unalloyed Nb_3Sn and $\sim 1\text{ T}$ higher than that predicted by Orlando for alloyed Nb_3Sn [9]. An apparent contradiction is that the linear fit to the $H^*_{Kramer}(T_c)$ data (equation 4.2a) implies that, for stoichiometric, strain-free Nb_3Sn (i.e. $T_c = 18.3\text{ K}$), $H^*_{Kramer}(4.2\text{ K}) \sim 30\text{ T}$, which would be higher than $H_{c2}(4.2\text{ K})$. Therefore, one must assume that there is a plateau in $H^*_{Kramer}(T_c)$ at high T_c values that is not accounted for in the fit. This should also correspond to a plateau in H_{c2} as a function of Sn content (and

thus T_c). The H_{c2} behavior as a function of Sn content in alloyed (i.e. “dirty”) Nb_3Sn is not known and needs to be explored. Flükiger, Schauer and Goldacker [13] have shown that there is a steep fall off in H_{c2} above 24.5at%Sn (i.e. at high T_c values) in unalloyed (binary) Nb_3Sn . This fall off is due to a decrease in T_c and γ caused by the cubic-to-tetragonal lattice transition below ~ 43 K [12].

4.4.3 T_c and A15 Chemical Composition

The T_c values of the best internal-Sn and PIT wires are suppressed by ~ 1.5 K and ~ 1 K, respectively, below the 18.3 K T_c of stoichiometric, strain-free Nb_3Sn . In Chapter 3, it was shown that there was a 0.6 K decrease in T_c in an internal-Sn wire due to strain effects caused by the differential contraction between the A15 and Cu. The PIT wire was also checked to see if its superconducting properties suffered similarly. To extract strain-free individual filaments, the PIT wires were etched in HNO_3 using the same method as in Chapter 3 with the internal-Sn wires. Figure 4.8 shows the T_c curves in the strained and unstrained state for both the PIT wire and the internal-Sn wire of Chapter 3. Contrary to the 0.6 K increase in T_c seen for CRe1912, the T_c of the PIT wire was the same in the etched and unetched condition, indicating no pre-compression effect in the PIT wire. Therefore, it may be that strain is the primary factor for the lower T_c values of the best internal-Sn wires (e.g. ORe137) relative to PIT conductors in Figure 4.7. If the pre-compression effect is the same in the best internal-Sn wires (e.g. ORe110, ORe137, ORe139) as it was in CRe1912, relief of the pre-compression would increase their T_c by ~ 0.6 K, making their T_c values comparable to those of PIT wires (i.e. ~ 17 K). This implies that the A15 phase generated in the best

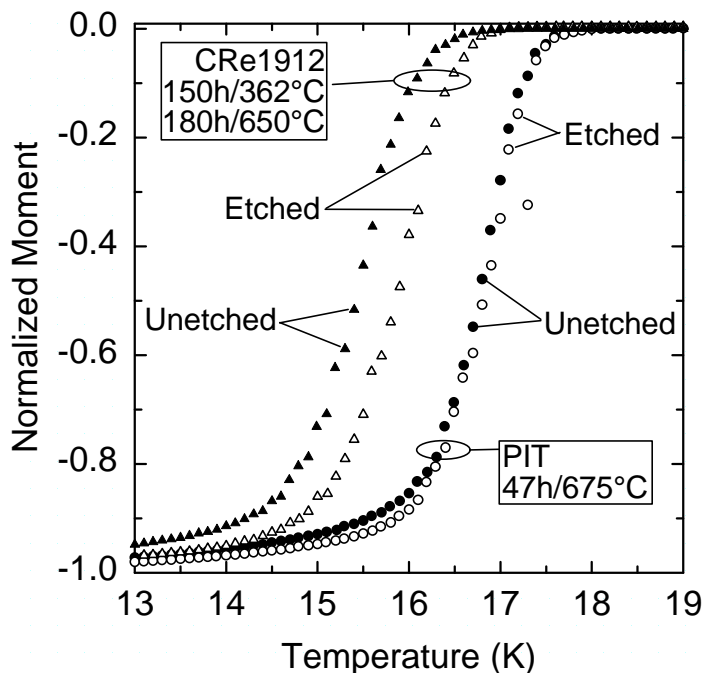


Figure 4.8. Inductive T_c curves for 0.5 mm CRe1912 (triangles) and a PIT wire (circles) in unetched (strained) and etched (strain-free) states. There is a T_c increase of ~ 0.6 K for CRe1912, whereas there was no change in T_c in the PIT wire. T_c strain suppression of internal-Sn wires is likely the primary factor that they fail to achieve PIT performance levels (see Figure 4.7).

internal-Sn wires and in PIT wires is of roughly the same quality. The lack of pre-compression effects in PIT indicates that their low T_c values (i.e. < 18 K) must also be due to some effect besides strain, possibly sub-stoichiometry.

Energy Dispersive Spectroscopy (EDS) measurements on the A15 areas in over-reacted samples show only a slight sub-stoichiometry. In CRe1912 after 256h/750°C, the A15 composition ranged between Nb-23.5at.%Sn and Nb-24.5at.%Sn, with variations across the agglomerated filament stack depending on whether the measurement was conducted at the center (lower Sn concentration) or edge (higher Sn concentration) of what was formerly an individual filament. By comparison, the composition of the PIT A15 phase after 64h/800°C was much closer to stoichiometry, ranging between Nb-24.5at.%Sn and

Nb-25at.%Sn. From Flükiger et al. [13], these compositions imply that T_c should be between ~16.4 K and ~17.8 K in CRe1912, and between 17.8 K and 18.0 K in the PIT wire. However, the measured T_c values were 15.1 K and 17.3 K in CRe1912 and the PIT wire, respectively (Table 4.4). Thus, even taking strain effects into consideration, the T_c values are lower than their compositions indicate. T_c is also reduced by atomic disorder [16, 70, 71] and may play a role in the suppressed T_c values seen here, however, this is beyond the scope of this study.

4.4.4 Composite Design Implications

The best evidence of the influence of the Nb:Sn ratio comes from ORe110 measured at 1.0 and 0.7 mm diameters, where the only changing parameters were the Nb:Sn ratio and diffusion distance. The Nb:Sn ratios were 3.28:1.00 and 3.39:1.00 (when including the barrier) at 1.0 and 0.7 mm diameter, respectively, due to draw-off of the soft Sn. While these ratios are not very different from each other, the variation in the superconducting properties is consistent with them. T_c was 0.2 K higher, $H^*_{Kramer}(12\text{ K})$ was 0.7 T higher and $H^*_{Kramer}(4.2\text{ K})$ was 0.9 T higher at 1.0 mm diameter than at 0.7 mm diameter. Strengthening this argument is the fact that the Sn diffusion distances are longer in the 1.0 mm diameter wire, which would tend to hinder A15 layer growth, however the 1.0 mm diameter had the better superconducting properties. This highlights the importance of taking Sn draw-off into consideration in the wire design.

Seemingly contrary to this conclusion is that the T_c and H^*_{Kramer} values of ORe137 and ORe139 appear to be independent of their vastly different Nb:Sn ratios. These two

samples were also the best performing internal-Sn samples, with both having $T_c = 16.6$ K and H^*_{Kramer} values of ~ 10.9 T (at 12 K) and ~ 25.5 T (at 4.2 K). It is logical that ORe137 would have good properties because of its advantageous, excess Sn design (2.77:1.00). However, the good T_c and H^*_{Kramer} values of ORe139 are not easily explained, due to its high Nb:Sn ratio when including the barrier (3.74:1.00). As mentioned earlier, the large Nb:Sn ratio of ORe139 is due to the fact that its Nb barrier is roughly twice as thick as that in ORe137 (~ 6 μm versus ~ 3 μm , respectively). The likely reason for the similar superconducting behavior of these two wires is that the A15 reaction front after 180h/675°C has reached the same distance into the Nb barrier in both composites, and thus the *effective* Nb:Sn ratios are the same in both wires. This is a clear example of how the true Nb:Sn ratio lies between the extremes listed in Table 4.2.

To maximize the superconducting properties, it is essential to effectively contain the Sn in the package. The T_c falloff of CRe1912 during the 750°C heat treatment is illustrative of the superconducting consequences when Sn is not effectively contained within the bundle and is allowed to escape. Figure 3.7 showed that the barrier will react through locally even after a standard heat treatment of 180h/650°C, and evidence of Sn loss comes from A15 grains growing on the external side of a Nb barrier. Further proof of Sn loss comes from the residual resistivity ratio measured at 77 K (ρ_{RT}/ρ_{77K}), which showed that RR was lower after heat treatment.

It is not clear why ORe102 did not exhibit any T_c degradation, even though it has a higher Sn concentration than CRe1912. Moreover, the average minimum Nb barrier thickness (i.e. the shortest path for Sn to escape through the barrier) at any given point was

digitally measured to be nearly identical at 1.96 and 2.14 μm for CRe1912 and ORe102, respectively. One difference that might play a role is that the bundles of CRe1912 are $\sim 25\%$ smaller in area than ORe102 ($\sim 65 \mu\text{m}$ versus $\sim 75 \mu\text{m}$ diameter, respectively, for the symmetric bundles), while the absolute Sn content in CRe1912 is only 1% lower (data not shown). This, coupled with the shorter diffusion distances, gives CRe1912 a higher Sn activity that enhances the driving force for A15 formation and, subsequently, barrier reaction. Also, there is less interfilamentary Cu in CRe1912 than in ORe102, which increases the Sn activity by decreasing the volume of Cu where Sn can reside. The Mg from the Sn core should also enhance A15 formation in CRe1912. Togano, Asano and Tachikawa [30] found that A15 layer formation was faster, the A15 grain sizes were smaller, and T_c and I_c were improved when the matrix Cu was alloyed with 0.5at.%Mg in bronze processed wires, but only for heat treatment temperatures above 750°C . McKinnell, Siddall and O'Larey [32], on the other hand, have shown that internal-Sn wires with Sn(Mg) cores had higher J_c values than similar wires with Sn(Cu) cores at heat treatment temperatures of 650°C . Moreover, McKinnell et al. state that Mg decreases the Sn solubility in the interfilamentary Cu, and thus the Sn activity should be higher still in CRe1912. Perhaps, all these factors put together increase the Sn activity in CRe1912 to the point where the A15 layer grows quicker and barrier react-through occurs much more readily than in ORe102.

4.5 Summary

There is a direct correlation between H^*_{Kramer} and T_c that is valid for both internal-Sn and PIT wires. It is hypothesized that the dependence of H^*_{Kramer} on T_c is mediated by the

dependence of H_{c2} on T_c . $H_{c2}(0)$ was calculated to be ~ 30 T in stoichiometric, strain-free Nb-Sn A15, using $T_c = 18.3$ K and $dH_{c2}/dT|_{T_c} = 2.4$ T/K. Assuming a linear $H^*_{Kramer}(T_c)$ dependence to 18.3 K gives $H^*_{Kramer}(4.2 \text{ K}) = 30$ T for stoichiometric Nb-Sn A15. Therefore, because this would be higher than $H_{c2}(4.2 \text{ K})$, this implies that there must be a plateau in H^*_{Kramer} at high T_c values. T_c values indicate that modern internal-Sn and PIT wires are sub-stoichiometric. Strain has been ruled out as a primary factor in causing the suppressed T_c values, as its effect is smaller than the suppression seen. The Cu:Nb:Sn ratio varies from bundle to bundle, with the outer, highly deformed bundles having a higher Sn content. Moreover, the true (i.e. effective) Nb:Sn ratio in any given bundle is unknown because the amount of Nb that will react is unpredictable. It is critical to contain the Sn within the bundles to promote A15 stoichiometry and maximize superconducting properties. If the barrier reacts completely through, Sn escapes into the stabilization Cu causing the superconducting properties (and RRR) to decline dramatically.

CHAPTER 5 – INFLUENCE OF WIRE DESIGN ON J_c

A significant fraction of the cost of high field magnet systems (e.g. particle accelerators) lies in the conductor. In order to reduce the cost of such large systems, it is advantageous to make a more cost efficient conductor, that is, reduce the cost per kA·m. This can be accomplished through more effective processing techniques and also through increases in J_c . Improvements in J_c come as a result of increases in the fraction of A15 within the conductor (i.e. $J_{c,non-Cu}$) and improvements in the intrinsic J_c of the A15 layer ($J_{c,layer}$). Therefore, this chapter considers component design issues for internal-Sn conductors. Specifically, it discusses design choices that increase the A15 fraction in the package by increasing the Nb and Sn fraction and minimizing the fraction of the diffusion barrier, interfilamentary Cu and alloying element in the Sn core. Rather than the typical ~100 μm diameter package found in commercial wires, this chapter considers a more stringent 50 μm bundle, much closer to the stated 40 μm HEP design goal.

5.1 The Essentials: Nb and Sn

The basic components of an internal-Sn wire are the Nb filaments, diffusion barrier, Sn core and interfilamentary Cu. In order to minimize work hardening during wire drawing (like that found in bronze-route conductors), the components should work harden slowly, and thus be pure or only lightly alloyed. Although commercially impractical because it would require a reaction temperature above 900°C, the maximum A15 fractional area is generated with only Nb and Sn in the package. The optimal amount of Sn is, of course, dictated by the amount of Nb in package that is to be reacted to form the A15 phase (i.e. filaments and barrier). The atomic volume of pure Sn is 27.0 Å³/atom and that of pure Nb is 18.1 Å³/atom. Therefore, to form stoichiometric Nb₃Sn, the Sn must be ¹/₃ and the Nb ²/₃ of the cross-sectional area of the package (27.0 Å³ of Sn for every 3×18.1=54.3 Å³ of Nb).

It is assumed that the A15 transformation occurs entirely within the Nb. The lattice constants for Nb and Nb₃Sn are 3.3063 Å [51] and 5.290 Å [11], respectively. The unit cell of Nb₃Sn contains 6 Nb atoms and 2 Sn atoms, which is therefore 24.67 Å³ per Nb atom. This is 36.3% larger than the 18.07 Å³ per Nb atom of pure, BCC Nb. A 36.3% volume expansion implies that there is a 10.8% expansion along each of the coordinate axes, and thus a 22.9% expansion in cross-section. However, the length of heat treated wires is seen to increase by only ~1% [72], meaning that nearly all of the expansion must occur radially and therefore produces a cross-sectional area expansion of the Nb of ~35% upon conversion to A15. A 35% area expansion of the Nb is assumed throughout this chapter.

There are many ways to account for the area expansion upon conversion to A15. At one extreme, the expansion can be entirely taken up internally to fill void space that was

formerly taken up by the Sn (i.e. constant package outer diameter (OD)). At the other extreme, there can be an outward only expansion that is accounted for solely through an increase in the package OD. This latter possibility represents the worst case scenario, in that it generates the minimum volume fraction of A15. In practice, there is both internal and external expansion. Measurement of the same, symmetrical (i.e. minimally aspected) ORe102 bundle before and after a reaction of 180h/650°C showed a ~4% increase in area after reaction, suggesting that much of the growth is taken up internally by expansion into the former Cu spaces between the filaments (see, for example, the right side of Figure 3.7) and into the former core region. Based on this data, 4% area expansion of the bundle is assumed throughout this chapter. Preliminary results on PIT conductors show an outward area expansion of ~10% [67], perhaps due to the circular geometry of the individual filaments of this conductor design.

For an idealized bundle containing only Nb and Sn, the A15 area will account for 86.7% of the package area after reaction. If the desired $J_{c,non-Cu}(12\text{ T}, 4.2\text{ K}) = 3000\text{ A/mm}^2$, as it is for the High Energy Physics community, then $J_{c,layer}$ must be 3460 A/mm^2 . Pyon and Gregory [73] have reported $J_{c,layer}(4.2\text{ K}, 12\text{ T}) = 4622\text{ A/mm}^2$ in a different style of internal-Sn conductor to those studied in this thesis, but it is unclear whether the I_c was normalized to the A15 area or the area of the pre-reacted Nb filaments. The reported $J_{c,layer}(4.2\text{ K}, 12\text{ T})$ of CRe1912 was 3600 A/mm^2 [74], and this low value was perhaps another consequence of Sn loss through the barrier. For PIT conductors, Field et al. [75] have reported $J_{c,layer}(4.2\text{ K}, 12\text{ T}) = 4500\text{ A/mm}^2$, and $J_{c,layer}(4.2\text{ K}, 12\text{ T}) = 5530\text{ A/mm}^2$ was derived for a different commercially available PIT conductor [67]. Therefore, $J_{c,layer}$ generated in multiple

ways easily exceeds that required to generate $J_{c,non-Cu} = 3000 \text{ A/mm}^2$ in this idealized conductor of only Nb and Sn.

5.2 Diffusion Barrier

Since any useful conductor must contain high conductivity, stabilization Cu, the bundle must have a diffusion barrier, thus diluting $J_{c,non-Cu}$. The area of the bundle is defined by the outer boundary of the diffusion barrier, and decreasing the barrier thickness is one method toward increasing $J_{c,non-Cu}$. However, this carries the risk of being too thin to effectively contain the Sn, especially if the barrier reacts with Sn. The required thickness will depend on the barrier material and the amount of excess Sn after reaction with the filaments. Also, as the bundle shapes are seldom circular, the barrier will also have to be thick enough to withstand the higher degree of reaction in those regions nearest the Sn core. This is particularly important for the highly aspected bundles near the corners of the filament stack. Moreover, the barrier thickness is highly non-uniform at final wire size and thus the barrier will have to be thick enough to withstand local thinning. Conversely, this implies that there will be areas where the barrier is unavoidably thicker than necessary, increasing the amount of unused real estate and decreasing $J_{c,non-Cu}$.

The optimal barrier is one that does not react with Sn, does not dissolve or react with Cu and can support large drawing strains. No material fulfilling all these requirements is known. Ta–56at%Nb is one choice (e.g. CRe1721 from Chapter 2) and, while this alloy does react with Sn, the reaction is very slow. However, Ta–56at%Nb is not a good candidate for most internal-Sn applications because it work hardens quickly and because bonding between

the wire sub-elements is poor, especially when the conductor is entirely cold drawn, like the Modified Jellyroll (MJR) conductors of this thesis.

In conductors where the design goal is to produce the maximum possible amount of Nb–Sn A15 phase within the package, the barrier is invariably pure Nb to allow for its partial transformation into A15. There is a considerable risk in allowing the barrier to react because, as shown in Chapter 3 (Figure 3.7), barrier reaction is highly non-uniform and can react through locally. When this happens, the barrier has failed its primary function – Sn retention. Based upon their Nb:Sn ratio, it appears that the barriers of CRe1912 and ORe102 were designed so that half of the barrier would react. However, the barrier reacted completely through locally in both wires, and resulted in the marked T_c degradation of CRe1912 during the 750°C heat treatment. The shortest path for Sn to escape through the barrier was $\sim 2 \mu\text{m}$ in both CRe1912 and ORe102. As both conductors were designed so the half their volume would react but they both exhibited A15 react-through, this suggests that there needs to be a safety margin of more than $1 \mu\text{m}$ to effectively retain the Sn. The benefit to $J_{c,non-Cu}$ of

TABLE 5.1
COMPOSITE DESIGN RAMIFICATIONS FOR $J_{c,LAYER}$

Nb Barrier (μm)	(vol.%)	Interfilamentary Cu (vol.%)	Core Material	A15 (vol.%)	Required $J_{c,layer}$ (A/mm^2)
0	0	0	Sn	86.7	3460
2	15.4	0	Sn	80.0	3750
3	22.6	0	Sn	76.9	3900
2	15.4	15	Sn	67.0	4480
2	15.4	2.7	Sn	77.7	3860
2	15.4	15	Sn-9at.%Mg	65.1	4610
2	15.4	15	Sn-1.3at.%Cu	66.9	4480
2	15.4	15	Sn-5.9at.%Ti	66.3	4530

Assumptions: 50 μm bundle O.D., stoichiometric Nb_3Sn , 50% of barrier reacts,
desired $J_{c,non-Cu}$ (4.2 K, 12 T)= 3000 A/mm^2

increasing the A15 fraction in the package by allowing a significant fraction of the barrier to react needs to be assessed to determine if it outweighs the penalties of allowing Sn to escape into the stabilization Cu.

The pure Nb barriers of the wires in this thesis (except ORe139) account for 15 ± 0.5 vol.% of the bundle prior to reaction. For a 50 μm diameter bundle, this represents only a 2 μm thick barrier. Assuming the filaments and 50% of a 2 μm barrier converts to stoichiometric A15, the fraction of A15 in the package will be 80.0 % and thus the required $J_{c,layer} = 3750 \text{ A/mm}^2$ to reach $J_{c,non-Cu} = 3000 \text{ A/mm}^2$ (Table 5.1), some 11% higher than without any barrier. But as noted above, a 2 μm Nb barrier typically does not effectively contain the Sn. Increasing the barrier thickness to 3 μm (50% reacted), leads to a $J_{c,layer}$ requirement of 3900 A/mm^2 , only a 4% $J_{c,layer}$ increase over the 2 μm barrier case.

To maximize the A15 fraction, one must minimize unreacted portion of a Nb barrier. However, the practical minimum is 1 to 2 μm due to concern over excessive Sn loss into the stabilization Cu. Modern high J_c conductors are already at this lower limit in barrier thickness. A small increase in the designed Nb barrier thickness (e.g. 3 μm for 50 μm bundle) would decrease Sn loss and thus help to keep the A15 Sn concentration high, without strongly increasing the $J_{c,layer}$ requirements. However, to understand the minimum required $J_{c,layer}$, the rest of this analysis assumes a 50 μm OD bundle with a 2 μm Nb barrier in which 50% reacts to form the Nb–Sn A15 phase.

5.3 Interfilamentary Cu

The interfilamentary Cu must (1) permit A15 formation at $\sim 700^\circ\text{C}$ [39], (2) permit composite fabrication (its melting point is between those of Nb and Sn, and it has an easily workable FCC lattice structure), and (3) act as a path for Sn to get to Nb. Reduction in the amount of interfilamentary Cu may represent the best avenue to increasing the $J_{c,non-Cu}$. However, the minimum amount of Cu required in order for the A15 reaction to proceed at temperatures below 700°C is not clearly known. LeFranc and Müller [39] have shown that A15 formation can occur at 450°C with a Cu concentration of only 5 at.% (i.e. 71.2at.%Nb-23.8at%Sn-5at.%Cu). However, the lower limit of Cu fraction may be dictated more by fabricability issues of the MJR design than with the minimum necessary for low temperature A15 reaction. ORe137 has the lowest amount of interfilamentary Cu (14.6vol.%) of any known internal-Sn wire, showing that it is possible to fabricate at this level.

Assuming 15 vol.% of Cu within a $50\ \mu\text{m}$ OD package, the A15 layer accounts for 67.0 % of the post-reaction bundle area, leading to a $J_{c,layer}$ requirement of $4480\ \text{A}/\text{mm}^2$. This $J_{c,layer}$ is 19% larger than that without Cu. For every 1 vol.% reduction in interfilamentary Cu there is $\sim 1.2\%$ decrease in the necessary $J_{c,layer}$ to produce $J_{c,non-Cu} = 3000\ \text{A}/\text{mm}^2$ (or, a $\sim 1.2\%$ increase in $J_{c,non-Cu}$ assuming a constant $J_{c,layer}$). A package with just 5at.% Cu would correspond to 2.7 vol.% Cu in the package and the required $J_{c,layer}$ would only be $3860\ \text{A}/\text{mm}^2$.

5.4 Alloyed Sn Core

Unlike the rest of the component materials, it is highly desirable to harden the Sn core by alloying because the softness of pure Sn makes wire drawing difficult. Alloying also allows for beneficial elemental additions, such as Mg or Ti. Mg has been reported to enhance A15 layer growth rate and minimize A15 grain size [30], and it was subsequently used in CRe1912, ORe110 and ORe137. Ti is starting to replace Mg and Cu as the alloying element in the Sn core because of the increasingly limited supply of inexpensive Nb–2at.%Ti alloy for the filaments, and because the H_{c2} benefits of Ti (and Ta) are deemed to outweigh the benefits of Mg by the superconductor community.

Alloying of the Sn core increases the size of the core and thereby reduces $J_{c,non-Cu}$. The three alloys considered here are Sn–9at.%Mg, Sn–1.3at.%Cu and Sn–5.9at.%Ti. The Sn(Mg) and Sn(Cu) alloys are produced via a eutectoid reaction, and the Sn(Ti) alloy is a mixture of pure Sn with 4.5vol.% Ti_3Sn . Assuming Sn does not remain bound to the alloying element, alloying with Mg, Cu or Ti requires an increase in the area of the core by 9.1%, 0.3% or 3.5%, respectively, over a pure Sn core to have the same amount of Sn atoms. (These calculations are given in Appendix A.) Therefore, Mg addition to the core lowers $J_{c,non-Cu}$ the most, followed by Ti and then Cu. The advantage of using a Sn(Cu) core is apparent, as alloying with Cu has negligible influence on the core size due to the small amount of second phase (Cu–Sn η -phase). However, Cu in the core does not benefit the superconducting properties, like Ti and Mg. For a constant interfilamentary Cu fraction and bundle size, the amount of Nb must be reduced to accommodate the larger alloyed core.

However, the reduction in Nb will in turn reduce the required size of the core slightly. Assuming a 50 μm bundle with 15vol.%Cu and 2 μm barrier in which 50% reacts, a core alloyed with Mg, Cu or Ti will cause the required $J_{c,layer}$ values to be 4610, 4480 or 4530 A/mm^2 , respectively.

5.5 Analysis of a Recent Attempt at an Optimized Package

ORe137 represents the best presently known attempt at implementing an optimal package. It has a Sn-9at.%Mg core to enhance Sn diffusion to the filaments, and the filaments are alloyed with 2at.% Ti to increase H_{c2} . As already mentioned, this conductor maximizes the A15 volume fraction within the bundle by minimizing the interfilamentary Cu (14.6 vol.%) and the unreacted portion of the Nb barriers. It has reached $J_c(4.2 \text{ K}, 12 \text{ T}) = 2900 \text{ A}/\text{mm}^2$. However, the very low Cu fraction within the bundle makes dissolution of the filament stank through the formation of the deleterious Cu–Nb–Sn phase more likely, thus requiring a special, proprietary heat treatment to control its growth.

Small design adjustments of ORe137 should lead to $J_{c,non-Cu}$ in excess of 3000 A/mm^2 . There is a significant Sn excess when including the entire barrier, such that Nb:Sn = 2.77:1.00 (Nb–26.5at.%Sn). This ratio represents a Sn core that is ~5% larger in volume than is needed to fully react all of the Nb and Nb(Ti) in the package and forming stoichiometric Nb₃Sn. If the core were reduced in volume by 5%, this would allow for a ~3% increase in amount of Nb in the package and, subsequently, a 3% increase in the amount of A15 and in the $J_{c,non-Cu}$ to 2990 A/mm^2 .

Another method to increase $J_{c,non-Cu}$ is through a reduction of the interfilamentary Cu. As discussed in the section on interfilamentary Cu, a 1 vol.% reduction in Cu (relative to the package) leads to an ~1.2% increase in $J_{c,non-Cu}$, assuming a constant $J_{c,layer}$. For ORe137, this means that decreasing the volume of interfilamentary Cu by 20% (so that it comprises 11.6 vol.% of the package), and subsequently increasing the volume of Nb and core by 2.1 vol.% and 6.1 vol.%, respectively, should generate $J_{c,non-Cu} > 3000 \text{ A/mm}^2$, exceeding the HEP target. The preceding calculations are predicated on $J_{c,layer}$ being unchanged with changes in the amount of Sn and interfilamentary Cu.

5.6 Summary

The best internal-Sn design is one that permits reliable fabrication and minimizes the volume fraction of elements that are not incorporated into the Nb–Sn A15 phase. This will maximize the A15 fraction after reaction and decrease the necessary $J_{c,layer}$ to attain $J_{c,non-Cu}(4.2 \text{ K}, 12 \text{ T}) = 3000 \text{ A/mm}^2$. Therefore, it is advantageous to minimize the volume of unreacted Nb barrier, interfilamentary Cu and alloying element(s) in the Sn core. However, minimizing the barrier subsequently puts one at risk for Sn leakage into the stabilization Cu, thus decreasing the Sn concentration in the A15 phase and depressing T_c , H^*_{Kramer} and J_c . The barriers in the high J_c conductors of Chapter 5 (other than ORe139) accounted for ~15% of the package cross-section. Minimization of the interfilamentary Cu is deemed the best route toward increasing the A15 fractional cross-section. ORe137 had the lowest vol.% of interfilamentary Cu at 14.6%, but 2.7vol.% Cu is enough to allow for the Nb–Sn A15 reaction to proceed below 700°C. Assuming that only stoichiometric Nb₃Sn

forms, calculations of an idealized conductor (with no barrier, interfilamentary Cu or alloying elements) show that 86.7% is the maximum fractional area of A15 possible. To reach $J_{c,non-Cu} = 3000 \text{ A/mm}^2$, such a conductor would need a $J_{c,layer}(4.2 \text{ K}, 12 \text{ T}) > 3460 \text{ A/mm}^2$. In a more realistic calculation that takes into account the barrier, interfilamentary Cu and alloyed Sn(Mg) core, $J_{c,layer}(4.2 \text{ K}, 12 \text{ T})$ must be $> 4610 \text{ A/mm}^2$, which is in line with reported $J_{c,layer}$ values for internal-Sn conductors (4622 A/mm^2), and is below the best $J_{c,layer}$ derived for PIT conductors (5530 A/mm^2).

Analysis of the most optimized MJR, internal-Sn known to date (ORe137) shows that it has an excess of Sn, even when the barrier fully reacts ($\text{Nb:Sn} = 2.77:1.00$). Replacing some of the Sn with Nb, such that there is only enough Nb and Sn to form stoichiometric Nb_3Sn , would increase $J_{c,non-Cu}$ to 2990 A/mm^2 . Calculations on interfilamentary Cu also showed that it is possible to exceed $J_{c,non-Cu} = 3000 \text{ A/mm}^2$ by simply reducing the volume of interfilamentary Cu by 20% (3 vol.% relative to the package). A factor not accounted for in this chapter is the role of the effective Nb:Sn ratio. Our assumption has been that we supply enough Sn so that only stoichiometric A15 forms, although we know this is never true. These tradeoffs strongly effect T_c , H^* and H_{c2} , and thus J_c , and they remain for further study beyond this thesis.

CHAPTER 6 – SUMMARY

The heat treatment, superconducting properties and wire composition of several commercially available MJR, internal-Sn conductors have been studied. The heat treatment of internal-Sn conductors has two primary functions: (1) mix the interfilamentary Cu with the nearly pure Sn from the core, and (2) react the Sn with the Nb filaments to form the superconducting Nb–Sn A15 phase. The Cu–Sn microstructures were examined in CRe1912 and CRe1721 after heat treatments consisting of 10 different temperatures (up to 600°C) and lasting for 24 and 150 hours. No heat treatment generated a homogenous (i.e. single phase) Cu–Sn microstructure. It was thus concluded that complete mixing of the Cu and Sn is highly unlikely in commercial wires. During this study, the first reported Cu-Sn-Nb ternary was discovered. The ternary was single phase below 401°C, but multiphase at higher temperatures. The composition of the single phase region was Cu-22at.%Nb-61at.%Sn. This ternary phase was seen only when the higher Sn concentration phases (i.e. non- α phases) were in contact with Nb. The Cu–Nb–Sn ternary forms as a result of Nb dissolution and forms disconnected nodules in the core, which have a deleterious effect on transport J_c .

Based upon the available Cu-Nb-Sn phase diagram, there was concern that Cu-Sn phase inhomogeneity might have an effect on the composition of the initial Nb-Sn A15 phase to form and thus effect the superconducting properties. Various Cu-Sn microstructures were generated in CRe1912 and ORe102 by ramping from room temperature to 650°C at ramp rates of 6°C/h, 30°C/h or 60°C/h, and direct insertion into a pre-heated furnace. The superconducting properties of these samples were compared with samples that received a more standard Cu-Sn mixing heat treatment of 120h/185°C + 72h/340°C. No evidence was found that the Cu-Sn mixing step influences the inductively measured T_c , H^*_{Kramer} or J_c (as determined from $\Delta m/mass$) in fully reacted wire. H^*_{Kramer} at 12 K and 4.2 K were ~10 T and ~24 T, respectively, for both wires, independent of heat treatment. The T_c values for all heat treatments were ~15.8 K and ~16.2 K for CRe1912 and ORe102, respectively. These values are ~2 K below that of stoichiometric Nb₃Sn (18.3 K). The T_c suppression due to strain caused by thermal contraction differences between Cu and Nb-Sn A15 (pre-compression) was measured to be ~0.6 K. Therefore, the low T_c values were attributed to sub-stoichiometry caused by excess Nb in the bundles, Sn leakage through the barrier and Sn concentration gradient in the A15 layer. ORe102 T_c values were consistently higher than those of CRe1912, even though they have similar Nb:Sn ratios. It was hypothesized that subtle differences between the two wires raised the Sn activity of CRe1912 enough to cause the barrier to locally react completely through earlier in the heat treatment, thus allowing more Sn to escape then package than in ORe102.

A linear correlation was found between T_c and H^*_{Kramer} in several commercial internal-Sn wires (CRe1912, ORe102, ORe110, ORe137 and ORe139) that underwent a wide

range of A15 formation heat treatments. This linear correlation appears to be universal, as it was also true for Nb₃Sn made via the PIT process. It is hypothesized that the T_c dependence of H^*_{Kramer} is mediated by its dependence on H_{c2} , which itself has a linear dependence on T_c . However, it is also believed that there must be a plateau in H^*_{Kramer} at high T_c values (> 17.0 K), otherwise H^*_{Kramer} would exceed H_{c2} for stoichiometric A15. $H_{c2}(0)$ of stoichiometric, strain-free Nb₃Sn was determined to be ~ 30 T from $dH_{c2}/dT = 2.4$ T/K measurements, which was independent of sample, fabrication route (internal-Sn or PIT) and heat treatment. However, strong differences were found in $H^*_{Kramer}(T)$ for different wires and heat treatments. Therefore, this indicates that the weakest A15 regions are probed by H^* measurements and the strongest are probed by H_{c2} measurements. The T_c of CRe1912 was seen to decrease strongly with increasing heat treatment time at 750°C, and also decrease slightly for long heat treatment time at 700°C. This highlights the effect (though to a greater degree) of having significant barrier reaction and subsequent Sn loss into the stabilization Cu.

Lastly, the effects of varying the package components (barrier, Cu, Sn core alloy) on J_c were calculated. Conductors containing only Nb and Sn, and assuming 100% conversion from Nb to stoichiometric Nb₃Sn, generate the maximum possible A15 fraction in the package of 86.7vol.%. This requires a $J_{c,layer} = 3460$ A/mm² in order to reach $J_{c,non-Cu} = 3000$ A/mm², the unofficial goal of the High Energy Physics (HEP) community. However, in a more realistic model with interfilamentary Cu, a diffusion barrier and alloying element in the core, it was found that $J_{c,layer}$ must be > 4611 A/mm² to reach $J_{c,non-Cu} = 3000$ A/mm². This is in line with the highest measured $J_{c,layer}$ (4622 A/mm²) for internal-Sn composites, but well below the calculated $J_{c,layer} = 5530$ A/mm² for a PIT conductor, the highest $J_{c,layer}$ yet for

Nb–Sn A15 phase. Analysis of the most optimized MJR, internal-Sn conductor to date shows that it has a nearly stoichiometric Nb:Sn ratio when including the barrier (2.95:1.00). Although, there is little room for improvement in the Nb:Sn ratio, it was calculated that only a 3 vol.% reduction of the interfilamentary Cu, and subsequent replacement with Nb and Sn, can increase $J_{c,non-Cu}$ from 2900 A/mm² to 3000 A/mm², meeting the HEP goal.

REFERENCES

- [1] R.M. Scanlan, *IEEE Trans. Appl. Supercond.*, **11** (1), 2150 (2001).
- [2] M.T. Naus, P.J. Lee, A.A. Squitieri, D.C. Larbalestier, *IEEE Trans. Appl. Supercond.* **7** (2), 1122 (1997).
- [3] P.J. Lee, C.M. Fischer, D.C. Larbalestier, M.T. Naus, A.A. Squitieri, W.L. Starch, R.J. Werner, P.J. Limon, G.J. Sabbi, A. Zlobin and E. Gregory, *IEEE Trans Appl. Supercond.*, **9** (2), 1571 (1999).
- [4] M. Suenaga, D.O. Welch, R.L. Sabatini, O.F. Kammerer and S. Okuda, *J. Appl. Phys.*, **59** (3), 840 (1986).
- [5] R.L. Cooper, *RCA Rev.*, **25**, 405 (1964).
- [6] H. Hillman and K.J. Best, *IEEE Trans. Mag.*, **MAG-13** (5), 1568 (1977).
- [7] P.H. Bellin, V. Sadagopan and H.D. Gatos, *J. Appl. Phys.*, **40** (10), 3982 (1969).
- [8] Personal communication, Jeffrey A. Parell, Oxford Instruments - Superconducting Technology, Inc. (2002)
- [9] T.P. Orlando, E.J. McNiff Jr., S. Foner and M.R. Beasley, *Phys. Rev. B*, **19** (9), 4545 (1979).
- [10] C.P. Charlesworth, I. Macphail and P.E. Madsen, *J. Mat. Sci.*, **5**, 580 (1970).
- [11] H. Devantay, J.L. Jorda, M. Decroux, J. Muller and R. Flükiger, *J. Mat. Sci.*, **16**, 2145 (1981).
- [12] R. Mailfert, B.W. Batterman and J.J. Hanak, *Phys. Lett.*, **24A** (6), 315 (1967).
- [13] R. Flükiger, W. Schauer and W. Goldacker, Superconductivity in d- and f-Band Metals (Karlsruhe, 1982), W. Buckel and W. Weber, eds., pp. 41-44.
- [14] A.J. Arko, D.H. Lowndes, F.A. Muller, L.W. Roeland, J. Wolfrat, A.T. van Kessel, H.W. Myron, F.M. Meuller and G.W. Webb, *Phys. Rev. Lett.*, **40** (24), 1590 (1978).
- [15] K. Hechler, G. Horn, G. Otto and E. Saur, *J. Low. Temp. Phys.*, **1** (1), 29 (1969).
- [16] T.P. Orlando, J.A. Alexander, S.J. Bending, J. Kwo, S.J. Poon, R.H. Hammond, M.R. Beasley, E.J. McNiff and S. Foner, *IEEE Trans. Mag.*, **MAG-17** (1), 368 (1981).
- [17] S. Foner and E.J. McNiff, Jr., *Phys. Lett.*, **58A** (5), 318 (1976).
- [18] R. Akihama, K. Yasukochi and T. Ogasawara, *IEEE Trans. Mag.*, **MAG-13** (1), 803 (1977).
- [19] C. Verwaerde, R. Taillard, C.E. Bruzek and Hoang-Gia-Ky, *Adv. Cryo. Eng.*, **42**, 1377 (1996).
- [20] Y.B. Kim, C.F. Hempstead and A.R. Strnad, *Phys. Rev.*, **139** (4A), A1163 (1965).

- [21] E.J. Kramer, *J. Appl. Phys.*, **44** (3), 1360 (1973).
- [22] R.M. Scanlan, W.A. Fietz and E.F. Koch, *J. Appl. Phys.*, **46** (5), 2244 (1975).
- [23] S. Ochiai and L. Osamura, *Acta Metall.*, **34** (12), 2425 (1986).
- [24] J.D. Livingston, , *Phys. Stat. Sol. A*, **44**, 295 (1977).
- [25] C.E. Bruzek, P. Sultan, E. Sirot., C. Kohler, P. Mocaër, F. Peltier and G. Grunblatt, *IEEE Trans. Appl. Supercond.*, **7** (2), 1041 (1997).
- [26] R. Akihama, K. Yasukochi and T. Ogasawara, *IEEE Trans. Mag.*, **MAG-13** (1), 803 (1977).
- [27] D.O. Welch, *Adv. Cryo. Eng.*, **30**, 671 (1984).
- [28] K. De Moranville, D. Yu and J. Wong, *Adv. Cryo. Eng.*, **40**, 931 (1994).
- [29] K. Tachikowa, T. Asano and T. Takeuchi, *Appl. Phys. Lett.*, **39** (9), 766 (1981).
- [30] K. Togano, T. Asano and K. Tachikawa, *J. Less. Comm. Met.*, **68**, 15 (1979).
- [31] I.W. Wu, D.R. Dietderich, J.T. Holthius, W.V. Hassenzahl and J.W. Morris, Jr., *IEEE Trans. Mag.*, **MAG-19** (3), 1437 (1983)
- [32] J.C. McKinnell, M.B. Siddal, P.M. O'Larey and D.B. Smathers, *Adv. Cryo. Eng.*, **40**, 945 (1994).
- [33] J. Ekin, *Adv. Cryo. Eng.*, **30**, 823 (1984).
- [34] T. Luhman, M. Suenaga and C.J. Klamut, *Adv. Cryo. Eng.*, **24**, 325 (1978).
- [35] R. Flükiger, R. Isernhagen, W. Goldacker and W. Specking, *Adv. Cryo. Eng.*, **30**, 851 (1984).
- [36] A.R. Kaufmann and J.J. Pickett, *Bull. Am. Phys. Soc.*, **15**, 838 (1970).
- [37] T. Miyazaki, N. Matsukura, T. Miyatake, M. Shimada, K. Takabatake, K. Itoh, T. Kiyoshi, A. Sato, K. Inoue and H. Wada, *Adv. Cryo. Eng.*, **44**, 943 (1998).
- [38] J.D. Elen, C.A.M. van Beijnen and C.A.M. van der Klein, *IEEE Trans. Mag.*, **MAG-13** (1), 470 (1977).
- [39] G. LeFranc and A. Müller, *J. Less-Comm. Met.*, **45**, 339 (1976).
- [40] M. Hansen, Constitution of Binary Alloys (McGraw-Hill, 1958), p. 634.
- [41] E. Barzi,, P.J. Limon, R. Yamada and A.V. Zlobin, *IEEE Trans. Appl. Supercond.*, **11** (1), 3573 (2001).
- [42] Y. Hashimoto, K. Yoshizaki and M. Tanaka, *Proc. of the 5th International Cryogenic Engineering Conference*, Kyoto, Japan 332 (1974).

- [43] W.K. McDonald, C.W. Curtis, R.M. Scanlan, D.C. Larbalestier, K. Marken and D.B. Smathers, *IEEE Trans. Mag.*, **MAG-19** (3), 1124 (1983).
- [44] Promotional brochure from Teledyne Wah Chang (now Wah Chang) (1989).
- [45] M. Takayasu, R.A. Childs, R.N. Randall, R.J. Jayakumar and J.V. Minervini, *IEEE Trans. Appl. Supercond.*, **9** (2), 644 (1999).
- [46] M. Suenaga and R.L. Sabatini, *Proc. of the 9th US-Japan Workshop on High Field Materials*, edited by K. Osamura et al., 111 (1995).
- [47] H. Oikawa and A. Hosoi, *Scr. Metall.*, **9**, 823 (1975).
- [48] D.S. Easton and D.M. Kroeger, *IEEE Trans. Mag.*, **MAG-15** (1), 178 (1979).
- [49] M.C. Jewell, P.J. Lee and D.C. Larbalestier, poster presented at the Applied Superconductivity Conference, Madison, WI (2000).
- [50] B.A. Glowacki, *IEEE Trans. Appl. Supercond.*, **7** (2), 1520 (1997).
- [51] Pearson's Handbook of Crystallographic Data for Intermetallic Phases, P. Villars and L.D. Calvert, 2nd edition, ASM International (1991).
- [52] Atlas of Crystal Structure Types for Intermetallic Phases, J.L.C. Daams, P. Villars and J.H. N van Nucht, ASM International (1991).
- [53] R. Taillard and C. Verwaerde, *Proc. Euromat95, Venice*, 471 (1995).
- [54] D.R. Dietderich, J. Glazer, C. Lea, W.V. Hasenzahl and J.W. Morris, Jr., *IEEE Trans. Mag.*, **MAG-21** (2), 297 (1985).
- [55] Handbook of Ternary Alloy Phase Diagrams, P. Villars, A. Prince and H. Okamoto, eds., ASM International, 9757 (1995).
- [56] C.E. Bruzek, P. Sultan, P. Mocaer, P. Mougnot, F. Peltier and G. Grunblutt, *Adv. Cryo. Eng.*, **42**, 1369 (1996).
- [57] E. Barzi, E. Gregory and T. Pyon, *IEEE Trans. Appl. Supercond.*, **11** (1), 3573 (2001).
- [58] N. Higuchi, K. Tsuchiya, C.J. Klamut and M. Suenaga, *Adv. Cryo. Eng.*, **30**, 739 (1984).
- [59] See for example, M. Wilson, Superconducting Magnets (Clarendon Press, Oxford, 1997), pp. 159-199.
- [60] Y. Zhang, J.C. McKinnell, R.W. Hentges and S. Hong, *IEEE Trans. Appl. Supercond.*, **9** (2), 1444 (1999)
- [61] R. Taillard and A. Ustinov, To be published in *Adv. Cryo. Eng.*, **45** (2000).
- [62] M. Onishi and H. Fujibuchi, *Trans. Jpn. Inst. Met.*, **16**, 539 (1986).

- [63] J.D. Verhoeven, A. Efron, E.D. Gibson and C.C. Cheng, *J. Appl. Phys.*, **59** (6), 2105 (1986).
- [64] J.A. Parrell, Oxford Instruments – Superconducting Technology, talk presented at the Low Temperature Superconducting Workshop, Napa CA, November 2001.
- [65] C.P. Bean, *Rev. Mod. Phys.*, **36**, 31 (1964).
- [66] M.C. Jewell, unpublished data.
- [67] C.M. Fischer, Master's Thesis, University of Wisconsin – Madison (2002).
- [68] A.M. Clogston, *Phys. Rev. Lett.*, **9** (6), 266 (1962).
- [69] R.R. Hake, *Phys. Rev.*, **158** (2), 356 (1967).
- [70] A.R. Sweedler, D.E. Cox and S. Moehlecke, *J. Nucl. Mat.*, **72**, 50 (1978).
- [71] A.K. Ghosh and M. Strongin, Superconductivity in d- and f- Band Metals, H. Suhl, M.B. Maple, eds., (Academic Press, New York, 1980) pp.305-315.
- [72] A. Godeke, personal communication, University of Twente, The Netherlands (2002).
- [73] T. Pyon and E. Gregory, *IEEE Trans. Appl. Supercond.*, **11** (1), 3688 (2001).
- [74] P.J. Lee, A.A. Squitieri and D.C. Larbalestier, *IEEE Trans. Appl. Supercond.*, **10** (1), 979 (2000).
- [75] M. Field, R. Hentges, J. Parrell, Y. Zhang and S. Hong, *IEEE Trans. Appl. Supercond.*, **11** (1), 3692 (2001).
- [76] P.D. Jablonski, personal communication (May 2002).
- [77] A. Gangulee, G.C. Das and M.B. Bever, *Met. Trans.*, **4**, 2063 (1973).

APPENDIX A – IMAGE ANALYSIS

A.1 Measuring Feature Sizes

Image analysis was performed on backscatter scanning electron microscope (SEM-BSE) images using Adobe Photoshop 6.0 software with the Image Processing Tool Kit 3.0 (IPTK) plugin by Reindeer Games. SEM-BSE images are used because the good atomic number contrast facilitates differentiation between the various components in the filament package. The SEM images were saved digitally as TIF images (Tagged Image File) in ‘indexed color’ mode by the SEM software, even though the SEM generates grayscale images. Therefore, in order to analyze an image, it had to be first converted to an 8-bit grayscale TIF.

The grayscale histogram gives the number of pixels at each of the 256 gray levels and is used to isolate the feature of interest (e.g the barrier) in the image to be analyzed. The ‘threshold’ feature allows one to highlight a range of gray levels within the grayscale histogram. Upon choosing a threshold level, the grayscale image changes into a purely black and white image, with the selected grayscale range now black and the rest of the grayscales white (or vice versa depending on the software) (Figure A.1).

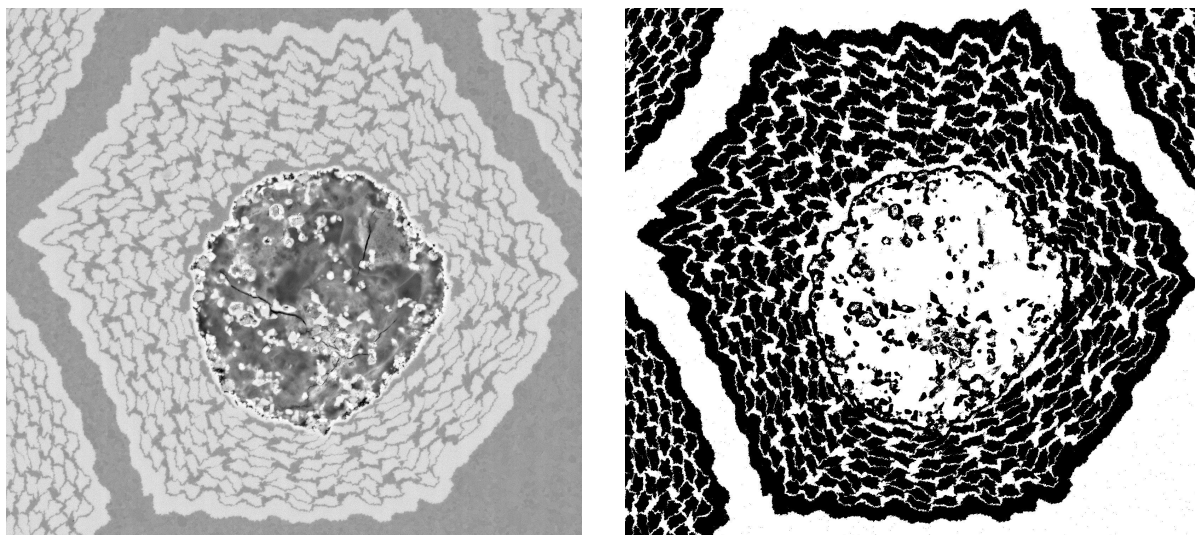


Figure A.1. (a) Grayscale SEM-BSE image of CRe1912 at 0.7 mm diameter, and (b) the same image in which the grayscales representing the filaments and barrier have been selected using the threshold feature. One can see that the image in (b) must still be manipulated so that only one bundle component is shown.

As a check of the quality of the threshold process, the black and white image was digitally overlaid on top the grayscale image to see if the feature of interest was adequately represented by the threshold image (Figure A.2). It was found that a few pixels within a given component (e.g. the barrier) were highlighted or not highlighted erroneously. This was usually near the edge of a feature, such as the Cu–Nb interface where significant intercurling can make accurate differentiation between the Cu and Nb difficult. By toggling the black and white threshold image on and off of the grayscale image, one could readily see these areas. The best threshold level was deemed to be one where there appeared to be an equal number of incorrectly highlighted and incorrectly non-highlighted pixels. While this may at first seem too subjective for quantitative analysis, it gave highly reproducible results, even with different users analyzing the same image. Nevertheless, it is a considered a potential source of error.

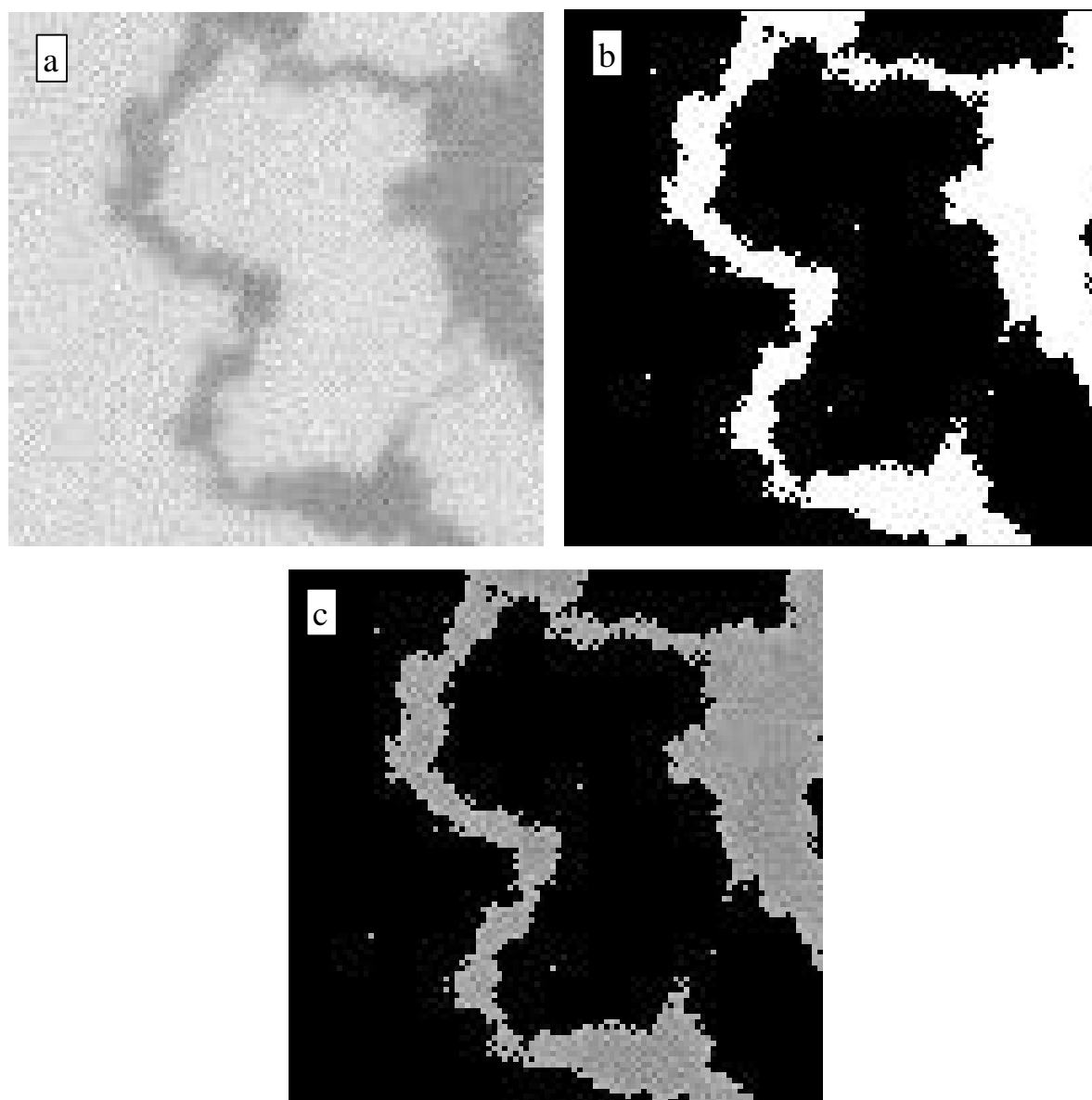


Figure A.2. Highly magnified portions of the (a) grayscale and (b) threshold digital images that more clearly show the effect of the threshold feature. In the images, the barrier is on the left, a filament is in the middle and the rest is the interfilamentary Cu. By combining the grayscale and threshold images (c), one can determine the accuracy of the threshold settings. In (b) and (c), one can also see stray erroneous pixels within the barrier and filament that have to be cleaned up manually.

After accurate threshold levels were achieved, the images still needed to be adjusted manually. As can be seen in Figure A.2(b), there were usually stray, erroneously highlighted pixels that were due to inevitable grayscale variations that occur in SEM images, even within a given material (e.g. the Sn cores). They can also be due to small particles on the sample surface. Any such erroneous pixels were changed manually. It was also necessary manually isolate the Nb–2at.%Ti filaments from the pure Nb barrier because it was not possible to distinguish between them by thresholding. This introduced another possible source of error, as it was sometimes difficult to determine whether a given pixel was part of the barrier or of a filament. Such pixels accounted for less than 1% of the number of pixels in the barrier or filaments. When only one component was featured and any stray erroneous pixels had been removed, the number of pixels within the component were counted by simply using the histogram feature on the black and white image. An image of each component of CRe1912 (0.7 mm diameter) after thresholding is shown in Figure A.3.

A.2 Atomic Ratio Calculations

A.2.1 Nb and Cu

The amount of Nb and Cu was calculated by simply multiplying the area of each (in pixels) by their respective atomic densities. As the desire was only to calculate the atomic ratios of the constituent elements, the true atomic count was not needed. The atomic volumes of the constituent elements were calculated from the crystallographic data given in [51,52] and are reproduced in Table A.1.

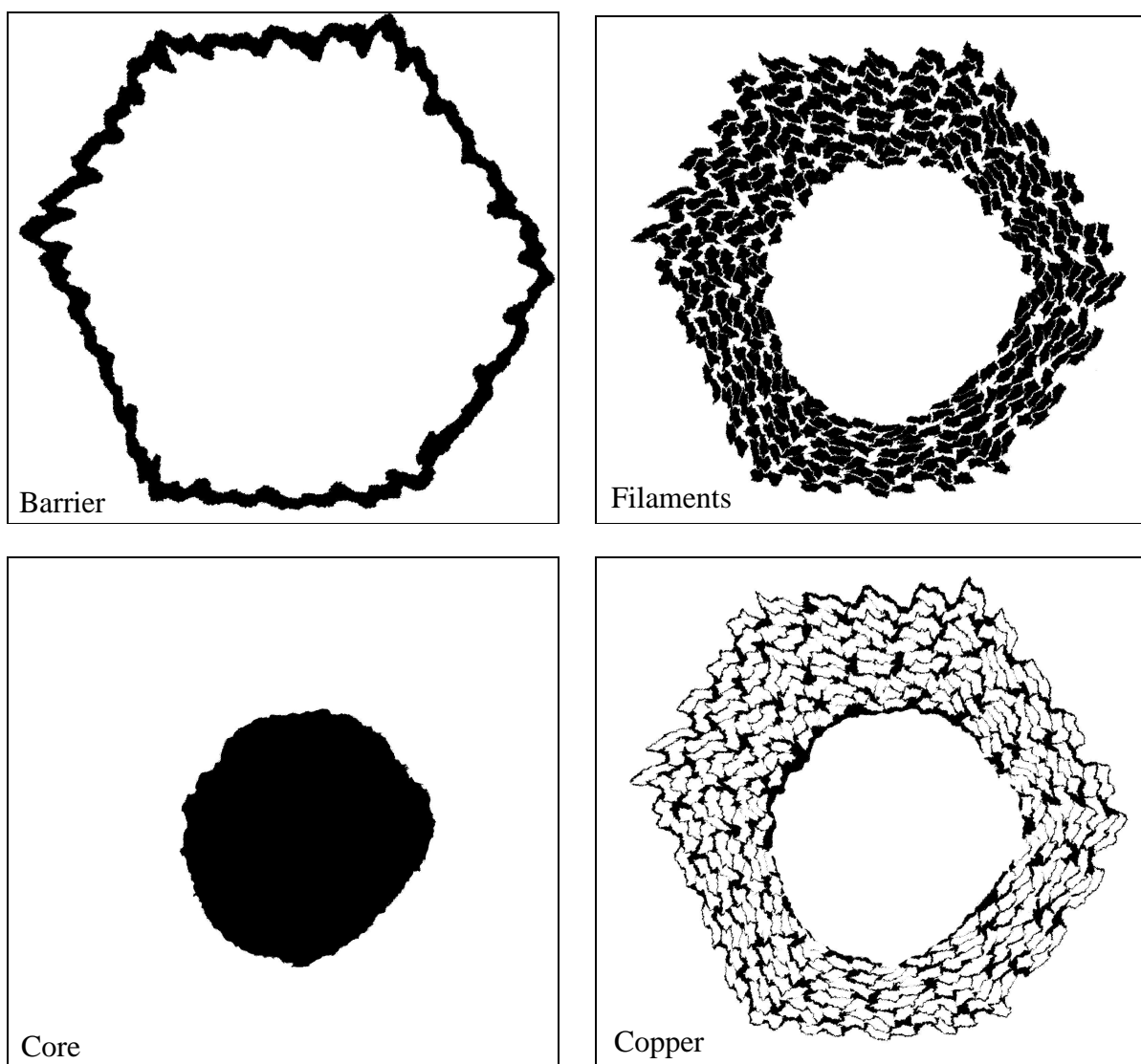


Figure A.3. Images of the barrier, filaments, core and interfilamentary Cu, which were used to determine the atomic ratios of the constituent chemical elements.

TABLE A.1
CRYSTALLOGRAPHIC DATA OF Cu, Nb AND Sn

	Cu	Nb	Sn
Atomic Density (atoms/nm ³)	84.8	55.3	37.0
Lattice Parameter(s) (Å)	a = 3.615	a = 3.3063	a = 5.8308 c = 3.1810
Atoms per Unit Cell	4	2	4
Structure Type	Cu	W	Sn
Space Group	Fm $\bar{3}$ m	Im $\bar{3}$ m	L4 ₁ /amd
Space Group Number	225	229	141
Pearson Symbol	cF4	cI2	tI4

The Ti solute in the Nb filaments was assumed to become a part of the A15 structure and reside on the Nb lattice. Therefore, as Ti is indistinguishable from Nb in this sense, no correction was made for the reduction in Nb due to the Ti addition to the filaments, and the filaments were treated as if they were pure Nb.

A.2.2 Alloyed Sn Core

As opposed to the Ti addition to the Nb filaments, the reduction in the fraction of Sn atoms in the core due to alloying must be taken into account as it directly results in the reduction of the amount of A15 that can be produced. The Sn-9at.%Mg and Sn-1.3at.%Cu cores are produced by a eutectoid reaction, therefore Mg₂Sn and Cu-Sn η -phase (\sim Cu₆Sn₅) precipitate out upon solidification. The recently developed Sn-5.9at.%Ti alloy (pure Sn plus \sim 4.5wt.% Ti₃Sn [76]) is a mixture of pure Sn and Ti₃Sn. The crystallographic data for Mg₂Sn, Cu₆Sn₅ and Ti₃Sn are listed in Table A.2.

TABLE A.2
CRYSTALLOGRAPHIC DATA OF Mg₂Sn, Cu₆Sn₅ and Ti₃Sn

	Mg ₂ Sn	Cu ₆ Sn ₅ *	Ti ₃ Sn
Atomic Density (atoms/nm ³)	38.9	57.4	55.3
Lattice Parameter(s) (Å)	a = 6.758	a = 4.192 c = 5.037	a = 5.921 c = 4.769
Atoms per Unit Cell	12	4.4	8
Structure Type	CaF ₂	AsNi	Ni ₃ Sn
Space Group	Fm $\bar{3}$ m	P6 ₃ /mmc	P6 ₃ /mmc
Space Group Number	225	194	194
Pearson Symbol	cF12	hP4	hP8

* 2 Cu interstitials are assumed per every 5 unit cells [77].

A.2.2.1 Sn-9at.%Mg

For the Sn–9at.%Mg eutectic reaction, the phase diagram lever rule dictates that pure Sn constitutes 86.5at.% (negligible solubility of Mg in Sn is assumed) and Mg₂Sn constitutes the remaining 13.5at.% (9at.% Mg and 4.5at.% Sn). The volume of the Sn and Mg components can be calculated as

$$\text{Sn: } \left(\frac{86.5 \text{ atoms pure Sn}}{37.0 \text{ Sn atoms/nm}^3} \right) + \left(\frac{4.5 \text{ atoms Sn in Mg}_2\text{Sn}}{38.9 \text{ Sn atoms/nm}^3} \right) = 2.45 \text{ nm}^3 \quad (\text{A.1})$$

$$\text{Mg: } \left(\frac{9 \text{ atoms Mg in Mg}_2\text{Sn}}{38.9 \text{ Mg atoms/nm}^3} \right) = 0.231 \text{ nm}^3 . \quad (\text{A.2})$$

Therefore, Sn accounts for 91.4 vol.% and Mg for 8.6 vol.% of the core. To calculate the atomic amount of Sn in the core, one must know the fraction of Sn in pure Sn and the fraction of Sn in the second phase. For Sn–9at.%Mg, 95.1% (= 86.5/(86.5+4.5)) of the Sn is

in pure Sn and 4.9% ($= 4.5/(86.5+4.5)$) is in Mg_2Sn . Therefore, the atomic count of Sn in an Sn–9at.%Mg core is

$$\# \text{ Sn atoms} = [\text{Volume of Sn Region}] \cdot [\text{Average Sn atomic density}]$$

$$\begin{aligned} \# \text{ Sn atoms} &= [0.914 \cdot (\text{Volume of core})] \cdot [0.951 \cdot (37.0 \text{ atoms/nm}^3) + 0.049 \cdot (38.9 \text{ atoms/nm}^3)] \\ &= (33.9 \text{ Sn atoms/nm}^3) \cdot (\text{Volume of core}) \end{aligned} \quad (\text{A.3})$$

Since the desire is to calculate only the atomic ratios, the volume of the core was simply calculated as the cross-sectional area multiplied by 1 unit in thickness (e.g. 1 pixel). From the factor in the last line of Equation A.3, a Sn–9at.%Mg core must be 9.1% larger ($37.0/33.9 = 1.091$) than a pure Sn core in order for there to be an equal number of Sn atoms.

A.2.2.2 Sn-1.3at.%Cu

Calculations of Sn–1.3at.%Cu cores are similar to those above. The eutectic reaction leads to 97.1at.% pure Sn and 2.9at.% Cu_6Sn_5 (Cu–Sn η -phase). Therefore, the volumes of Sn and Cu are

$$\text{Sn: } \left(\frac{97.1 \text{ atoms pure Sn}}{37.0 \text{ Sn atoms/nm}^3} \right) + \left(\frac{1.30 \text{ atoms Sn in } Cu_6Sn_5}{57.4 \text{ Sn atoms/nm}^3} \right) = 2.65 \text{ nm}^3 \quad (\text{A.4})$$

$$\text{Cu: } \left(\frac{1.56 \text{ atoms Cu in } Cu_6Sn_5}{57.4 \text{ Cu atoms/nm}^3} \right) = 0.027 \text{ nm}^3 . \quad (\text{A.5})$$

Thus, the volume fractions of Sn and Cu in the core are 99.0 vol.% and 1.0 vol.%, respectively. There is 1.3 at.%Sn in the Cu_6Sn_5 ($(5/11) \cdot 2.9$ at.%) and, therefore, 98.7% of the Sn is in pure Sn ($97.1/(97.1+1.32)$) and 1.3% Sn in Cu_6Sn_5 ($1.3/(97.1+1.3)$). The Sn atomic count in a Sn(Cu) core is calculated as

$$\begin{aligned} \# \text{ Sn atoms} &= [0.990(\text{Volume of core})] \cdot [0.987(37.0 \text{ atoms/nm}^3) + 0.013(57.4 \text{ atoms/nm}^3)] \\ &= (36.89 \text{ Sn atoms/nm}^3) \cdot (\text{Volume of Core}) \end{aligned} \quad (\text{A.6})$$

Therefore, a Sn-1.3at.%Cu core needs to be only 0.3% larger than a pure Sn core ($37.0/36.89$) to have the same number of Sn atoms.

A.2.2.3 Sn with Ti_3Sn

There is 4.5 wt.% Ti_3Sn in the Sn(Ti) alloy [76]. From the crystal structures, the calculated mass density of Sn is 7.29 g/cm^3 and that of Ti_3Sn is 6.02 g/cm^3 . Therefore,

$$\text{Sn: } \left(\frac{95.5 \text{ g pure Sn}}{7.29 \text{ g/cm}^3} \right) = 13.1 \text{ cm}^3 \quad (\text{A.7})$$

$$\text{Ti}_3\text{Sn: } \left(\frac{4.5 \text{ g Ti}_3\text{Sn}}{6.02 \text{ g/cm}^3} \right) = 0.75 \text{ cm}^3, \quad (\text{A.8})$$

and thus the pure Sn accounts for 94.6 vol.% and Ti_3Sn accounts for 5.42 vol.% of the Sn core. As Sn makes up $\frac{1}{4}$ of the Ti_3Sn compound, the Sn in Ti_3Sn takes up 1.4 vol.% of the

Sn core and, in sum, there is 95.9 vol.% Sn and 4.1 vol.% Ti in this Sn(Ti) alloy. Therefore, 98.5% and 1.5% of the Sn atoms are in pure Sn and Ti_3Sn , respectively, and the total Sn count is

$$\begin{aligned} \# \text{ Sn atoms} &= [0.959(\text{Volume of core})] \cdot [0.985(37.0 \text{ atoms/nm}^3) + 0.015(55.3 \text{ atoms/nm}^3)]. \\ &= (35.74 \text{ Sn atoms/nm}^3) \cdot (\text{Volume of core}). \end{aligned} \quad (\text{A.9})$$

A Sn + Ti_3Sn core must be 3.5% larger ($37.0/35.74$) than an pure Sn core to have the same number of Sn atoms.

APPENDIX B – Cu ELECTROPLATING

The Cu plating set-up is shown in Figure B.1(a). The Cu plating solution consisted of 1000 ml of H₂O, ~40 ml of H₂SO₄ and 185 g of CuSO₄. Distilled H₂O must be used in order to avoid significant dendrite formation. A ~7 cm diameter, 6 cm long OFHC (oxygen-free, high conductivity) Cu tube rested concentrically in a ~8 cm diameter, 5 cm tall Pyrex dish, and the dish was filled with plating solution. To facilitate Cu plating, the copper-oxide was removed from the sample ends by lightly etching in an acid solution consisting of 435 ml H₂SO₄, 72 ml HNO₃, 2 ml HCl and 491 ml H₂O ('copper brite'). The samples were then hung from metal clips such that their ends were submerged into the Cu plating solution within the Cu tube. The samples and Cu tube were connected to a power supply such that the samples were the cathode(s) and the Cu tube was the anode.

Dendrite formation on the wire is to be avoided because the higher electric field around a dendrite will draw Cu atoms toward it and away from the rest of the sample, resulting in preferential dendrite growth. One of the parameters controlling dendrite formation is the current. If the current is too high, the plated material will become porous, cracks can form and dendrites will grow. (However, if the current is too low, it will take a

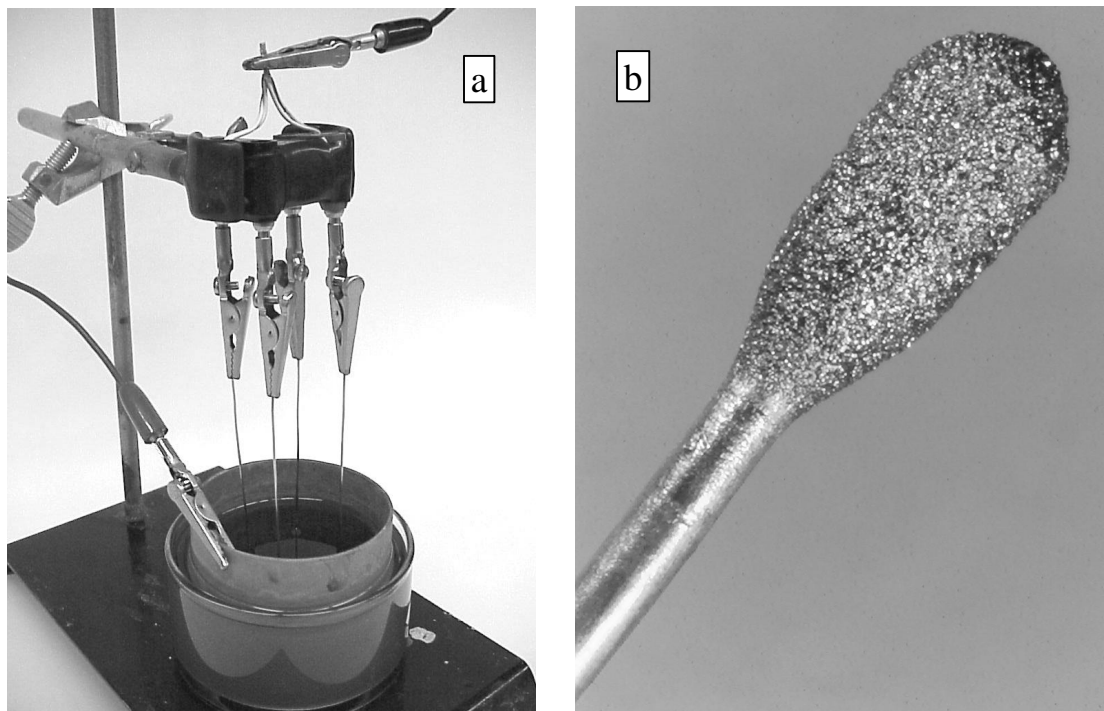


Figure B.1 (a) Photo of one Cu plating station, which plates up to 4 wires simultaneously. A series of plating stations can be connected to one another to increase the plating output from a single power supply. (b) Photo of the Cu plated end of CRe1912 at 0.7 mm diameter. The Cu plated region is ~2 mm in diameter and ~3.5 mm long.

long time to plate and there is a risk that the level of the plating solution will drop below the ends of the hanging samples due to evaporation.) Pores and cracks are also to be avoided because they give the liquid Sn a path out through the plated ends. It was found that there is also an increased risk for dendrite growth as the plating solution ages, perhaps due to significant evaporation of H_2O during the lifetime of the solution. When dendrites formed, it was usually sufficient to simply cut them off and continue plating, having made the proper adjustments to the current or plating solution.

For the samples studied in this thesis, each sample was submerged ~2 mm into the plating solution. Care was taken to ensure that the samples were submerged an equal distance into the plating solution so that each sample end had an equal conductance and thus

an equal plating rate. The ends were plated with a current of ~2 mA per sample, which is roughly between 0.25 and 0.4 mA/mm² of submerged sample area depending on wire diameter. A plating time of 24 hours per end (48 hours total) was sufficient such that no leaks were detected in any of the samples heat treated for this thesis (even when going directly from room temperature to 650°C). This plating rate generated a Cu plated end that was ~2 mm in diameter and ~3.5 mm long (Figure B.1(b)), with approximately 1 mm of that length grown beyond the end of the wire . A set of 3 plating stations (with 4 samples hanging in each) were connected in series so that 12 plated samples could be generated in 48 hours from one power supply.